

New Methods and Applications
in Nuclear Magnetic Resonance Microscopy
using small RF Coils

Dissertation zur Erlangung des
naturwissenschaftlichen Doktorgrades
der Bayerischen Julius-Maximilians-Universität Würzburg

vorgelegt von

Edmund Armin Porea

aus

Lugosch, Rumänien

Würzburg 2008

Eingereicht am:
bei der Fakultät für Physik und Astronomie

1. Gutachter: Prof. Dr. Peter Jakob
2. Gutachter:
der Dissertation.

1. Prüfer: Prof. Dr. Peter Jakob
2. Prüfer:
im Promotionskolloquium.

Tag des Promotionskolloquiums:

Doktorurkunde ausgehändigt am:

CONTENTS

1. <i>Introduction</i>	7
2. <i>Theory</i>	9
2.1 NMR basics	9
2.1.1 Spins and Magnetization	9
2.1.2 Relaxation	10
2.1.3 The spin echo	11
2.1.4 The gradient echo	11
2.1.5 The Bloch-Torrey equation and the diffusion amplitude	12
2.2 NMR imaging	13
2.2.1 Principle	13
2.2.2 The discrete \vec{k} -space and the resolution limit	14
2.2.3 2D and 3D imaging	16
2.3 Relaxation time and diffusion measurement methods	17
2.3.1 Longitudinal relaxation time T_1	17
2.3.2 Transverse relaxation time T_2	17
2.3.3 Apparent diffusion coefficient ADC	18
2.4 Small solenoids as RF coils	19
2.4.1 The principle of reciprocity	20
2.4.2 Sensitivity	20
2.4.3 The quality factor Q	21
3. <i>Quantitative imaging methods</i>	25
3.1 Measurement of T_1	25
3.2 Measurement of T_2	26
3.3 Measurement of T_2^*	26
3.4 Measurement of diffusion	28
4. <i>Multiple coil probehead</i>	29
4.0.1 Probehead construction	30
4.0.2 Parallel data acquisition	31
4.0.3 Results	32
5. <i>Susceptibility matching</i>	35
5.1 Alternative substances	35
5.1.1 BTCM	36
5.1.2 Fomblin	38
5.2 The dipole field around a capillary	38

5.3	Measurement of susceptibility	39
5.4	Results and Discussion	42
6.	<i>NMR microscopy of P. triangulum</i>	43
6.1	Imaging of the head	43
6.1.1	Methods	43
6.1.2	Results and Discussion	45
6.2	Imaging of the antenna	45
6.2.1	Methods	46
6.2.2	Results and Discussion	46
7.	<i>Chemical fixation of single cells</i>	49
7.1	The <i>X. laevis</i> oocyte as a model organism	50
7.2	Cell preparation	50
7.3	NMR experiments	51
7.4	Results and Discussion	52
7.4.1	Fixed samples	52
7.4.2	Fixed samples reimmersed in buffer	55
7.4.3	Gadolinium experiments	55
7.4.4	Spectroscopic experiments	56
7.5	Conclusion	56
8.	<i>Morphological studies of X. laevis embryos</i>	59
8.1	Embryo preparation	59
8.2	NMR imaging	60
8.2.1	Time lapse study	60
8.2.2	HMGN study	60
8.2.3	H1A study	60
8.3	Results and Discussion	60
8.3.1	Time lapse study	60
8.3.2	HMGN study	63
8.3.3	H1A study	63
8.4	Conclusion	64
9.	<i>Specific labeling using iron oxide</i>	65
9.1	Quantification of iron concentration	66
9.1.1	Relaxivity	67
9.1.2	Iron quantification	69
9.1.3	Verification using mass spectrometry	72
9.1.4	Discussion	73
9.2	Specific labeling of <i>X. laevis</i> embryos	73
9.2.1	Preliminary experiments	73
9.2.2	Methods and Materials	74
9.2.3	Results and Discussion	74
10.	<i>Conclusion and outlook</i>	79

11. Summary	81
12. Zusammenfassung	83
Appendix	85
A. Multichannel operation	87
A.1 Sequential acquisition	87
A.2 Simultaneous acquisition	87
A.3 Practical details	88
A.3.1 Sequential acquisition	88
A.3.2 Simultaneous acquisition	89

1. INTRODUCTION

After its discovery by Rabi in 1937 [1] and the first extensive experiments independently conducted by Bloch [2, 3] and Purcell [4] in 1946, the effect of nuclear magnetic resonance (NMR) has developed into a powerful tool for studying a multitude of different problems. Spectroscopic NMR allows structural and dynamical analysis of inorganic and organic molecules including proteins. The combination of NMR with spatially varying magnetic fields as introduced by Lauterbur [5] and Mansfield [6] in 1973 has opened up the field of magnetic resonance imaging (MRI), which is nowadays a standard diagnostic method in radiology, due to its advantages such as true non-invasiveness, rich contrast mechanisms and access to a variety of physical parameters. The NMR signal depends on many different microscopic parameters such as relaxation times, diffusion, local field strength and macroscopic parameters such as temperature and viscosity.

Driven by the idea of obtaining spatial resolutions significantly lower than $(1\text{ mm})^3$, instrumentation techniques were improved and specifically designed for this purpose. Most important advances were made by increasing the static magnetic field strength and optimizing the gradient coils necessary for spatial encoding as well as optimizing the actual NMR signal detector, the radiofrequency (RF) coil. The field of NMR microscopy, also termed NMR microimaging, evolved from within MRI. It was loosely defined by Callaghan [7] as NMR imaging at spatial resolutions below $(100\text{ }\mu\text{m})^3$. The method has been shown useful on a variety of applications, among which are *in vivo* imaging on small animals such as mice, imaging of tissue samples, plants and even single cells.

NMR imaging is an intrinsically insensitive technique, a fact that is even more significant in NMR microscopy. Although the feasible spatial resolution is inferior to other techniques such as optical microscopy, significant progress has been made over the last years. The first experiment with a spatial resolution below 1 mm was presented by Aguayo et al. [8]. Using a combination of a small NMR coil (5 mm solenoid) with a strong magnetic field (9.4 T), images of *Xenopus laevis* oocytes were obtained at resolutions up to $10 \times 13 \times 250\text{ }\mu\text{m}^3$. Good intracellular contrast between the nucleus and the cytoplasm was observed due to relaxation time differences. Higher spatial resolutions have been reported since: $(6.37\text{ }\mu\text{m})^3$ by Zhou [9], and in-plane resolution of $(4\text{ }\mu\text{m})^2$ by Cho et al. [10], even though the volume resolution of Zhou et al. was not exceeded until 2001 when Lee and coworkers reported 2D images with an in-plane resolution of $(1\text{ }\mu\text{m})^2$ and a slice thickness of $75\text{ }\mu\text{m}$ on a capillary phantom. In order to reach such a high resolution, strong gradients as large as 10 T/m in addition to a strong magnetic field (14.1 T) and a small RF coil (500 μm diameter) were used. An even higher volume resolution of $(40\text{ }\mu\text{m})^3$ was reported by Ciobanu et al. [11], using an even smaller microcoil with a diameter of 100 μm and a maximum gradient strength of 5.8 T/m. A phantom consisting of polymer beads in a capillary of 53 μm i.d. and 73 μm o.d. was imaged for validation purposes, followed by imaging of biological cells [12] (*Paramecium* and *Spirogyra* algae).

The resolution length scale of a few microns is obviously a threshold in NMR microimaging that is unlikely to be overcome within the next few years. Any morphological study of single cells using NMR microscopy is thus inferior to light microscopy. However, its multiparameter contrast mechanisms, the access to functional parameters such as temperature and diffusion provides additional information that complements optical or electron microscopy. Therefore, the aim of this work is increasing the efficiency of an NMR microscopic experiment and applying this new technique along with established methods to the study of a number of biological problems.

In Chapter 2, an overview of the theoretical aspects of NMR and MRI with a special view on microimaging will be given with respect to the regime where high spatial resolution is usually obtained: high static magnetic fields combined with small RF coils. In Chapter 3, the methods used for quantitative imaging are described. This comprises the measurement of relaxation times as well as diffusion which were necessary within various projects treated in the course of this work.

Chapter 4 describes a project that is aimed at improving the instrumentation used in NMR microscopy by constructing a probehead that contains four identical solenoid coils. An increase in the efficiency of microscopic experiments of small samples was successfully demonstrated by simultaneous acquisition of 3D NMR images from four single cellular samples.

The miniaturization of structures such as the RF coil leads to problems related to the close proximity of coil wire to the sample and the magnetic susceptibility difference between air, coil wire, capillary glass and sample. Methods have been described in the past that overcome the resulting field distortions. The general approach is known as susceptibility matching, and usually the NMR coil is either constructed of a material matched to the magnetic susceptibility close to that of air [13] or the coil is immersed in a fluid having a susceptibility comparable to that of the wire. Alternate fluids have been found and examined with regard to specific needs of certain applications. This project is described in Chapter 5.

In the following chapters, a number of applications on biological systems is presented. To begin with, it is customary practice in NMR microimaging to represent the morphology of a biological system in order to get accustomed to feasible spatial resolutions, contrast mechanisms and eventual sources of artifacts. The first project described in Chapter 6 deals with imaging an insect (beewolf) head. The objective was the representation of a large gland by visualizing its three-dimensional structure in the head capsule and determining its volume. In the work presented in Chapter 7, frog oocytes were used as a model to examine the process of chemical fixation and its impact on NMR parameters. Morphological studies of frog embryos that had modified levels of certain proteins relevant for their development were conducted. The methods and results are given in Chapter 8. Looking beyond morphology, the rather new field of specific targeting in NMR was examined on embryos of the same species. While specific targeting, e.g. by immunohistochemistry, is a standard method in biology, the adaptation to MRI and NMR microscopy using adequate contrast agents is an area of intensive study. Chapter 9 contains an experimental study of iron oxide contrast agents using transverse relaxation theory in inhomogeneous fields and its application on specific labeling of frog embryos.

A general conclusion is given in Chapter 10, and an outlook into potential continuation of the work is given.

2. THEORY

In this chapter, an overview of the theoretical background necessary for the understanding of the effect of NMR, the principle behind NMR imaging (MRI) and most important, the special case of NMR microimaging (NMR microscopy) will be given. Although achieving the highest spatial resolution is ultimately limited by SNR, two requirements must be fulfilled: first, a small voxel must be encoded in a short enough time to avoid signal depletion due to spin diffusion and second, a high enough sensitivity is necessary to detect the low number of spins present in such a voxel.

The encoding limitation will be addressed in section 2.2 in the context of NMR imaging. The sensitivity limitation is closely related to the RF coil used in the experiment, which is the topic of section 2.3.

2.1 NMR basics

2.1.1 Spins and Magnetization

The effect of nuclear magnetic resonance (NMR) is bound to the presence of nuclear spins, which correspond to a nuclear magnetic moment. In the following, the proton will be taken as an example to illustrate the physical basics of NMR. While other nuclei such as ^{31}P , ^{23}Na , ^{13}C and ^{15}N are also of great interest, the proton is by far the most sensitive and most abundant nucleus. Therefore, it is the nucleus of choice in NMR microimaging where the SNR is limited.

The spin of a proton is characterized by a spin quantum number $I = 1/2$, leading to a magnetic dipole moment $\vec{\mu}$:

$$\vec{\mu} = \gamma \vec{I} \quad (2.1)$$

The parameter γ is called gyromagnetic ratio and is a constant specific to a certain nucleus. For protons, $\gamma/2\pi = 42.5759$ MHz/T. If a proton spin is brought into a static magnetic field \vec{B}_0 , from a quantum mechanical point of view the static field will remove the energy degeneracy into the Zeeman levels $E_{\pm} = \mp \frac{1}{2} \gamma \hbar B_0$. The energy difference between the levels is $\Delta E = \gamma \hbar B_0$, and thus quanta with frequency $\omega = \gamma B_0$ can induce transitions between populations. Classically, the two energy states can be represented by parallel and anti parallel orientation of the spin with respect to the static magnetic field direction. For an ensemble of spins, a population difference will arise according to the Boltzmann distribution:

$$\frac{N_{-\frac{1}{2}}}{N_{+\frac{1}{2}}} = e^{-\frac{\gamma \hbar B_0}{k_B T}} \quad (2.2)$$

where k_B is the Boltzmann constant and T is the temperature of the spin system. At room temperature, only the difference between populations, which is about 1 ppm of all spins in the ensemble, will contribute to a macroscopic magnetization:

$$\vec{M} = \frac{\gamma^2 \hbar^2 N \vec{B}_0}{4k_B T} \quad (2.3)$$

Any change in population that leads to a deviation from the thermal equilibrium will tip the macroscopic magnetization away from the static field \vec{B}_0 . The result is a torque that is proportional to the temporal change in angular momentum \vec{M}/γ :

$$\frac{d\vec{M}}{dt} = \gamma \vec{M} \times \vec{B}_0 \quad (2.4)$$

Solving this equation again leads to $\omega = \gamma B_0$, which corresponds with the classical derivation. The magnetization is rotating in the x - y -plane precessing with the Larmor frequency.

Now an oscillating magnetic field \vec{B}_1 is added as a disturbance to \vec{B}_0 . If \vec{B}_1 is linearly polarized, it can be represented by two circularly polarized counter-rotating components, one of which rotates with ω in the same sense as the magnetization vector. In a frame of reference rotating with the Larmor frequency ω (the rotating frame), this rotating magnetic field \vec{B}_1 will be constant, leading to a precession with $\omega_1 = \gamma B_1$ due to

$$\frac{d\vec{M}}{dt} = \gamma \vec{M} \times \vec{B}_1 \quad (2.5)$$

If \vec{B}_1 is present for a certain time Δt , the magnetization will be tipped over by an angle $\theta = \gamma B_1 \Delta t$. The solution to Eq. 2.5 leads to transverse components of the magnetization $M_{x,y} \propto \sin(\omega_1 t)$ and a longitudinal component $M_z \propto \cos(\omega_1 t)$. The magnetization vector is tipped completely into the transverse plane if $\gamma B_1 \Delta t = \pi/2$.

After Δt , when the field \vec{B}_1 is turned off, the magnetization will rotate in the transverse plane. If a coil is placed around the sample, the rotating magnetization of the sample will induce an oscillating voltage at frequency ω proportional to the transverse component of the magnetization. This signal decays exponentially and is known as free induction decay (FID). The process leading to a decay of the signal amplitude is called relaxation and will be covered in the next section.

2.1.2 Relaxation

After excitation, the magnetization reverts to its thermal equilibrium: the longitudinal magnetization component M_z builds up and transverse magnetization $M_{x,y}$ decays. Such mechanisms are called relaxation. Although theoretical descriptions have been derived for the relaxation, a phenomenological description based on relaxation times is commonly used.

Spin-lattice relaxation

This relaxation process describes the reversal of the magnetization along the z -axis into thermal equilibrium. Spins change their orientation with respect to the static field by

returning into the ground state, thus energy is given off to the surrounding, which is denoted as the lattice. Therefore, T_1 relaxation is also known as spin-lattice relaxation. Mathematically, the relaxation process is characterized by the differential equation

$$\frac{dM_z}{dt} = -\frac{M_z - M_0}{T_1} \quad (2.6)$$

where M_0 is the initial magnetization, and its solution

$$M_z(t) = M_z(0)e^{-t/T_1} + M_0(1 - e^{-t/T_1}) \quad (2.7)$$

Spin-spin relaxation

The loss of coherence between spins is called transverse or spin-spin relaxation with a characteristic time T_2 . It is caused by dipole-dipole interaction between the spins and chemical exchange.

$$\frac{dM_x}{dt} = -\frac{M_x}{T_2}, \quad \frac{dM_y}{dt} = -\frac{M_y}{T_2} \quad (2.8)$$

The respective solutions are

$$M_x(t) = M_x(0)e^{-t/T_2}, \quad M_y(t) = M_y(0)e^{-t/T_2}. \quad (2.9)$$

The observable decay of transverse magnetization is occurring with characteristic time T_2 in a perfectly homogeneous magnetic field. If any fluctuations are present, however, the decay will occur faster due to the spatial distribution of Larmor frequencies. This increased decay rate is expressed by the relaxation time T_2^* , which is defined as

$$\frac{1}{T_2^*} = \frac{1}{T_2} + \gamma\Delta B_0 \quad (2.10)$$

2.1.3 The spin echo

If a second \vec{B}_1 pulse with pulse angle π is given after a $\pi/2$ -pulse, the spin dephasing due to magnetic field inhomogeneities can be reverted. In contrast, spin dephasing due to stochastic processes can not be reverted. While an FID decays with e^{-t/T_2^*} , the spin echo amplitude shows an attenuation according to e^{-t/T_2} instead. A series of spin echo experiments with varying echo time can therefore be used to determine the relaxation time T_2 . However, it should be noted that the method is sensitive to diffusion effects leading to the measurement of an apparent relaxation time $T_{2,app}$. In NMR microscopy, this is an important issue because microscopic field gradients can lead to a significant underestimation of T_2 .

2.1.4 The gradient echo

An alternative way to revert the spin dephasing after an excitation is the formation of a gradient echo. A defined gradient G_1 is turned on along an arbitrary direction (the x-axis

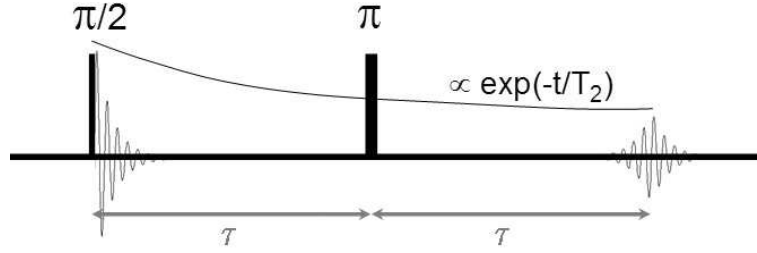


Fig. 2.1: The spin echo: right after the $\pi/2$ pulse, an FID signal is formed; T_2^* dephasing of the signal is reverted by the π pulse, forming an echo after 2τ .

is chosen exemplarily) for a time $t_{dephase}$, during which spins acquire a phase dependent on their position in space:

$$\phi(x) = \gamma B(x)t_{dephase} = \gamma Gx t_{dephase}. \quad (2.11)$$

Hereafter, a gradient G_2 is turned on with the opposite polarity. When the area $G_2 \cdot t$ equals the area $G_1 \cdot t_{dephase}$, the spin phase resulting from the first gradient is reverted under the assumption that the spin position did not change. This leads to the formation of a gradient echo. The time from the center of the excitation pulse to the center of the echo is called echo time T_E . It is worth noting that the amplitude is the same as the amplitude of the FID at the time T_E after excitation, as the echo amplitude decreases proportional to e^{-t/T_2^*} .

2.1.5 The Bloch-Torrey equation and the diffusion amplitude

Combining equations (2.4), (2.6) and (2.8), a set of differential equations is obtained that describes classically the evolution of the magnetization:

$$\frac{dM_x}{dt} = \gamma M_y B_0 - \frac{M_x}{T_2} \quad (2.12)$$

$$\frac{dM_y}{dt} = -\gamma M_x B_0 - \frac{M_y}{T_2} \quad (2.13)$$

$$\frac{dM_z}{dt} = \gamma - \frac{M_z - M_0}{T_1}. \quad (2.14)$$

This set of phenomenological equations characterizes the behaviour of a magnetization vector subject to longitudinal and transverse relaxation under the influence of an external static magnetic field $\vec{B}_0 = B_0 \vec{e}_z$. For the case where diffusion has to be considered, the Bloch equations have been modified by Torrey [14] by adding a diffusion term. The origin of the diffusion term is Fick's second law of diffusion for spin magnetization along any axis i under the assumption of isotropic diffusivity D :

$$\frac{dM_i}{dt} = D \nabla^2 M_i. \quad (2.15)$$

Combing the above Bloch equations with Fick's law, the Bloch-Torrey equations are obtained:

$$\frac{dM_x}{dt} = \gamma M_y B_0 - \frac{M_x}{T_2} + D \nabla^2 M_x \quad (2.16)$$

$$\frac{dM_y}{dt} = -\gamma M_x B_0 - \frac{M_y}{T_2} + D \nabla^2 M_y \quad (2.17)$$

$$\frac{dM_z}{dt} = \gamma - \frac{M_z - M_0}{T_1} + D \nabla^2 M_z \quad (2.18)$$

where M_0 denotes the magnitude of the magnetization. In the presence of a gradient G , which is assumed to be parallel to the static magnetic field B_0 , the total magnetic field becomes $B(\vec{r}, t) = B_0 + G(\vec{r}, t)$. RF excitation leads to transverse magnetization that can be expressed in complex notation as:

$$m(t) = M_x(t) + iM_y(t). \quad (2.19)$$

Equations (2.16), (2.17) and (2.18) lead to

$$\frac{\partial m}{\partial t} = \frac{\partial M_x}{\partial t} + i \frac{\partial M_y}{\partial t} = - \left(i\gamma(B_0 + \vec{G}\vec{r}) + \frac{1}{T_2} - D \nabla^2 \right) m. \quad (2.20)$$

This differential equation can be solved using the approach:

$$m(\vec{r}, t) = M_0 A(t) e^{i\gamma B_0 t - i\gamma \int_0^t \vec{G}(t') \vec{r} dt'} e^{-\frac{t}{T_2}} \quad (2.21)$$

where $A(t)$ contains the influence of diffusion upon the magnetization. Substitution of (2.21) in (2.20) leads to:

$$\frac{\partial A}{\partial t} = -\gamma^2 D \left(\int_0^t \vec{G}(t') dt' \right)^2 A(t). \quad (2.22)$$

Calculating the integral in the absence of flow, the diffusion amplitude becomes:

$$A(t) = e^{-\gamma^2 D \int_0^t \left(\int_0^{t'} \vec{G}(t'') dt'' \right)^2 dt'}. \quad (2.23)$$

For a constant gradient $G(t) = G_0$, determination of $A(t)$ yields:

$$A(t) = e^{-\frac{1}{3} \gamma^2 D G_0^2 t^3}. \quad (2.24)$$

Consequently, if a static gradient is present, the diffusion amplitude leads to signal degradation proportional to G^2 and t^3 .

2.2 NMR imaging

2.2.1 Principle

The principle behind NMR imaging is the utilization of magnetic field gradients in order to make the Larmor frequency depending on the spatial position of a spin. This makes the Larmor frequency dependent on the position:

$$\omega(\vec{r}) = \gamma B_0 + \gamma \vec{G} \cdot \vec{r} \quad (2.25)$$

where G is a vector of a linearly varying static magnetic field. Ignoring any relaxation process that leads to signal dephasing, the signal resulting from an infinitesimal volume element at position \vec{r} and spin density $\rho(\vec{r})$ is

$$dS(\vec{G}, t) = \rho(\vec{r}) e^{i(\gamma B_0 + \gamma \vec{G} \cdot \vec{r})t} dV. \quad (2.26)$$

After downmixing and integration, the signal amplitude becomes

$$S(t) = \int \int \int \rho(\vec{r}) e^{i\gamma \vec{G} \cdot \vec{r}t} d\vec{r}. \quad (2.27)$$

Obviously, the above represents a Fourier transformation where the time-dependent signal corresponds to the Fourier-transformed spin density.

A vector denoted \vec{k} has been introduced as the reciprocal space vector:

$$\vec{k} = \frac{\gamma \vec{G}t}{2\pi}. \quad (2.28)$$

In order to obtain the spatial spin density distribution, it is thus necessary to traverse \vec{k} -space either by a change in time t or gradient strength $|\vec{G}|$. Combining equations (2.27) and (2.28), $S(\vec{k})$ and $\rho(\vec{r})$ become mutually conjugate, linking the reciprocal \vec{k} -space to real space:

$$S(\vec{k}) = \int \int \int \rho(\vec{r}) e^{2\pi i \vec{k} \cdot \vec{r}} d\vec{r} \quad (2.29)$$

$$\rho(\vec{r}) = \int \int \int S(\vec{k}) e^{-2\pi i \vec{k} \cdot \vec{r}} d\vec{k}. \quad (2.30)$$

2.2.2 The discrete \vec{k} -space and the resolution limit

While an exact knowledge of \vec{k} -space is necessary for an identical representation of the real space spin density distribution $\rho(\vec{r})$, it is technically not feasible to obtain. Determination of the \vec{k} -space signal is actually a determination of the time-domain signal. Consequently, the signal can only be sampled in discrete steps. Also, the integration over \vec{k} -space is limited to the interval between $[-\vec{k}_{max}, \vec{k}_{max}]$ due to limited gradient strength \vec{G}_{max} . Although the above limits are general, there are many approaches as to how the \vec{k} -space shall be sampled. In most cases, the trajectory is cartesian. Assuming that the sampling is carried out with a step size of $\Delta\vec{k}$, general property of the discrete Fourier transformation leads to a spatial sampling width, also denoted as field-of-view (FOV), of $1/|\Delta\vec{k}|$. Although step sizes can be different in different orthonormal axes of reciprocal and real space, the same step size is assumed for all axes for simplicity. Subsequently, the obtained spatial resolution Δx is limited by $1/k$. In Fig. 2.2, a typical acquisition scheme is shown for imaging in two dimensions. In order to sample the desired \vec{k} -space, a

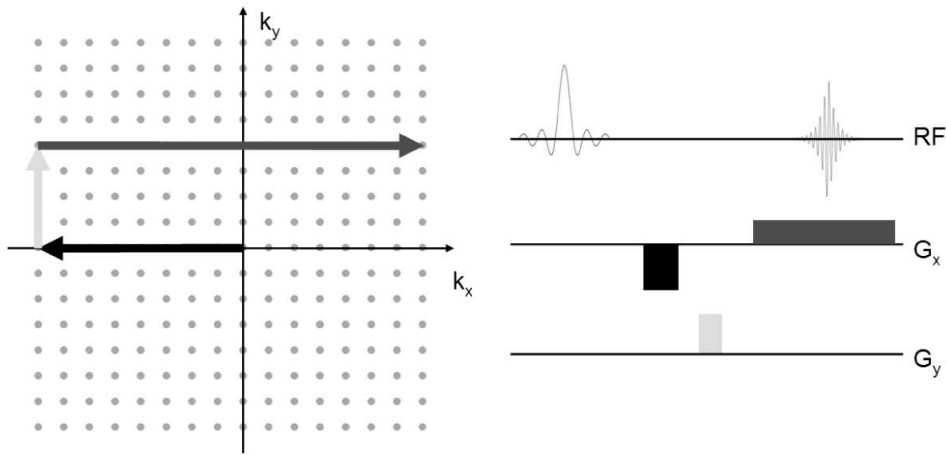


Fig. 2.2: k -space sampling scheme with frequency encoding (dephasing gradient: black, rephasing gradient: dark grey) and phase encoding (light grey) gradients

combination of frequency and phase encoding gradients is used (see next section). While the frequency encoding scheme allows acquisition of one \vec{k} -space line per scan, phase encoding allows one \vec{k} -space point to be acquired. Any modulating function $f(t)$ of the \vec{k} -space signal will obviously affect the real-space signal $\rho(r)$:

$$f(t) \times S(t) \leftrightarrow p(r) \otimes \rho(r). \quad (2.31)$$

The function $f(t)$ is called modulation-transfer function (MTF) and multiplication with the MTF in the time-domain corresponds to a convolution of the spatial spin distribution with the Fourier transform $p(r)$ of the MTF which is called the point-spread function (PSF). The PSF is a convolution of multiple PSF terms: the discretization of k -space, the natural linewidth and spin diffusion. The spatial resolution is defined as the full width at half maximum ($FWHM$) of the PSF. Intuitively, it is obvious that the achievable resolution cannot exceed the distance that a spin travels during the encoding time. If the spin motion is only dictated by diffusion, the spin travels a distance $\Delta x = \sqrt{2Dt}$. The diffusive signal attenuation has been calculated in section 2.1.4 from the Bloch-Torrey equations and is the MTF induced by diffusion, MTF_D , which varies depending on the spatial encoding scheme. A more detailed description of the involved MTFs has been published by Gravina and Cory [15].

Frequency encoding

In this acquisition scheme, the signal is acquired while a gradient \vec{G} is turned on, which means the \vec{k} -space is traversed in a direction parallel to \vec{G} . This method is known as frequency encoding because spins obtain a different frequency depending on their position; a common term for the frequency encoding gradient is read gradient. The PSF of the read gradient can be found by Fourier transformation of its MTF, and the $FWHM$ of the PSF yields the achievable resolution or vice-versa, the minimum gradient needed for achieving a given resolution [16]:

$$G \geq 2.8 \frac{2\pi D}{\gamma(\Delta x)^3}. \quad (2.32)$$

The bandwidth BW necessary to cover an object of elongation l at a frequency encoding gradient with strength G is given by:

$$BW = \frac{\gamma}{2\pi}Gl. \quad (2.33)$$

Increasing the spatial resolution requires stronger gradients and hence higher bandwidths. Because the SNR is inversely proportional to \sqrt{BW} , it is affected adversely at the same time.

Phase encoding

In contrast to frequency encoding, for phase encoding the acquisition is performed after a variable strength gradient has been turned on for a fixed time t_p . During application of this phase gradient, spins accumulate a phase dependent on their position with respect to the origin of the gradient frame of reference:

$$\Delta\phi = \gamma Gx t_p \quad (2.34)$$

A position offset is thus translated into a phase offset. Applying the Fourier transformation restores the position of the respective spins in space. Calculating the MTF and the $FHWM$ of the PSF hereafter, the minimum gradient strength for a given resolution is obtained [16]:

$$G \geq 1.8 \frac{2\pi D}{\gamma(\Delta x)^3} \quad (2.35)$$

Fig. 2.3 visualizes Eq. (2.35) for a given diffusivity. All experiments in this work were performed at a maximum gradient strength of 1 T/m, leading to a maximum spatial resolution of $\approx 5 \mu\text{m}$ for samples that have a diffusivity comparable to that of water. It shall be noted that the SNR in a phase encoding experiment is not affected by the actual encoding process as is the case for the read gradient because the gradient is switched off during acquisition.

2.2.3 2D and 3D imaging

In 2D imaging, only one slice of the whole sample is excited by using a frequency-selective RF (soft) pulse while a gradient is turned on. This gradient leads to spin dephasing, necessitating another gradient pulse with same area but opposite polarity in order to rephase the spins. Hereafter, the excited slice can be imaged by phase gradients or a combination of a phase gradient and a read gradient as shown in Fig. 2.2. It is also possible to apply two phase gradients simultaneously. The intrinsic spectroscopic information, such as chemical shift or frequency offset due to local magnetic field distortions is thus preserved, but the sequence is more time-consuming.

In 3D imaging, no slice selection is necessary, although in certain applications it might be desirable to excite just a certain volume within a larger sample for reduced FOV and to avoid folding artifacts. Generally, the whole sample is excited using an RF pulse that does not need to be frequency-selective (hard pulse). Hereafter, one k-space line is usually selected by applying two orthogonal phase gradients, and the line is read out in the third dimension using frequency encoding.

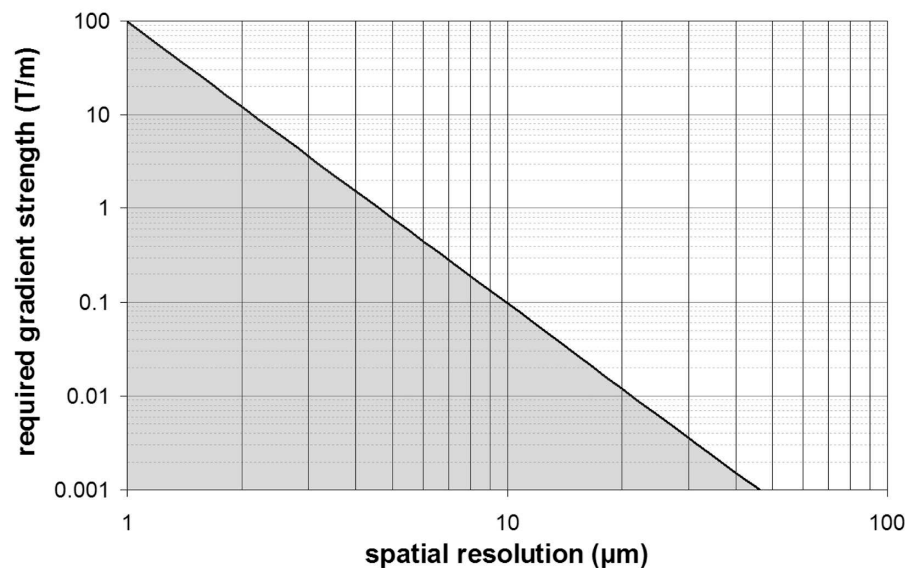


Fig. 2.3: Required gradient strength vs. achievable spatial resolution for phase encoding, $D=2.3 \cdot 10^{-9} \text{m}^2 \text{s}^{-1}$; shaded area not feasible

2.3 Relaxation time and diffusion measurement methods

2.3.1 Longitudinal relaxation time T_1

One of the standard methods for measuring T_1 is the saturation recovery experiment [17]. At the beginning of the sequence, the initial magnetization, which is assumed to be purely longitudinal ($\vec{M} = M_0 \vec{e}_z$), is completely saturated, e.g. by a burst of nonselective pulses as initially proposed. After a certain waiting time, the recurring magnetization is sampled by a $\pi/2$ pulse. Right after acquisition, the magnetization is again completely saturated and thus in the same defined initial state, independent of the repetition time T_R . The signal is acquired after various waiting times and allows calculation of T_1 after fitting to the function

$$M_z(t) = M_0(1 - e^{-t/T_1}) \quad (2.36)$$

which is the solution of Eq. 2.6 under the initial condition that the magnetization is saturated ($M_z(0) = 0$).

2.3.2 Transverse relaxation time T_2

It is customary to measure the transverse relaxation time with spin echoes because of the inherent T_2 dependence of the echo amplitude. Hahn proposed increasing the spacing between $\pi/2$ and π pulse to obtain echoes with decaying amplitude [18]. This decay is proportional to e^{-T_E/T_2} , and a line fit yields the T_2 relaxation time. However, employing this scheme severely affects the result obtained from fluids due to molecular diffusion. Any background magnetic field gradient G_0 present during the time t between excitation and acquisition will attenuate the obtained signal by a damping factor which has been derived according to the theoretical framework presented in Section 2.1.5:

$$A(t) = e^{-\frac{1}{3}\gamma^2 D G_0^2 t^3}. \quad (2.37)$$

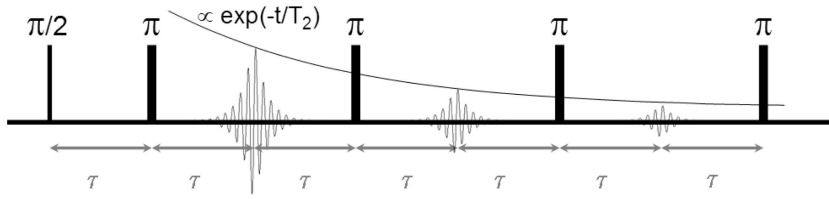


Fig. 2.4: Carr-Purcell-Meiboom-Gill echo train

Any additional gradient such as an imaging gradient increases the damping factor. If the attenuation varies with echo time, which is the case if the read dephase gradient is applied prior to the refocusing pulse, the diffusive attenuation will contribute to the apparent T_2 . Hsu and coworkers have minimized the influence of the imaging gradients [19] by turning any residual attenuation into a constant attenuation for variable echo time which thus does not contribute to the T_2 decay.

In order to minimize the effect of diffusion under a background gradient, Carr and Purcell optimized the spin echo sequence by applying consecutive π pulses 2τ after the first π pulse [20]. This causes an echo to appear after a time τ following each π pulse. The sequence was further optimized by Meiboom and Gill [21] by rotating the phase of the refocusing pulse by 90° with respect to the excitation pulse. While any imperfection in the refocusing pulse is accumulated over the Carr-Purcell sequence and leads to an additional decay besides T_2 , it only remains one constant offset after the Meiboom-Gill modification and is not accumulated. T_2 is obtained after acquiring a number of echoes and fitting to the function

$$M_{x,y}(t) = M_0 e^{-t/T_2}. \quad (2.38)$$

2.3.3 Apparent diffusion coefficient ADC

A method for the measurement of diffusion in a sample is based on Eq. (2.23) by introducing a new variable b :

$$b = -\gamma^2 \int_0^t \left(\int_0^{t'} \vec{G}(t'') dt'' \right)^2 dt'. \quad (2.39)$$

Integration of the value b requires consideration of the applied gradient scheme. If a sequence is used where only the diffusion gradient is varied, experimental results differ in the amount of diffusive attenuation solely:

$$A = e^{-bD}, \quad (2.40)$$

and fitting the data to this exponential function with varying b yields the diffusion coefficient D . The most common diffusion experiment is the pulsed-field gradient experiment as introduced by Stejskal and Tanner [22], where two consecutive gradient pulses with opposite polarity are applied, each for a time δ and with a temporal spacing of Δ . Stationary spins experience a location-dependant dephasing after the first gradient pulse that is fully reverted by the second pulse. The phase of diffusing spins does not fully revert after the second pulse due to their movement. Details on this sequence are given in Sec. 3.4.

It shall be noted that diffusion experiments in NMR are often conducted on samples that impede the truly random diffusion, e.g. as in a water sample if no convection is present. Therefore, in the presence of diffusion barriers such as protein molecules or cell membranes, the observed diffusion can differ from the molecular diffusion in a free medium. To account for this difference, the commonly used term is apparent diffusion coefficient (ADC). Additionally, in this deduction, diffusion is assumed to be isotropic. If the diffusion shows anisotropies due to anisotropic barriers, D has to be substituted by the tensor \overline{D} .

2.4 *Small solenoids as RF coils*

In the last section, it has been described how diffusion affects spatial encoding. Strong gradients are necessary to reduce the voxel size. However, even for static spins a limit is reached where the signal obtained from a single small voxel is below the noise threshold. Therefore, achieving high spatial resolution in NMR imaging is ultimately limited by the SNR. There are two prominent methods how to increase the SNR obtained from a single voxel: (a) cooling down the receiver coil to reduce the thermal noise level and (b) reducing the receiver coil size. Following approach (b), small solenoid NMR coils have been developed which have been termed 'microcoils'. A mathematical explanation will be given in the course of this section. Although no precise definition exists for a microcoil, it is generally used for coils with an observe volume of 1 μl and below [23].

The first reported use of NMR microcoils dates back to 1966, when Odeblad used a series of solenoid coils with diameters ranging from 200 to 1000 μm in order to study the physical chemistry of mucus from single secreting human cervix cells by continuous wave (CW) NMR [24]. In 1979, Shoolery published applications in ^1H and ^{13}C spectroscopy using a 1.7 mm diameter saddle coil [25]. Crouch et al. reported development of micro-NMR probes with 100 and 150 μl sample volumes and respective diameters of 2.5 and 3 mm at 11.7 T in 1992 [26]. In 1999, Martin et al. [27] reported a 30 μl probe with a diameter of 1.7 mm that was compared to a 3 mm probe. In 2002, a triple X inverse (TXI) probe was developed by Bruker Switzerland in cooperation with Hoffmann-La Roche AG that had an observe volume of 2.5 μl [28]. Linewidths below 1 Hz were obtained at 14.1 T.

Olson et al. [29] presented NMR spectra of 5 nl samples obtained with a coil ten orders of magnitude smaller than typical coils mentioned above. The sensitivity of arginine and sucrose spectra was enhanced by a factor of 130 compared to a conventional 5 mm tube sample. The linewidth was also improved by immersing the coil in a medium that matches the magnetic susceptibility of copper. This issue will be addressed in Chapter 5. Peck et al. [30] further addressed the theoretical background of microcoil construction. The resistance of the coil was evaluated with regard to different regimes of the conductor/skin depth-ratio, leading to predictable performance enhancements for microcoils as small as 50 μm in diameter. Webb and Grant [31] studied the influence of filling factor on the obtained linewidth for a 355 μm solenoid by varying the inner diameter from 50 μm to 250 μm , thus varying the filling factor from 2.0% to 51.0%. It was shown that the SNR could be improved with little loss in spectral resolution.

2.4.1 The principle of reciprocity

As shown by Hoult and Richards [32], the SNR of the NMR experiment is proportional to

$$SNR \propto \frac{B_1}{i} V_s N \gamma \frac{h^2}{4\pi^2} I(I+1) \frac{\omega_0^2}{3\sqrt{2}kTU_{noise}}. \quad (2.41)$$

Here, V_s is the sample volume, N the number of spins per volume, U_{noise} is the sample and coil noise and B_1/i is the magnetic field generated by the coil per unit current. Hoult and Richards have shown that the signal induced in the coil by the sample magnetization at any point in space is directly proportional to the B_1 field that would be generated in the same point by unit current passing through the coil. This important relationship is called the principle of reciprocity. It shows that the performance of an NMR coil while transmitting is directly proportional to the case when it is receiving. The expression B_1/i is therefore called sensitivity; the SNR obtained from an NMR coil is directly proportional to its sensitivity.

2.4.2 Sensitivity

Furthermore, Hoult and Richards studied the sensitivity of two most common used coil types, the solenoid and the saddle coil. While the saddle coil is advantageous since the magnetic field it produces is transverse to the magnet bore axis, the solenoid coil offers a sensitivity that is superior to the saddle coil by almost a factor of three. This is caused by the higher magnet field density inside the solenoid coil.

The sensitivity of a solenoid with n turns ($n \gg 1$) can be calculated from the Biot-Savart law. It is given by

$$\frac{B_1}{i} = \frac{\mu_0 n}{\sqrt{4r^2 + l^2}} \quad (2.42)$$

where r is the coil radius and l the coil length. Obviously, the coil sensitivity is inversely proportional to the coil diameter, and a reduction in coil size leads to higher sensitivity and subsequently higher SNR.

Miniaturization of the coil has another advantage: with the power available on common RF transmitters, the necessary pulse length becomes short, on the order of few μs , which in turn allows broadband excitation. This is most useful in protein NMR, when aliphatic and aromatic compounds need to be excited (0 – 140 ppm).

Mass and concentration sensitivities have also been defined with respect to spectroscopic applications on fluids [33]:

$$S_m = \frac{SNR}{m}, S_c = \frac{SNR}{c} \quad (2.43)$$

where m is the mass of diluted sample and c the concentration. To determine the dependence of mass and concentration sensitivities on increasing or reducing the coil size, rescaling a solenoid with a factor f in all three spatial dimensions is considered, as shown in Fig. 2.5. Regarding Eq. (2.41) with focus on factors dependent on the elongation:

$$SNR \propto \frac{B_1}{i} V_s N. \quad (2.44)$$

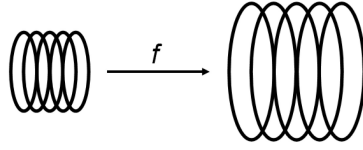


Fig. 2.5: Scaling of a solenoid

Introducing the scaling factor in all relevant parameters, the sensitivity becomes:

$$\frac{B_1}{i} = \frac{\mu_0 n}{\sqrt{4(f \cdot r)^2 + (f \cdot l)^2}} = \frac{\mu_0 n}{f \sqrt{4r^2 + l^2}}, \quad (2.45)$$

and the volume becomes:

$$V_s = f^3 V_s. \quad (2.46)$$

Mass sensitivity

For a given mass m , or a certain number of spins $N_{spins} = V_s N$, the dependence of mass sensitivity S_m on coil scaling is

$$\frac{SNR}{m} \propto \frac{SNR}{N_{spins}} \propto \frac{B_1}{i} \frac{1}{f} \propto \frac{1}{f}. \quad (2.47)$$

Mass sensitivity is inversely proportional to the coil dimensions. If a certain sample mass is given and the sample concentration can be chosen arbitrarily, only constrained by solubility, e.g. in protein applications, the mass sensitivity is higher for smaller coils.

Concentration sensitivity

If sample mass is variable and the concentration c and thus the spin density N is fixed,

$$\frac{SNR}{c} \propto \frac{SNR}{N} \propto \frac{B_1}{i} \frac{1}{f} f^3 V_s \propto f^2. \quad (2.48)$$

For a given sample concentration, the concentration sensitivity increases with the square of the coil size.

In conclusion, reducing the coil size is advantageous for limited mass samples. If unlimited sample amount is present, a large coil provides a superior SNR . Improving the spatial resolution is a 'limited mass'-situation as the number of spins in a small voxel is limited. In this case, coil size reduction is necessary for improved sensitivity.

2.4.3 The quality factor Q

The quality factor Q of a series RCL circuit, where L is the inductance of the probe coil, R is the Ohmic resistance of the coil and C is a capacitance, is defined as

$$Q = \frac{\omega L}{R}. \quad (2.49)$$

Frequency f(MHz)	skin depth $\lambda(\mu\text{m})$
60	8.5
100	6.6
300	3.8
500	3.0
600	2.7
750	2.4

Tab. 2.1: Skin depths in copper at various frequencies

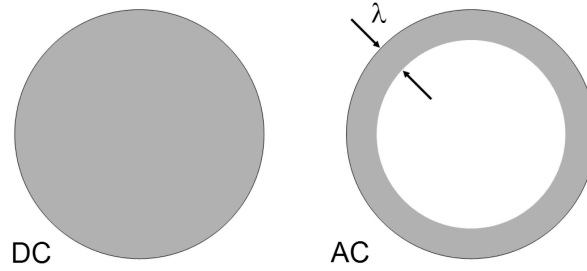


Fig. 2.6: Cross section of a circular conductor at DC and AC; current flows in the gray areas

It reflects how much magnetic energy is stored in the resonant circuit at the expense of current lost due to Ohmic resistance. For DC, R is a constant. For AC, however, the resistance is increased due to an effect known as skin effect which is caused by eddy currents inside the conductor. At the edge of the conductor, no compensation of the current is present, leading to an area where current is flowing. The skin depth is given by

$$\lambda = \frac{1}{\sqrt{\mu_0 \pi f \sigma}} = \sqrt{\frac{2}{\mu_0 \omega \sigma}} \quad (2.50)$$

where f is the frequency and σ is the conductivity of the conductor. The skin depth λ is the distance inside the conductor where the current has dropped to $1/e$ of its value at the surface. Table 2.1 summarizes the skin depths in copper at various frequencies.

The overall coil resistance R therefore becomes dependent on the available cross-section. The frequency-dependent quality factor $Q(f)$ of a solenoid coil can be calculated using expressions for the inductance L and the resistance $R(f)$ following the definitions in Fig. 2.7:

$$L = \frac{\mu_0 \pi (r + d)^2 N}{l} \quad (2.51)$$

$$R = \frac{s}{\sigma A(f)}. \quad (2.52)$$

The total wire length s is given by $s = 2\pi N(r + d)$ and the frequency-dependent cross section $A = \pi \lambda (2r - \lambda)$. For $\lambda \ll r$, A becomes $\approx 2\pi r \lambda$. Combining Eq. (2.49), (2.51) and (2.52), Q becomes:

$$Q = \omega \frac{\mu_0 \pi (r + d)^2 N}{l} \frac{\sigma 2\pi r \lambda}{2\pi N (r + d)} = \frac{2\pi r (r + d)}{l \lambda}. \quad (2.53)$$

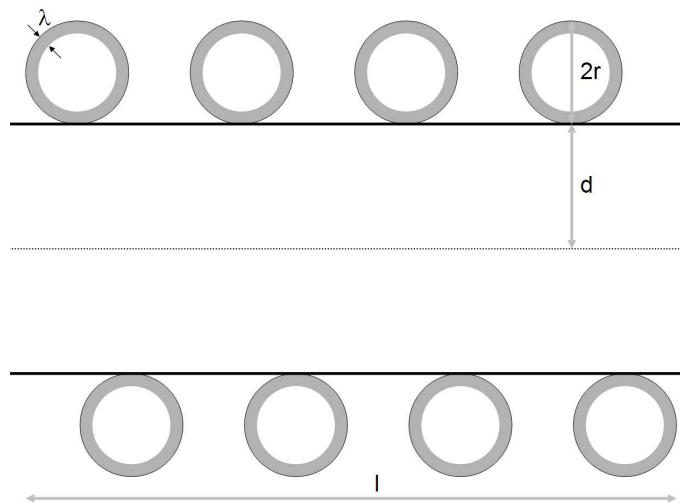


Fig. 2.7: Cross-sectional view of a solenoid coil with four windings wound on a glass capillary

The quality factor of a resonant circuit can be determined by measuring the reflected power over a frequency sweep around the resonant frequency [34]. The width $\Delta\omega$ at the -7 dB drop (or 1/5) of the incident power yields the quality factor:

$$Q = \frac{\omega}{\Delta\omega}. \quad (2.54)$$

3. QUANTITATIVE IMAGING METHODS

In this chapter, the imaging sequences carried out for the three-dimensional determination of the relaxation times T_1 , T_2 , T_2^* and the apparent diffusion coefficient (ADC) are described. All experiments were performed on a Bruker 17.6 T (750 MHz), 89-mm widebore magnet with a gradient insert (Micro2.5, maximum gradient $G_{max} = 1$ T/m, clear bore 40 mm) and a Bruker AVANCE 750 console (Bruker Analytik, Rheinstetten, Germany). If not indicated otherwise, 256 complex points were acquired in the read direction, which was usually chosen along the capillary axis, along with 32 steps in each phase direction and two averages. With a FOV of $3.84 \times 1.92 \times 1.92$ mm³, the resulting spatial resolution was $30 \times 60 \times 60$ μm^3 .

Parameter fitting was always carried out using a three-parameter nonlinear least squares fit written in IDL (Research Systems Inc., Boulder, CO, USA).

3.1 Measurement of T_1

In order to measure T_1 , a saturation recovery preparation was combined with a 3D spin echo readout. The saturation module consisted of nine excitations with a $\pi/2$ and a π -pulse of varying phases and variable crusher gradients hereafter. This sequence was presented by Brandl as a very effective method for saturating [35]. The complete values are given in Table 3.1. When lipid was present in the sample and caused unwanted signal, selective excitation using a binomial 1331-pulse [36] centered at the water frequency was used instead of the $\pi/2$ excitation pulse in the spin echo readout sequence. Spatially resolved T_1 -maps were obtained after fitting data for each pixel. Five different variable delay times vd were used (160, 320, 640, 1000 and 2000 ms). Data acquisition time was approximately 3 hours.

n	$\pi/2$ pulse phase	π pulse phase	G_R	G_{P1}	G_{P2}
1	0	180	10	0	0
2	60	240	20	0	0
3	120	300	40	0	0
4	180	0	0	12	0
5	240	60	0	24	0
6	300	120	0	48	0
7	0	180	0	0	9
8	60	240	0	0	18
9	120	300	0	0	36

Tab. 3.1: Pulse phases (in degrees) and gradient strengths (in percent of max. gradient strength) utilized for saturation in the quantitative imaging experiments

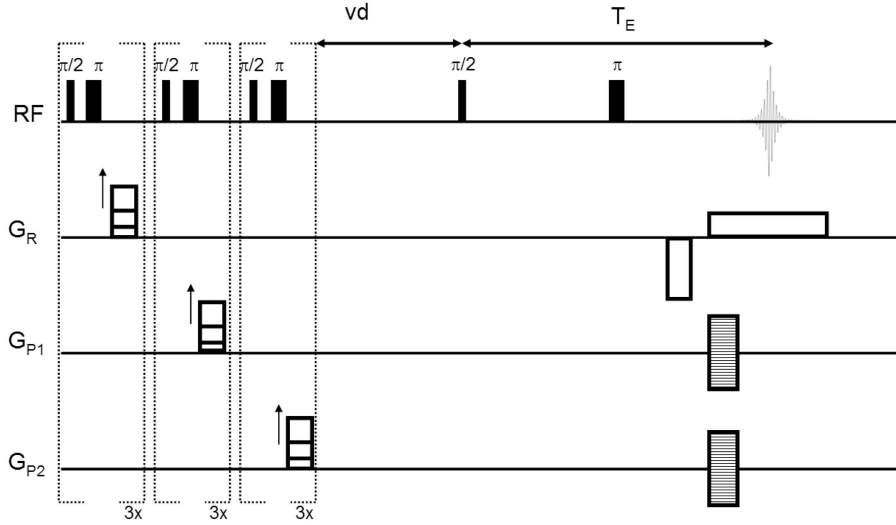


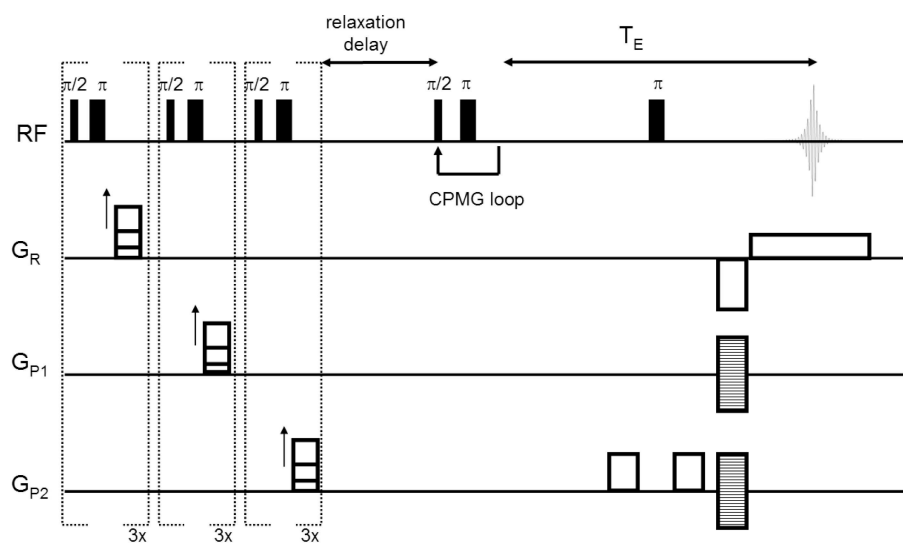
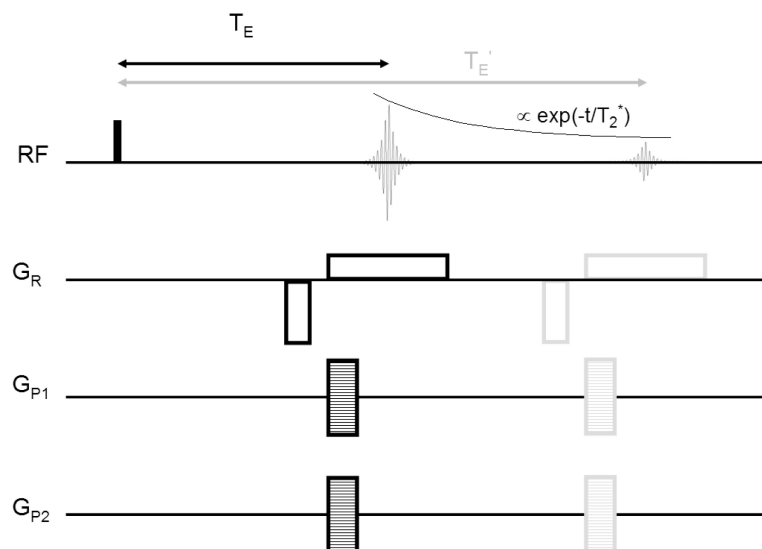
Fig. 3.1: 3D T_1 experiment with spin echo readout

3.2 Measurement of T_2

The spin-spin relaxation time T_2 was measured with a global CPMG preparation module after global saturation as used on the T_1 measurement. As shown in section 2.3.2, for increased spatial resolutions and resulting higher gradient strengths, a CPMG sequence rather than a variable echo time spin echo sequence has to be used to minimize the effects of diffusion on the T_2 measurement. Otherwise, the measured T_2 is becoming an apparent $T_{2,app}$ [37]. A spoiler gradient pair arranged symmetrically around the refocusing pulse was used in the first phase encoding direction.

3.3 Measurement of T_2^*

The relaxation time T_2^* is composed of spin-spin relaxation T_2 and additional relaxation due to magnetic field inhomogeneities (see Section 2.1.2). In macroscopic imaging, it is determined using a method known as multi-echo gradient echo. In this sequence, additional gradient echoes are formed after an initial gradient echo by constant dephasing and rephasing of spins, in analogy to the CPMG sequence, although the refocusing is performed using RF pulses and yet yields T_2^* . A k -space line is acquired for every echo. While the method is rather time-efficient, its drawback for microscopic applications becomes obvious after regarding the necessary gradient power necessary; it leads to strong diffusion attenuation and thus obscures the real T_2^* . In this work, T_2^* was measured by acquiring individual gradient echo data sets with different echo times. The diffusive attenuation from the imaging sequence is always constant and does not contribute to an apparent $T_{2,app}^*$. The sequence used is shown in Fig. 3.3 for two different echo times.

Fig. 3.2: 3D T_2 experiment with spin echo readoutFig. 3.3: Two 3D T_2^* experiments at different echo times

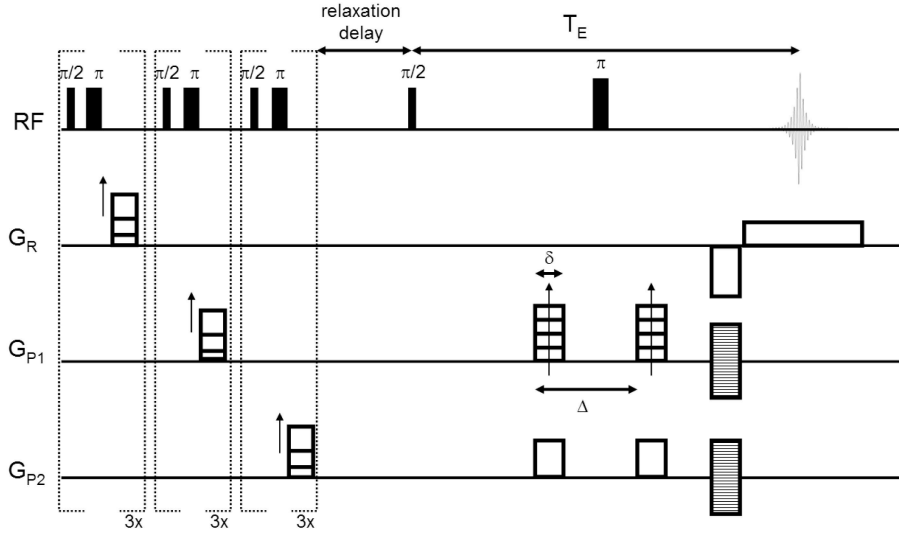


Fig. 3.4: 3D pulsed-gradient diffusion experiment with spin echo readout

3.4 Measurement of diffusion

Apparent diffusion coefficients (ADCs) were calculated from data obtained using a standard pulsed-field gradient experiment as introduced by Stejskal and Tanner [22]. In this type of experiment, the attenuative effect from the spin motion under the influence of gradients is exploited by applying a pair of defined gradients with separation Δ and length δ . Solving the diffusion amplitude equation for such a gradient sequence yields the attenuation of the echo amplitude:

$$A(\delta, \Delta) \propto e^{-\gamma^2 G^2 D \delta^2 (\Delta - \delta/3)} = e^{-bD} \quad (3.1)$$

with

$$b = -\gamma^2 G^2 \delta^2 (\Delta - \delta/3). \quad (3.2)$$

Five different b-values from 40 to 1470 s/mm² were used. If not indicated otherwise, the values of δ and Δ were 1.6 ms and 6 ms, respectively.

4. MULTIPLE COIL PROBEHEAD

In a regular MRI experiment, a single sample is imaged at a time, occupying a significant fraction of the maximum space available for imaging. For small samples however, it is natural to consider the possibility of imaging many samples simultaneously to increase the experiment efficiency. This is especially desirable on systems with limited access time and high operational costs, such as high-field systems. A number of such "parallel" data acquisition approaches have recently been presented, both in NMR spectroscopy and imaging.

Multiple coil NMR spectroscopy and the resulting increase in sample throughput has potential applications in the drug discovery in the pharmaceutical industry as well as in protein structure elucidation, where time consuming experiments can be performed on more than one protein simultaneously. There are mainly two different approaches in NMR spectroscopy for simultaneous acquisitions of spectra from multiple samples. In the first approach, all probe coils are connected in parallel, forming a single resonant circuit [38, 39, 40]. Signals are selected from individual coils by using spatially selective pulses. In the second approach, each probe coil is connected to a resonant circuit, all of which are isolated from each other [41]. Most of these probeheads contain two to four single resonance coils. This configuration has also been presented with up to eight individual coils [42] and on multiple frequencies [43].

MRI experiments on multiple samples have mostly focused on imaging of mice and different experimental setups have been evaluated [44]. Possible setups incorporate single or separate receiver coils, receiver channels and gradient sets, respectively. It is clear that positioning multiple samples in a single receiver coil and a single gradient set requires the least complexity at the expense of signal-to-noise ratio and spatial resolution. On the contrary, using separate RF coils and gradient sets for each sample allows acquisition with highest sensitivity and highest spatial resolution with high hardware complexity as significant drawback [45]. Most approaches have focused on using separate RF coils but a single gradient set for high sensitivity along with moderate complexity [44, 46]. Among those, it has to be differentiated between those employing a single receiver multiplexed to all RF coils or those using multiple receivers.

The main technical challenge in developing these types of probeheads is achieving a decoupling of at least 20 dB between the coils such that the cross talk is minimized. This is typically accomplished by shielding the individual coils and networks using thin conductive sheets. On the other hand, placing a shield near an RF coil distorts the B_1 field depending on the separation, ultimately limiting the number of coils that can be placed in a certain volume. Evaluation of the impact of a shield on the B_1 field of a solenoid depending on the separation was carried out [47]. If the separation is above one coil radius, distortions in the B_1 field are below 10%.

In this chapter, the design, construction, and application of a highfrequency, four-coil

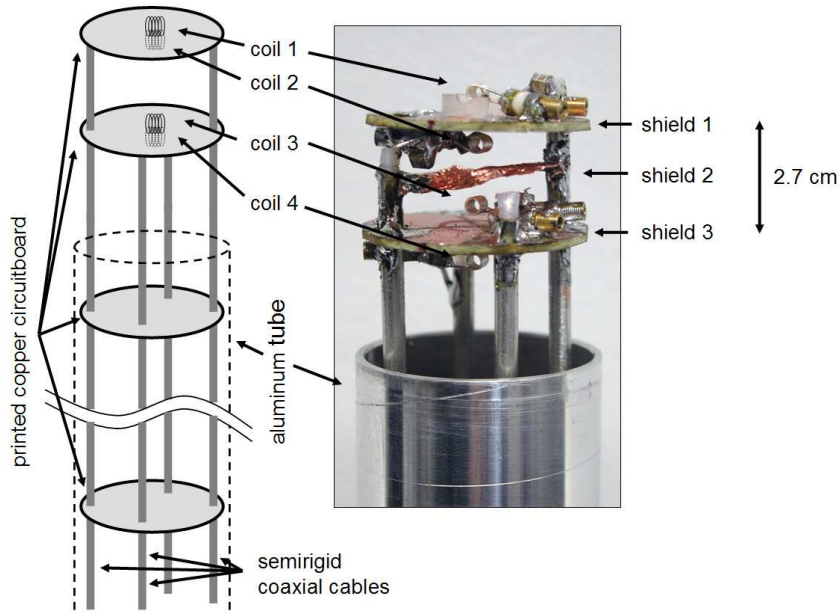


Fig. 4.1: Schematic (left) and photograph (right) of the four-channel probehead. This figure is reprinted from reference [47].

probehead for imaging multiple single-cell samples simultaneously will be described [47].

4.0.1 Probehead construction

The probehead consisted of four solenoid coils, each with an outer diameter of 2 mm, for studying the NMR relaxation properties of fresh and fixed stage VI *Xenopus laevis* oocytes. It was made out of several copper circuit boards and four grounded semirigid coaxial cables to give the probehead mechanical and electrical stability. This framework was housed inside an aluminium tube, as shown in Fig. 4.1. Each coil was a five-turn solenoid, wound with 400 μm diameter silver-coated copper wire (Conrad Elektronik, Hirschau, Germany). Spacer wire corresponding to one-half of the coil wire diameter was used for achieving the optimum wire spacing [32], and removed afterward. The coils and corresponding impedance matching circuits were placed on either side of two double-sided copper printed circuit boards (PCB). A simple L-type capacitive impedance matching network was used with variable (0.5-8 pF range, Voltronics Corp., Denville, NJ) and fixed (10 pF, American Technical Ceramics Corp., Huntington Station, NY) capacitors. Components on the circuit board were arranged so that the largest area was at ground potential, minimizing the effect of a change in dielectric environment on the circuit. Because of space constraints, no external rods were attached to the capacitors. Therefore, impedance matching the coils was only possible outside the magnet. However, inserting the probehead into the gradient system did not change the impedance match or resonant frequency of any of the coils. Before constructing the complete probehead, different electrical setups were evaluated. Because of space constraints, both the top and the bottom side of the circular circuit boards were used for probe coil and circuit mounting. These were slotted into quadrants to avoid eddy currents during the imaging experiments. Single-sided and double-sided networks were compared in terms of the

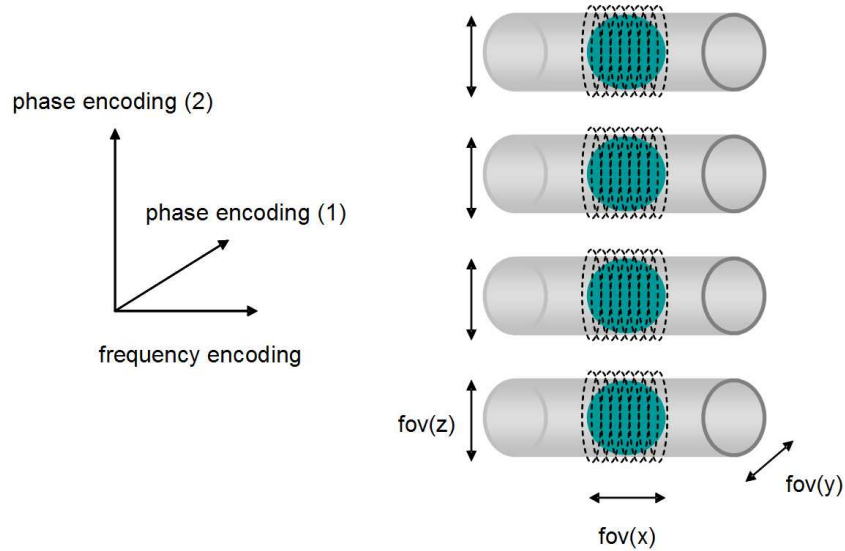


Fig. 4.2: Imaging gradients for the three-dimensional multiple-coil experiments. This figure is reprinted from reference [47].

quality factor Q and tuning range. The cross talk between two single networks on opposing sides of the two circuit boards was measured for different coil spacings and orientations at 750 MHz. Results showed that coupling originated mostly from the impedance matching networks, presumably due to electric field coupling from the capacitors. Grounding played an important role in achieving minimum coupling between networks. With the PCBs being slotted and consequently divided into four quadrants, not every copper surface was at ground potential. The grounding scheme was optimized so that maximum isolation was present between the coils.

4.0.2 Parallel data acquisition

The four-receiver channel Bruker system has, in common with many other commercial systems, a single transmitter channel. Therefore, the output of the transmitter was fed into a four-way power splitter (Mini-Circuits, Brooklyn, NY; 725 to 1050 MHz, insertion loss < 0.5 dB). For studies of relaxation times, diffusion coefficients, and membrane permeability in single cells, the spatial resolution must be sufficient to differentiate between physically distinct volumes within the cell. This means that, in practice, 3D images must be acquired [48, 49, 50, 51]. As shown in Section 2.2, the measured signal intensity of a 3D spin-echo experiment is given by

$$S(k_x, k_y, k_z) \propto \int \int \int \rho(x, y, z) e^{-2\pi i k_x x} e^{-2\pi i k_y y} e^{-2\pi i k_z z} dx dy dz \quad (4.1)$$

where x , y , and z are the frequency-, first phase-, and second phase-encoding directions, respectively. k_x , k_y , and k_z are defined in the usual k -space representation. The fields of view (FOV) in each dimension are given by:

$$FOV_x = \frac{1}{\Delta k_x}, FOV_y = \frac{1}{\Delta k_y}, FOV_z = \frac{1}{\Delta k_z} \quad (4.2)$$

Parameter	unloaded	loaded ¹
Q (coil 1)	197	64
Q (coil 2)	173	57
Q (coil 3)	154	60
Q (coil 4)	188	67
S_{21} coil 1/coil 2	-24 dB	-37 dB
S_{21} coil 1/coil 3	-36 dB	-48 dB
S_{21} coil 1/coil 4	-33 dB	-42 dB
S_{21} coil 2/coil 3	-28 dB	-36 dB
S_{21} coil 2/coil 4	-44 dB	-46 dB
S_{21} coil 3/coil 3	-32 dB	-35 dB

Tab. 4.1: Electrical characterization of the four-channel probehead

It was important that the cells all be accurately aligned in the frequency encoding direction so that the minimum FOV could be used, as shown in Fig. 4.2. In the other two phase-encoded dimensions, accurate positioning was less important as the signal is indirectly encoded, and multiplication of the k-space signal by an appropriate phase factor could be used to center the image within the FOV with no loss in sensitivity. As indicated in Fig. 4.2, the readout gradient direction was chosen along the coil axis for all experiments, with a 3D FOV set equal to that for a single cell. Because there was a high degree of decoupling between the individual coils, there was no superposition of individual signals, allowing multiple volumes of interest to be imaged without sacrificing in spatial resolution. Although this approach is related to the partially parallel imaging technique PILS [52], it is worth noting that reconstruction is performed for each FOV individually and four independent data sets are obtained. Data acquisition was performed using the physical setup shown in Fig. A.3 in the appendix where additional information is given about the actual data acquisition on the Bruker system.

4.0.3 Results

Electrical characterization

Electrical measurements for the four-coil probehead are presented in Table 4.1. The ratio of unloaded to loaded quality factor $Q_{\text{unloaded}}/Q_{\text{loaded}}$ was about three, which is typical for this case in which both coil and sample losses were important (i.e., there was no single dominant source of loss). Decoupling between all of the coils was 35 dB or better with samples in place.

NMR experiments

The particular imaging experiments performed to test the probehead were acquiring T_1 maps of fixed stage VI *Xenopus laevis* oocytes. The NMR sequence is described in detail in Section 3.1. This forms part of the study described in Chapter 7 that is investigating the reversible and irreversible effects of chemical fixation (and subsequent reimmersion

¹ The sample was 100 mM NaCl in water.

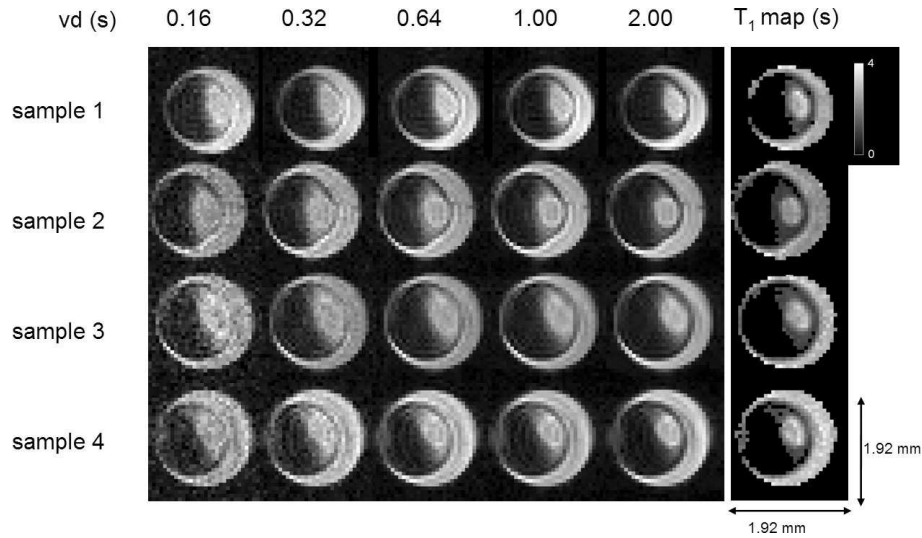


Fig. 4.3: Slices from simultaneously acquired datasets with variable delays (left to right) using the four-channel probehead, corresponding T_1 maps shown on the right. This figure is reprinted from reference [47].

in buffer) on cellular structures and tissues. In this experiment, the oocytes were fixed in 4% formaldehyde solution after defolliculation and transferred to Barth's solution (88 mM NaCl, 1 mM KCl, 0.41 mM CaCl₂, 0.33 mM Ca(NO₃)₂, 0.82 mM MgSO₄, 2.4 mM NaHCO₃, and 10 mM HEPES) after 2 hours of fixation. The obtained datasets, shown in Fig. 4.3, showed no ghosting artifacts, corroborating the good isolation of all four probe coils.

Values for the nucleus, animal pole, and medium (as a control) are shown in Table 4.2. These values were calculated using a region of interest (ROI) placed in the nucleus, animal pole, or medium, respectively, in a single slice of the 3D data set. Values for the medium show that quantitative results within experimental error can be obtained using this probehead. This confirms experimental observations that the pulse widths for all coils were within 5% of each other, and that the results from multiple samples were the same as those in which only one sample was placed in one of the coils.

² SD: standard deviation; sem: standard error

	T_1 (s) Mean \pm SD (sem) ²	No. of Pixels
<i>Coil 1</i>		
nucleus	2.75 \pm 0.29 (0.05)	36
animal pole	1.18 \pm 0.18 (0.04)	17
medium	2.61 \pm 0.23 (0.04)	36
<i>Coil 2</i>		
nucleus	2.71 \pm 0.20 (0.05)	18
animal pole	1.13 \pm 0.14 (0.03)	25
medium	2.84 \pm 0.44 (0.07)	42
<i>Coil 3</i>		
nucleus	2.80 \pm 0.45 (0.09)	26
animal pole	1.16 \pm 0.19 (0.03)	50
medium	2.85 \pm 0.45 (0.07)	37
<i>Coil 4</i>		
nucleus	2.53 \pm 0.38 (0.09)	18
animal pole	1.03 \pm 0.22 (0.02)	45
medium	2.77 \pm 0.45 (0.07)	45

Tab. 4.2: Calculated T_1 values

5. SUSCEPTIBILITY MATCHING

In a common type setup, a solenoid coil constructed of copper wire is wound on a glass capillary. There are three regions with different magnetic susceptibility χ . The biggest difference in susceptibility is the variation from copper to air. As a result, the magnetic field in close proximity to the coil windings will be distorted, causing unwanted artifacts in NMR imaging and line broadening in NMR spectroscopy.

For a simplified mathematical description, an infinitely long cylindrical piece of copper representing a piece of wire is assumed to be surrounded by air in a region of static magnetic field B_0 . The local magnetic field variation ΔB at distance r and angle ϕ around the copper cylinder with magnetic susceptibility χ_i is given by [53]:

$$\Delta B \approx \frac{B_0 \sin^2 \theta \cos 2\phi}{2r^2} R^2 (\chi_e - \chi_i) \quad (5.1)$$

where χ_e is the susceptibility of air, R is the cylinder radius and θ is the angle between the cylinder axis and static magnetic field according to Figure 5.1. The highest field distortion occurs if the cylinder is oriented perpendicularly to the external magnetic field, $\theta = 90^\circ$. The field variation has the shape of a two-dimensional dipole field due to the dependence on $\cos 2\phi$.

In order to reduce the field inhomogeneity, the concept of susceptibility matching was introduced by D. Olson [29] by immersing a sub-millimeter-sized microcoil in perfluorinated carbon (perfluorotributylamine, commonly known as Fluorinert FC-43; 3M Corporation, Minneapolis, MN, USA). The magnetic susceptibility of FC-43 lies within 15% of that of copper¹. FC-43 is chemically stable and safe to handle at room temperature and above; it evaporates at temperatures between 165°C and 185°C and shows hazardous decomposition above 200°C, making it unsuitable for high temperature applications such as gas chromatography coupled NMR (GC-NMR) experiments of substances with high boiling points. Also, a variety of ¹³C spectral lines between 106 and 120 ppm [54] provide a significant background signal in carbon experiments, especially when studying aromatic compounds in the same frequency range.

5.1 Alternative substances

Various applications provide a demand for alternative ways of susceptibility matching: higher operational temperature and reduced carbon background signal are among the desired prerequisites. The requirement for any substance is the absence of proton signal, absence or reduction of carbon signal and elevated temperatures of evaporation and dissociation. The magnetic susceptibility of potentially useful substances to be considered

¹ volume magnetic susceptibilities in SI-system: $\chi_{Cu} = -9.65 \cdot 10^{-6}$, $\chi_{FC-43} = -8.23 \cdot 10^{-6}$, $\chi_{air} = +0.30 \cdot 10^{-6}$, also see Table 4.4

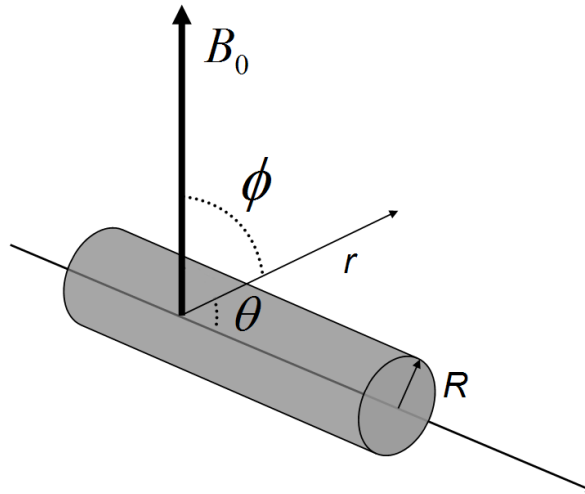


Fig. 5.1: Infinite cylinder in a static magnetic field

Substance	FC-43	BTCM	Fomblin Y25
Molecular formula	$(\text{CF}_3\text{CF}_2\text{CF}_2\text{CF}_2)_3\text{N}$	CBrCl_3	see Sec. 5.1.2
CAS Number	311-89-7	75-62-7	-
Molecular weight (g mol^{-1})	671.00	198.27	3200.0
Density at 20 °C (g cm^{-3})	1.86	2.01	1.90
Boiling point (°C)	178	105	> 250
Hazard Codes	-	Xn	-

Tab. 5.1: Chemical and physical properties of FC-43, BTCM and Fomblin Y25

is unknown and has to be determined experimentally. A suitable method is described in Section 5.3, along with experimental results obtained from various substances. An overview of physical and chemical parameters of the gold-standard substance FC-43 and the two alternate substances BTCM and Fomblin Y25 that have been evaluated in this work is given in Table 5.1.

5.1.1 BTCM

One substance potentially suitable for matching is bromotrichloromethane (BTCM). Its empirical formula is CBrCl_3 ; 100 ml of 98% pure substance was obtained from Sigma-Aldrich (St Louis, MS, USA).

While BTCM requires additional precautions according to the hazard code, its ^{13}C -spectrum is only composed of a single line at 67.44 ppm due to its simple molecular structure [55]. The ratio of total signal obtained from BTCM to the total signal from FC-43 has been estimated by calculating the number of carbon atoms (N_C) per unit volume. With 12 carbon atoms per molecule for FC-43 and one per molecule for BTCM, the ratio can be calculated:

$$\frac{N_{\text{C,BTCM}}}{N_{\text{C,FC-43}}} = \frac{N_{\text{BTCM}}}{12 \cdot N_{\text{FC-43}}} = \frac{\rho_{\text{BTCM}} \cdot M_{\text{FC-43}}}{12 \cdot \rho_{\text{FC-43}} \cdot M_{\text{BTCM}}} \approx 0.305 = 3.28^{-1} \quad (5.2)$$

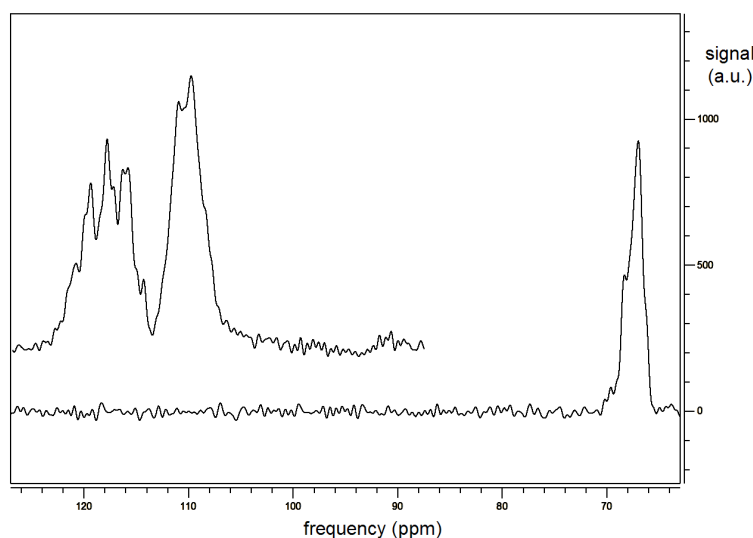


Fig. 5.2: ^{13}C background spectra of BTCM (bottom) and FC-43 (top)

where N is the number of atoms, M is the molecular weight and ρ is the density. A given volume of BTCM provides one third of the signal FC-43 would, assuming no relaxation effects. This ratio has also been verified experimentally. A five-turn solenoid coil operating at the Larmor frequency of ^{13}C at 17.6 T (188.5 MHz) was wound on a 1 mm capillary using 200 μm copper wire and placed in a container that was filled with FC-43. No sample was placed inside the coil. After the NMR experiment was carried out on FC-43 as described below, the container was emptied, cleaned, filled with BTCM, and the experiment was repeated. The ^{13}C background signal was measured by acquiring an FID from a single pulse (pulse length 4 μs at 20 dB transmitter attenuation using a 500 W Bruker BLAX500 X-Channel RF amplifier). Acquisition was carried out using a sweep width of 50 kHz, 2048 complex data points, a relaxation delay of 0.5 s and 2048 averages resulting in a total acquisition time of 17 minutes. The acquired spectra are shown in Figure 5.2. Spectra were processed with MestRec, signal integration was performed between 64 and 72 ppm (BTCM) and 106 and 124 ppm, respectively (FC-43). The integrated signal obtained from BTCM was 52055 in arbitrary units, the signal obtained from FC-43 was 192921. The resultant ratio obtained from the integrated signals was 0.270 or 3.70^{-1} , which is $\approx 11.5\%$ lower than the theoretically obtained value. The acquisition of FIDs excludes any effects resulting from differences in relaxation times.

The capability of BTCM for susceptibility matching was evaluated using a 1 mm solenoid coil wound of five turns of copper wire with 400 μm diameter. The coil was wound directly on a 1 mm o.d. borosilicate glass capillary (Hilgenberg GmbH, Germany). The capillary was glued into a plastic container that allowed filling with BTCM. NMR experiments were either performed with an empty container (coil surrounded by air) or with a BTCM-filled container. The sample was Millipore water. The FID signal was acquired after a $\pi/2$ pulse.

With air surrounding the coil, a spectral line $FWHM = 145$ Hz was obtained after shimming on first, second and third order shim coils. Immersion of the coil in BTCM and subsequent shimming leads to a line $FWHM = 17$ Hz. Obtained spectra are shown in

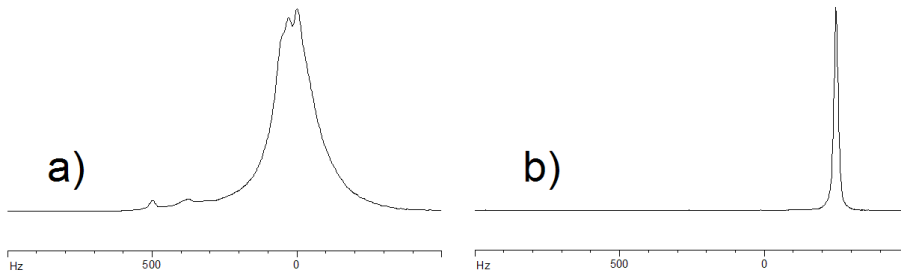


Fig. 5.3: ^1H spectra of water sample in 1 mm copper solenoid coil; (a) coil surrounded by air, $FWHM = 145$ Hz; (b) coil immersed in BTCM, $FWHM = 17$ Hz; note that the signal scale is different between (a) and (b)

Figure 5.3. The experiment was also repeated with a smaller solenoid (0.7 mm diameter). After immersion and shimming, a linewidth of $FWHM = 14$ Hz was obtained.

5.1.2 Fomblin

The prerequisite of susceptibility matching operation at elevated temperature requires substances that have higher inter- and intramolecular bonding forces, macroscopically expressed as higher viscosity. One family of such proton-free viscous substances are perfluoropolyethers (PFPEs), commercially known as Fomblin (Solvay Solexis). Unlike FC-43, Fomblin substances are composed of mixtures of molecules with the formula $(\text{CF}_3-[(\text{O}-\text{C}_2\text{F}_4-\text{CF}_2)_m-(\text{O}-\text{CF}_2)_n]\text{O}-\text{CF}_3)$ with $m+n=8-45$ and $m/n=20-1000$. PFPEs have been studied spectroscopically with NMR [56] and their usefulness for susceptibility matching of biological samples in proton-free media is well-known [57, 58], although the actual magnetic susceptibility value has not been measured. In order to estimate the potential of low-viscosity PFPE lubricants, the magnetic susceptibility of Fomblin Y25 has been determined experimentally using the modified Reilly-McConnel-Meisenheimer-method [59] (see Section 5.3). Fomblin Y25 is thermally stable up to temperatures of 290°C , although evaporation occurs above 150°C . A 0.7 mm solenoid coil was used to determine the amount of susceptibility matching obtained by using Fomblin Y25. A single FID of a water sample was acquired under various shim and immersion conditions. The obtained spectra are shown in Fig. 5.4: immersing the coil in Fomblin Y25 led to a linewidth reduction from 500 Hz to 50 Hz with no shim currents in any case; subsequent shimming on first, second and third order shim coils led to a linewidth of 4 Hz.

5.2 The dipole field around a capillary

The susceptibility of a fluid sample (χ_s) is measured by placing a glass capillary (χ_g) perpendicularly into a magnetic field B_0 ($\theta = 90^\circ$). The capillary has an inner diameter $2a_1$ and an outer diameter $2a_2$. It is surrounded by water (χ_w) and contains the sample of unknown susceptibility (χ_s). The field offset created by such a setup has been derived [60] by solving the Maxwell equations analytically for this particular setup:

$$\Delta B(r) = \frac{B_0 \cos 2\phi}{r^2} \left[-\frac{1}{2} \left(1 + \frac{\chi_w}{3} \right) \right] [a_1^2(\chi_g - \chi_s) + a_2^2(\chi_w - \chi_g)]. \quad (5.3)$$

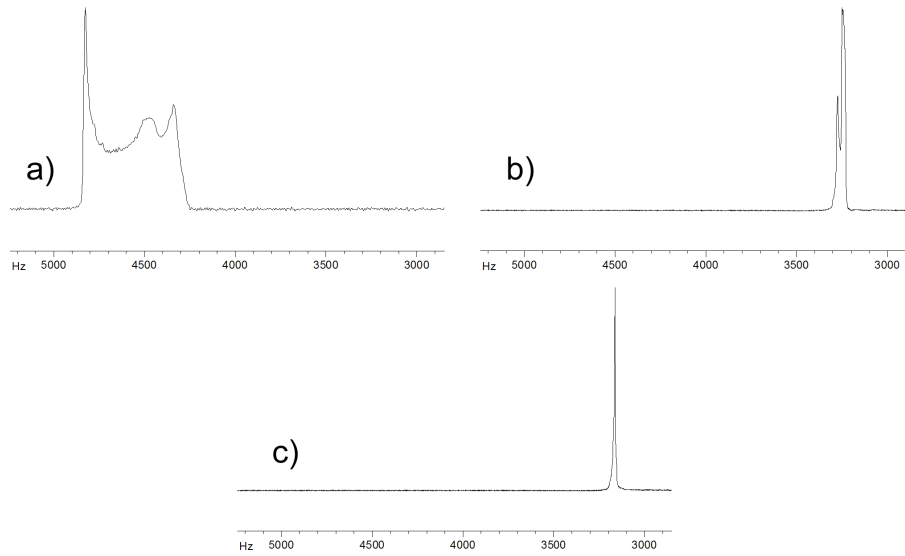


Fig. 5.4: ^1H spectra of water sample in 0.7 mm copper solenoid coil; (a) coil surrounded by air, unshimmed (no shim current in any shim coil), $FWHM = 500$ Hz; (b) coil immersed in Fomblin Y25, unshimmed, $FWHM = 50$ Hz; (c) coil immersed in Y25, after shimming, $FWHM = 4$ Hz

The susceptibility of water is $\chi_w = -9.04 \cdot 10^{-6}$. It is significantly smaller than 1, and the above equation can be simplified:

$$\Delta B(r) \approx -\frac{B_0 \cos 2\phi}{2r^2} [a_1^2(\chi_g - \chi_s) + a_2^2(\chi_w - \chi_g)]. \quad (5.4)$$

5.3 Measurement of susceptibility

A 5 mm glass tube was glued perpendicularly into a 15 mm plastic centrifuge tube and was hereafter filled with millipore water. A borosilicate glass capillary (Hilgenberg GmbH, Germany) with an inner diameter $2a_1 = 1.05$ mm and outer diameter $2a_2 = 1.5$ mm was filled with the respective substance of unknown susceptibility and placed inside the 5 mm tube (see Figure 5.5). The lower volume of the centrifuge tube was filled with FC-43 to reduce any field distortion at the outer region of the 5 mm tube volume. The whole phantom was placed inside a Bruker 20 mm linear birdcage coil. The field was mapped using a CSI sequence. The imaging parameters were 32×32 phase encoding steps at a FOV of 4.48×4.48 mm², resulting in a spatial resolution of $(140 \mu\text{m})^2$. The slice thickness was 1 mm. In the spectroscopic dimension, 4096 complex points were acquired over an acquisition time of 1.0 s and thus a resolution of 1 Hz/point. Total acquisition time was 37 minutes with two averages. The data set was zero filled to 64×64 spatial points, and a Fourier transform was carried out. The actual field map was obtained from the spectral position of maximum signal value. Hereafter, an image was computed by integrating over the spectrum, and a mask was obtained by thresholding at 25% of the maximum image value. A representative map is shown in Figure 5.6. Due to the dipole character of the field in Eq. (5.3), the data were fitted to the equation

$$\Delta B(r, \phi) = \frac{c \cdot \cos 2\phi}{r^2} + d \quad (5.5)$$

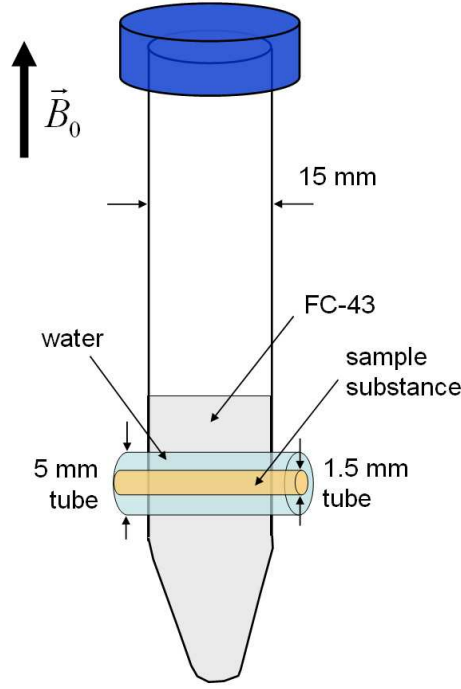


Fig. 5.5: Phantom for susceptibility measurements

by first extracting the circular paths according to $\cos 2\phi$ for known radii. Hereafter, the fit with respect to $1/r^2$ was carried out. Data points and the respective fit function are shown exemplarily in Figure 5.7. Knowing the fit parameter c , the unknown susceptibility χ_s of the substance in the inner capillary can be calculated using Eq. (5.4) and (5.5):

$$\chi_s = \frac{2c}{a_1^2 B_0} + \frac{a_2^2}{a_1^2} (\chi_w - \chi_g) + \chi_g. \quad (5.6)$$

The susceptibility of the glass capillary χ_g was also unknown, hence the inner capillary was filled with water ($\chi_s = \chi_w$) and the susceptibility of the capillary was determined from the resulting dipole field. A number of samples have been examined; the magnetic susceptibility of some examined samples is known, and the experiment was carried out in order to confirm the validity of the method. Three samples consisted of iron oxide particles in solution (see Chapter 9) for details. For those samples, it was necessary to consider the magnetization instead of the susceptibility due to the ferromagnetic/superparamagnetic nature of iron oxide particles.

The standard deviation σ_{χ_s} of the measured susceptibility according to Eq. (5.6) was calculated using error propagation theory, which yielded the equation:

$$\sigma_{\chi_s}^2 = \frac{4}{a_1^4 B_0^4} \sigma_c^2 + \left(1 - \frac{a_2^2}{a_1^2}\right)^2 \sigma_{\chi_g}^2 + \frac{a_2^4}{a_1^4} \sigma_{\chi_w}^2 + \frac{4a_2^2 (\chi_g - \chi_w)^2}{a_1^4} \sigma_{a_2}^2 + \frac{4(2c + a_2^2 B_0 (\chi_w - \chi_g))^2}{a_1^6 B_0^2} \sigma_{a_1}^2. \quad (5.7)$$

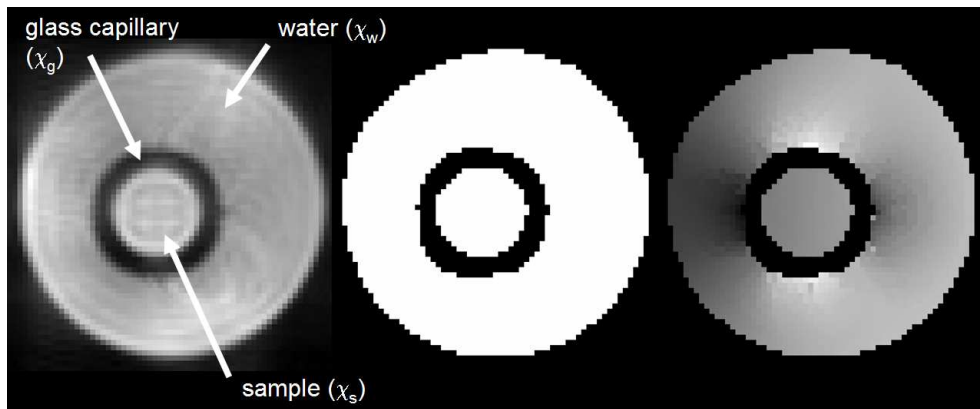


Fig. 5.6: Images obtained from CSI data set using millipore water as a sample to determine the glass susceptibility: (left) maximum intensity, (center) mask obtained by thresholding, (right) field map after multiplication with mask

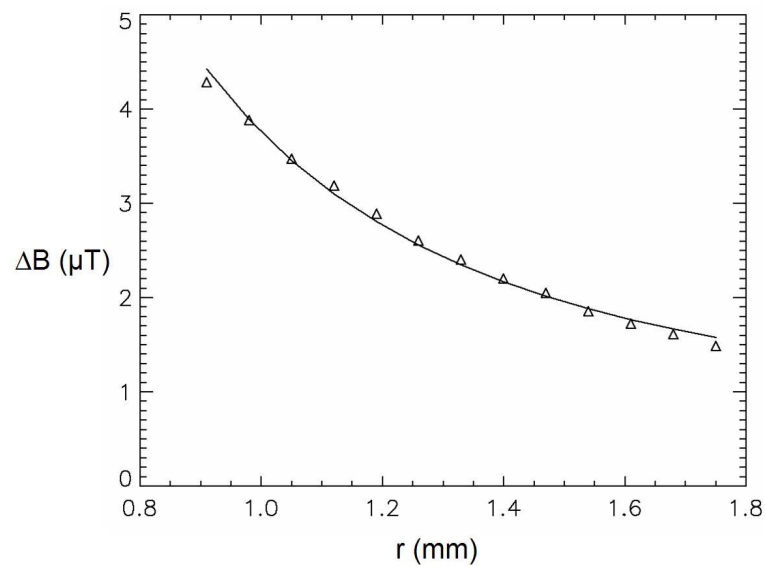


Fig. 5.7: Corresponding radial fit according to Eq. (5.5) of ΔB map shown in the right image of Fig. 5.6

Substance	measured $\chi_V (\times 10^{-6})$	literature value for $\chi_V (\times 10^{-6})$ [ref.]
Acetone	-5.76 ± 1.36	-5.78 [61]
Air	-0.46 ± 2.07	+0.3
Fluorinert FC-43	-8.49 ± 0.87	-8.23 [29]
BTCM (CBrCl ₃)	-9.32 ± 0.81	-9.30 [61]
Fomblin Y25	-8.54 ± 0.84	-
Resovist 5mM Fe*	-7.21 ± 0.80	-
VSOP 5mM Fe*	-6.78 ± 0.87	-
MACS 1:3*	-8.58 ± 0.94	-

Tab. 5.2: Volume magnetic susceptibility values for various substances obtained from CSI experiment (SI units, mean \pm SD); *for those samples, χ_V has to be replaced by the sample magnetization $\mu_0 M_s / B_0$

5.4 Results and Discussion

All measured susceptibilities are presented in Table 5.2. The susceptibility of the glass was determined to be $\chi_g = -10.3 \cdot 10^{-6}$. A general observation is that data obtained from samples having a susceptibility close to that of glass and water is closer to the literature value.

The susceptibility value obtained for BTCM (-9.32×10^{-6}) leads to a susceptibility difference between copper and BTCM of $\Delta\chi_{\text{Cu,BTCM}} = 0.33 \times 10^{-6}$, while the difference between copper and Fomblin Y25 is $\Delta\chi_{\text{Cu,Y25}} = 1.11 \times 10^{-6}$. Comparing the susceptibilities of copper and FC-43, a difference of $\Delta\chi_{\text{Cu,FC-43}} = 1.16 \times 10^{-6}$ is obtained ($\Delta\chi_{\text{Cu,FC-43lit.}} = 1.42 \times 10^{-6}$ when comparing with the literature value). The *FWHM* of a spectral line is proportional to the field offset ΔB and thus proportional to the susceptibility difference $\Delta\chi$.

Practical use of both BTCM and Fomblin Y25 was demonstrated by determining the linewidth improvement obtained by immersing an RF solenoid coil in the respective substance. Achieving linewidths below 10 Hz using small coils was possible using Fomblin Y25. However, linewidth improvement from BTCM was always inferior to matching with Fomblin Y25, lowest *FWHM* values on water samples being around 14 Hz. Although the difference in magnetic susceptibility between Fomblin Y25 and copper is higher than the difference between BTCM and copper, matching using Fomblin Y25 is more effective. Results suggest that minimized susceptibility difference between copper and matching liquid might not be the only prerequisite. Further clarification is necessary with focus on viscosity, which seems to be another pivotal factor.

Results obtained from iron oxide particle solutions will be addressed in Chapter 9.

6. NMR MICROSCOPY OF *P. TRIANGULUM*

Philantus triangulum, also known as the European beewolf, is a solitary, predatory wasp that preys on bees, but also feeds on pollen and nectar. In collaboration with the Department of Animal Ecology and Tropical Biology and the Department of Animal Physiology and Sociobiology at the University of Würzburg and the Institute of Zoology at the University of Regensburg, a *P. triangulum* head was imaged in order to nondestructively reveal the position and dimension of a large cephalic gland in the head. The aim was to verify whether this gland was a postpharyngeal gland (PPG), as present in workers and queens of ants. The feasibility and the advantages of NMR microimaging in entomology have been shown [62, 63] and reviewed [64] in the past. In this project [65], NMR served as a complementary method, along light microscopy, electron microscopy and biochemical analysis, allowing the nondestructive visualization of the gland inside the head. Additionally, glands in different segments of the antenna have been imaged with a microcoil setup.

6.1 Imaging of the head

6.1.1 Methods

A male beewolf (head width 3.3 mm) was anesthetized in CO₂ and killed with diethyl ether. After decapitation the head was immersed in 100% ethanol and kept for one hour in an exsiccator with water jet vacuum. In this process, the air sacs were filled with liquid in order to avoid susceptibility artifacts in the imaging experiment caused by air-tissue transitions. The head was transferred to a 5 mm NMR tube filled with water and 5 mM Gadovist (Schering, Berlin, Germany) as a contrast agent and evacuated for another 30 minutes. A 5 mm commercial birdcage coil (Bruker Analytik, Rheinstetten, Germany) was used as transmit-receive RF coil. Three-dimensional data sets were obtained using a 3D FLASH sequence with selection of a 2 mm slice in the second phase encode direction. Data acquisition parameters were $T_R = 40$ ms, $T_E = 3.0$ ms, number of averages $N_A = 6$, a data matrix of $512 \times 256 \times 128$ complex points and a FOV of $(5.0 \times 5.0 \times 2.5)$ mm³, yielding an isotropic spatial resolution of $(20 \mu\text{m})^3$. Total data acquisition time was 4.4 hours.

The preparation of the beewolf head and the three-dimensional reconstruction based on the NMR data using the 3D visualization software AMIRA (Indeed-Visual Concepts, Berlin, Germany) were performed by Wolfgang Göttler (Institute of Zoology at the University of Regensburg). No evidence for any artifact caused by the preparation was found, as the results coincide with structures inferred from the histological analysis.

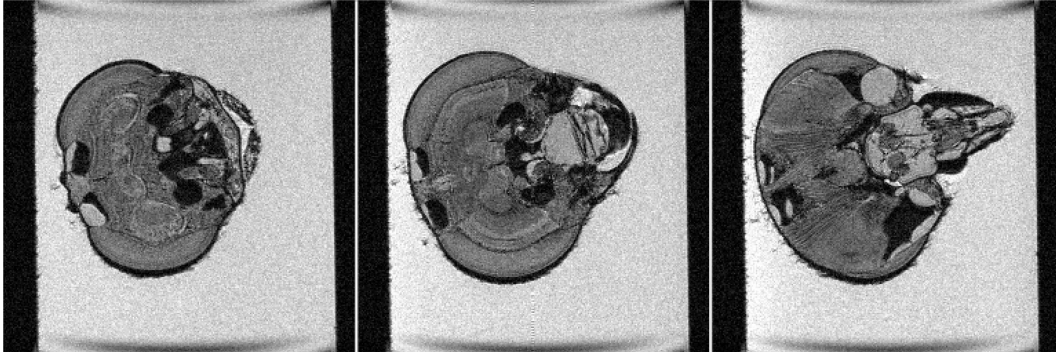


Fig. 6.1: Individual slices from 3D data set of the beewolf head; spatial resolution $(20 \mu\text{m})^3$

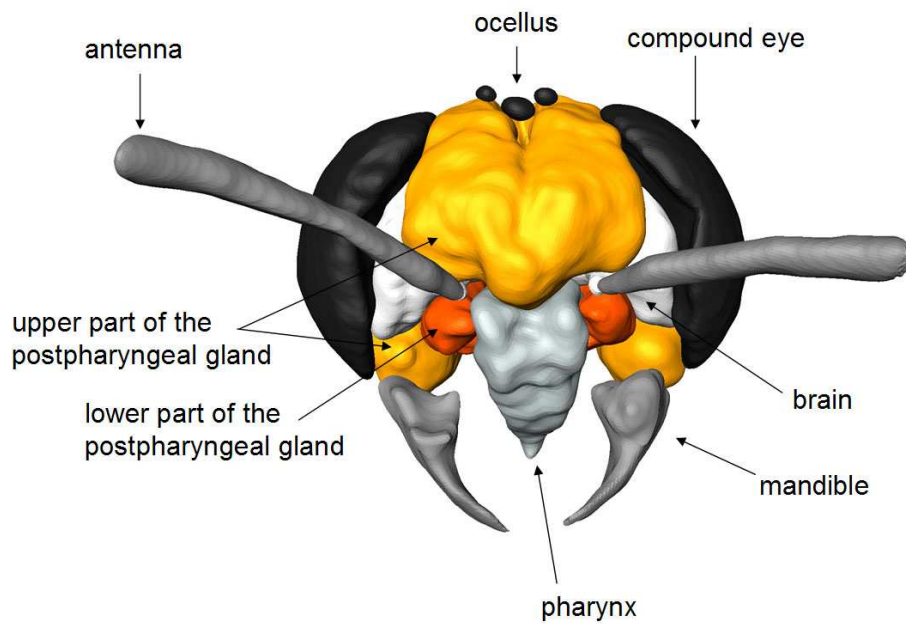


Fig. 6.2: 3D reconstruction of the beewolf head (front). This figure is reprinted from reference [65].

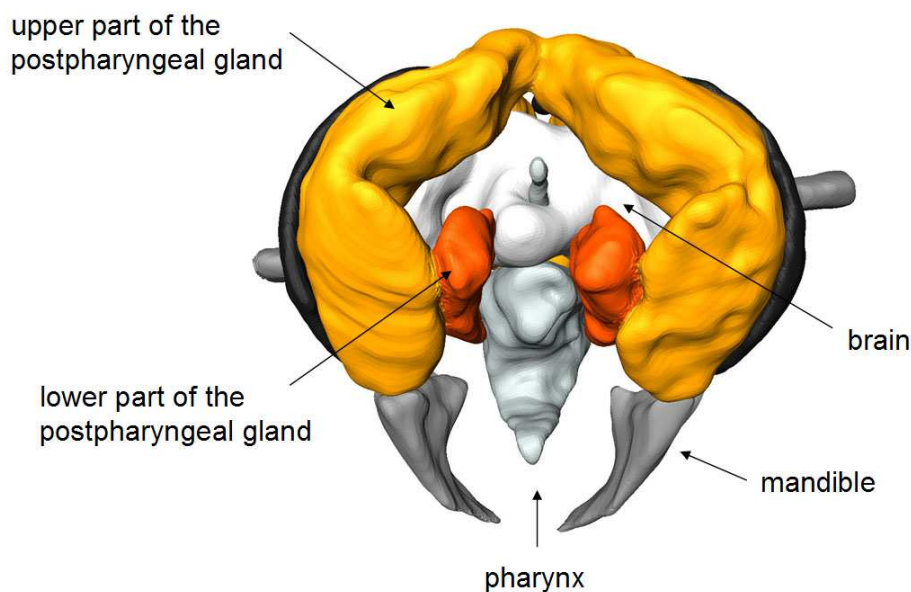


Fig. 6.3: 3D reconstruction of the beewolf head (rear). This figure is reprinted from reference [65].

6.1.2 Results and Discussion

Individual slices of the complete data set of the head are shown in Fig. 6.1. Three-dimensional reconstructions of the NMR data with an outline of the depicted structures are presented in Figs. 6.2 and 6.3. The reconstructed data allowed volume determination: the volume of the upper PPG was $2.12 \mu\text{l}$, the lower part $0.41 \mu\text{l}$, while the volume of the head capsule was determined to be $9.3 \mu\text{l}$. The total PPG occupies approximately 25% of the head capsule volume.

The NMR microscopy was very useful to determine the actual position and shape inside the head and confirm findings obtained from semi-thin sections. As already pointed out in Section 4, experiment time on high field systems is usually limited, requiring experiments to be as efficient as possible. Combining high magnetic field strength, strong gradients, addition of Gadolinium for T_1 -reduction and an RF coil allowing for a high filling factor, the complete head could be imaged at a sufficiently high spatial resolution in a relatively short data acquisition time and with short sample preparation time. All desired target structures could be identified.

6.2 Imaging of the antenna

Females of the European beewolf have been found to secrete large quantities of a white substance from antennal glands. The substance has been examined and it was found that it contained large quantities of *Streptomyces* bacteria. Certain segments in the antenna contain reservoirs that allow symbiotic growth of those bacteria [66]. The substance containing the bacteria is deposited on the breed cell walls and is hereafter taken up by beewolf larvae. Those bacteria have been shown to protect the cocoon from fungal infestation, possibly due to production of antibiotics.

The symbiosis between various beewolf species and bacteria is of great interest to

evolutionary biology. It has been hypothesized that the glands grew in size along with progressive symbiosis. In order to verify this hypothesis, it is necessary to compare the anatomy of the antennal glands of various beewolf species to the genealogy of the corresponding bacteria. The antenna of female beewolves consists of 12 segments, denoted A1 through A12. Segments A4 through A8 contain the respective glands. The classical histological method of semithin sectioning followed by digitizing of the images is hardly suitable for systematical analysis due to the high number of sections necessary in the longitudinal direction of the antenna. Certain beewolf species are rare; the antennae are valuable and cannot be sacrificed for sectioning. NMR microimaging as a noninvasive imaging method is favorable for the acquisition of three-dimensional morphological data. A small solenoid is ideally suited as RF coil due to the long cylindrical shape of the antenna.

6.2.1 Methods

An isolated antenna has been imaged using a microcoil with a geometry that was specially tailored for optimal filling factor and sensitivity. The left antenna of a female beewolf was fixed in a mixture of 2% formaldehyde and 0.1 M PBS for 27 h. Hereafter, it was washed and reimmersed in 1 M PBS and 2 mM Gadolinium. The antenna was brought into a fused silica glass capillary (700 μm o.d., 530 μm i.d., Polymicro Technologies, Inc.) and had to be immobilized using a second capillary that was smaller in diameter. The RF coil used was a 1 mm homebuilt solenoid coil that was wound on a 1 mm o.d., 720 μm i.d. borosilicate glass capillary (Hilgenberg, Germany) and susceptibility-matched with FC-43.

Three-dimensional imaging was carried out using a 3D gradient echo sequence, an echo time $T_E = 2.8$ ms, a repetition time $T_R = 75$ ms and $N_A = 48$ averages. The FOV was $4.1 \times 0.8 \times 0.8$ mm³ with an imaging matrix of $1024 \times 100 \times 100$ complex points, resulting in an isotropic spatial resolution of 8 μm .

6.2.2 Results and Discussion

The morphological image data obtained allows the identification of individual antennal segments. The signal contrast within the segments allows identification of larger structures; however, tissue heterogeneity and possibly susceptibility-induced artifacts complicate a precise mapping of smaller structures. In segments A4 through A8, the reservoir glands can be identified and their shape indicates that they have collapsed. At the surface of the antenna, various artifacts can be observed, probably due to field distortions from air bubbles. This can be overcome by using a spin echo sequence instead. However, the SNR efficiency of a spin echo experiment is inferior to the gradient echo sequence and the same spatial resolution can not be obtained in the same experiment time. Therefore, it has to be explored whether it is possible to degas such a small sample prior to the experiment. In summary, NMR microscopy on beewolf antennae with focus on the reservoir glands is promising, potentially eliminating the need for histological sectioning.

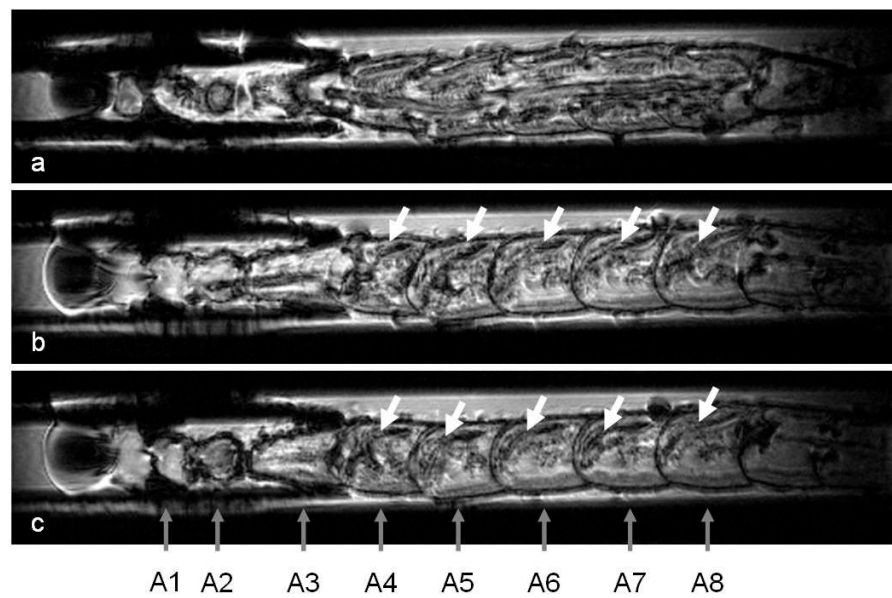


Fig. 6.4: Beewolf antenna; three individual slices from the $(8 \mu\text{m})^3$ isotropic dataset; white arrows indicate positions of the five reservoir glands; distance from slice a to slice b is $120 \mu\text{m}$, distance from slice b to slice c is $32 \mu\text{m}$.

7. CHEMICAL FIXATION OF SINGLE CELLS

The usefulness of NMR microscopy on *ex vivo* samples has been shown in the last chapter, where high-resolution three-dimensional images of chemically fixed samples were acquired non-invasively. This methodology is typically referred to as "magnetic resonance histology". It was originally formulated by Johnson and coworkers [67] using the example of morphological phenotyping. Among recent applications are the production of three-dimensional MRI [68, 69] and multi-modal [70] atlases of the mouse brain and multi-modal neurotoxicity evaluations [71]. While the spatial resolution of NMR histology is much inferior to light and other forms of microscopy, the advantages include true three-dimensional data acquisition, the lack of morphological changes associated with tissue dehydration and sectioning, and reduced data processing time compared to histological sectioning. The non-invasive nature of NMR histology is particularly important when the samples are unique and irreplaceable [72], for example having been collected over a long period of time [45].

As for many microscopy studies, tissue specimens for NMR histology are typically fixed in buffered solutions of formaldehyde, which is the most common fixative. This chemical fixation destroys autolytic enzymes, preserves tissue from decomposition due to bacteria or moulds, and adds rigidity to very fragile tissue. Formaldehyde dissolves in water to form methylene hydrate, $\text{HO-CH}_2\text{-OH}$, which in its monomeric form is the active fixation agent [73]. Formaldehyde's mechanism of action is based on the reaction of the aldehyde group with primary amines in proteins. The initial reaction of formaldehyde with protein is complete within 24 hours, but the formation of cross-links, or methylene bridges, between neighbouring proteins (if the primary amines are close enough together) can take several weeks. Since formaldehyde penetrates tissue rapidly, the rate-limiting step for fixation is the cross-linking process. Another common fixative, glutaraldehyde, has two aldehyde groups separated by three methylene bridges, which greatly increases the crosslinking compared to formaldehyde. Reaction with proteins is faster for glutaraldehyde than for formaldehyde, but its physical penetration through tissue is slower.

Given the importance of *ex vivo* NMR studies, many studies have investigated how chemical fixation affects NMR parameters such as relaxation times and diffusion coefficients. In general, T_1 and T_2 relaxation times have been found to decrease upon chemical fixation, with T_2 affected to a significantly greater degree than T_1 [74]. The major mechanism for this reduction is chemical exchange between water and the protons in the aldehyde group of the fixative. Many groups have performed experiments on animal [75] and human [76, 77] tissue in order to understand both the altered contrast mechanisms in fixed tissue compared to *in vivo* imaging, and also to optimize the imaging parameters for fixed tissue samples. Although the actual changes varied quite significantly, T_1 and T_2 times generally decreased after fixation.

In terms of the effects of chemical fixation on diffusion, Pattany et al. [78] showed that

diffusion anisotropy was preserved in white matter tracts of fixed cat spinal cords. While the ADC values dropped in the longitudinal direction after about two weeks of fixation, it was relatively constant in the transverse direction. Obviously, tissue heterogeneity and anisotropy makes the exact mechanism of chemically induced changes difficult to determine, a number of simplified models have been developed. One model that has been recently used by Thelwall and coworkers [79] are erythrocyte ghosts derived from human blood to study the influence of temperature and fixation on relaxation times and diffusion. Results showed that a temperature increase resulted in an increase in the extracellular ADC of water and increased water exchange between the tortuous extracellular compartment and the diffusion-restricted intracellular compartment. Fixation has been shown to slightly reduce the extracellular ADC; washing restores the extracellular ADC to values prior to fixation and increases the T_2 compared to the initial value.

This project does not only focus on the changes in NMR properties from chemical fixation, but also in what NMR data can infer about the reversibility of such changes upon reimmersion in buffer. Since the T_2 , in particular, is shortened by fixation, many studies of *ex vivo* tissue reimmerse the fixed tissue in some form of aqueous buffer in order to increase the T_2 value [80]. However, with the exception of the aforementioned papers of Pattany [78] and Thelwall [79] there are relatively few published data on whether the NMR parameters return to those of the fresh tissue, and therefore whether measured relaxation times and diffusion coefficients can be related directly to the *in vivo* situation. In order to answer some of these questions, a well-studied single cell model, namely Stage VI oocytes from *Xenopus laevis*, has been used in order to determine the effects of chemical fixation on NMR parameters and also the effects of reimmersion in buffer solution.

7.1 The *X. laevis* oocyte as a model organism

The African clawed frog *Xenopus laevis* is a common model organism in developmental biology due to short generation times, large and robust egg cells and embryos that are easily accessible. From an NMR point of view, the oocyte is a good model because of its intracellular contrast. The nucleus is easily distinguished from the cytoplasm, which itself consists of an animal and vegetal pole, the latter having a relatively high lipid concentration. Aguayo et al. [8] achieved the first single cell NMR images of *X. laevis* oocytes. A number of rigorous, quantitative studies on the same cell type have already been performed by Sehy et al., in which intracellular relaxation times and apparent diffusion coefficients (ADCs) of water and lipid have been measured at 4.7 T, at a high spatial resolution necessary to avoid partial volume effects [48, 50, 49, 51, 81].

7.2 Cell preparation

Stage VI *X. laevis* oocytes with a diameter of approximately 1.2 mm were harvested, defolliculated and divided into two groups. Six cells were placed in Barth's solution (90 mM NaCl, 1 mM KCl, 0.8 mM $\text{MgSO}_4 \cdot 7 \text{H}_2\text{O}$, 0.3 mM $\text{Ca}(\text{NO}_3)_2 \cdot 4 \text{H}_2\text{O}$, 0.4 mM $\text{CaCl}_2 \cdot 2 \text{H}_2\text{O}$, 2 mM NaHCO_3 , 10 mM HEPES). Sixteen cells were placed in fixative (4% formaldehyde in Barth's solution). Cells were prepared by Dr. Stefanie Glaser at the Department of Cell and Developmental Biology, University of Würzburg. After approxi-

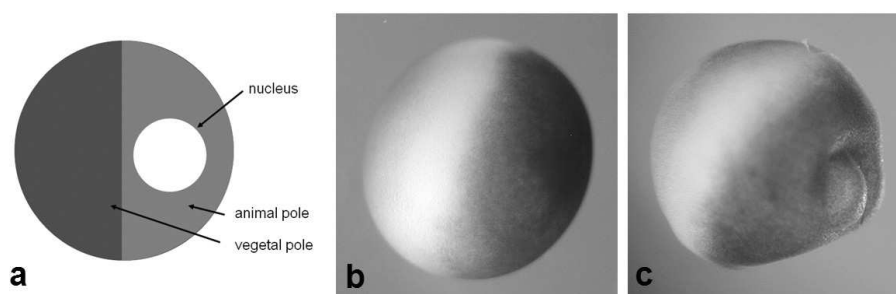


Fig. 7.1: Schematic (a) and photographs of a fresh (b) and fixed(c) oocyte used in these experiments. This figure is reprinted from reference [82].

mately eight days, eight cells from the latter group were reimmersed in Barths medium for three days, with the other eight cells left in fixative. Prior to NMR experiments, the cells were studied under a microscope to check for obvious signs of physical degradation or lysing: those showing these gross effects were removed from the study. Table 7.1 shows the total number of cells used in each measurement. In a separate experiment to determine the effects of fixation on membrane permeability with respect to small molecules, a contrast agent (Gadovist, 5 mM) was added to the medium surrounding fresh cells ($n=2$) and cells that had been fixed for eight days ($n=2$). After 2 hours of immersion in the Gd-solution T_1 relaxation maps were obtained to determine whether the contrast agent had permeated through the outer membrane to the animal and/or vegetal poles. Finally, NMR spectra were acquired from nine different cells (three fresh, three fixed, three reimmersed) in order to determine the effects of chemical fixation on lipid content.

7.3 NMR experiments

Experiments were either carried out using the four-channel probehead described in Section 4 for increased throughput or using a homebuilt 2 mm solenoid coil wound on a glass capillary having an inner diameter of 1.6 mm. The latter coil was immersed in FC-43 for susceptibility matching to improve the spectral linewidth and minimize off-resonance effects for spectroscopy experiments and T_2 estimation, respectively. Spectral linewidths (FWHM) were typically about 150 Hz for samples in the four-channel probehead after shimming on all four coils and about 50 Hz in the susceptibility-matched coil. All experiments were carried out at 16°C. All imaging data were acquired using the three-dimensional spin-echo based sequences as described in Chapter 3. It should be noted that Sehy et al. have shown no evidence for restricted diffusion using inter-gradient diffusion times of between 3.4 and 100 ms [50]. The diffusion coefficient was only determined in one diffusion-sensitizing direction because it has been shown that the fractional anisotropy (FA) is rather small in both the poles and nucleus of *Xenopus* oocytes [50]: Hsu et al. [83] have shown similar results for another commonly studied single cell system, the L7 neuron in *Aplysia Californica*. It should also be noted that the ADC was calculated as a single exponential: Sehy et al. [49] have shown that the intracellular components can be represented as two exponentials, with the fast fraction contributing approximately 90%. The slow component is only significant at very high b-values, which were not explored here.

Parameter fitting was carried out as described in Chapter 3; representative maps are shown in Fig. 7.4.1. Regions of interest (ROIs) were placed in the nucleus, vegetal and animal pole in slices from the 3D data sets. Due to the extremely short T_2 in the vegetal pole no dependable T_2 or ADC data could be fitted from within this region. Statistical analysis used three one-way analyses of variance (ANOVAs); two groups were compared at a time, and F and p-values for the individual pairings were obtained. In accordance with standard practice, a p-value of less than 0.05 was assigned to be statistically significant. The values obtained are displayed in Table 7.1, with full statistical analysis in the changes in the parameters summarized in Tables 7.2 and 7.3. NMR spectra with 16384 complex data points were acquired with a 10 kHz bandwidth, $N_A = 64$ signal averages and were processed with MestReC (Santiago de Compostela, Spain). The methylene peak at 1.17 ppm was chosen as a representative lipid peak, as shown in Fig. 7.4, and a frequency-domain line-fit and signal integration was performed.

7.4 Results and Discussion

Fig. 7.1 (a-c) shows a schematic and photographs of an oocyte, fresh Fig. 7.1(b) and fixed Fig. 7.1(c), used in these experiments. After immersion in formaldehyde the concave shape of the oocyte is always observed. The deformation of the animal pole occurs mainly because the cytoskeletal structure collapses under the influence of the formaldehyde [84]. Subsequently, the intracellular pressure (turgor) is lost, and the animal pole also changes significantly in shape.

Non-fixed samples

The values of T_1 , T_2 and ADC values for the nucleus, vegetal and animal poles are in good agreement with results obtained previously by Sehy et al. at 4.7 T [48], with T_1 values slightly longer and T_2 values slightly shorter at 17.6 T for each compartment, as might well be expected. Also, the spatial variation of relaxation times inside fresh oocytes due to the division into vegetal and animal hemisphere found in [48] was also apparent at 17.6 T: a 25% difference in T_1 was measured in a profile across the oocyte. The physiological basis for the higher values of the T_2 and ADC in the nucleus than in the cytoplasm has been described and investigated in detail in a number of papers for the L7 neuron of *Aplysia Californica* [83, 85, 86, 87] and for *X. Laevis* [48].

7.4.1 Fixed samples

After immersion in fixative solution, a decrease in T_1 ($p < 0.001$) of 30% in both the animal pole and the vegetal pole, and a decrease ($p < 0.001$) of 13% in the nucleus, a decrease ($p < 0.001$) in the T_2 of 85% in the nucleus and 45% ($p < 0.001$) in the animal pole, and a decrease ($p < 0.001$) in the ADC in the animal pole of 25% and 6% ($p = 0.02$) in the nucleus were recorded. Going from non-fixed to fixed cells, the decrease in T_1 for the Barth's medium was very similar to that for the nucleus, in percentage terms. Potential mechanisms for the T_1 reduction involve chemical exchange and viscosity changes [74]. Previous measurements of viscosity changes caused by the concentration of formaldehyde used in this study do not support a change large enough to explain the differences in

	T_1 (s)	T_2 (ms)	ADC ($\cdot 10^{-3}$ mm ² /s)
	Mean \pm SD (sem)	Mean \pm SD (sem)	Mean \pm SD (sem)
<i>Fresh</i>			
	n=5	n=4	n=6
nucleus	2.57 \pm 0.39 (0.03)	113.4 \pm 13.5 (1.62)	1.58 \pm 0.34 (0.03)
animal pole	1.59 \pm 0.34 (0.02)	20.9 \pm 7.4 (0.62)	1.17 \pm 0.61 (0.05)
vegetal pole	1.18 \pm 0.38 (0.02)	15.36 \pm 10.44 (1.07)	-
medium	2.74 \pm 0.16 (0.06)	922.0 \pm 108.0 (8.0)	1.70 \pm 0.08 (0.03)
<i>Fixed</i>			
	n=6	n=6	n=7
nucleus	2.25 \pm 0.32 (0.03)	19.3 \pm (0.29)	1.27 \pm 0.45 (0.04)
animal pole	1.14 \pm 0.29 (0.02)	10.9 \pm 4.0 (0.4)	0.88 \pm 0.58 (0.06)
vegetal pole	0.83 \pm 0.41 (0.03)	-	-
medium	2.35 \pm 0.05 (0.02)	44.46 \pm 2.11 (1.06)	1.64 \pm 0.05 (0.03)
<i>Reimmersed</i>			
	n=6	n=8	n=7
nucleus	2.35 \pm 0.10 (0.04)	128.9 \pm 26.0 (2.44)	1.67 \pm 0.26 (0.02)
animal pole	1.15 \pm 0.11 (0.04)	12.3 \pm 7.8 (0.6)	1.20 \pm 0.44 (0.03)
vegetal pole	1.03 \pm 0.15 (0.06)	12.0 \pm 9.0 (1.0)	-
medium	2.71 \pm 0.13 (0.06)	978.0 \pm 117.0 (12.8)	1.80 \pm 0.08 (0.04)

Tab. 7.1: Relaxation times and ADCs of fresh, fixed and reimmersed oocytes

<i>Nucleus</i>		
T_1	-13%	p < 0.001
T_2	-83%	p < 0.001
ADC	-6%	p = 0.019
<i>Animal pole</i>		
T_1	-28%	p < 0.001
T_2	-48%	p < 0.001
ADC	-25%	p < 0.001
<i>Vegetal pole</i>		
T_1	-30%	p < 0.001

Tab. 7.2: Changes in NMR parameters from fresh to fixed cells

<i>Nucleus</i>		
T_1	-9%	$p < 0.001$
T_2	+13%	$p < 0.001$
ADC	+6%	$p = 0.02$
<i>Animal pole</i>		
T_1	-28%	$p < 0.001$
T_2	-41%	$p < 0.001$
ADC	no change	$p = 0.6$
<i>Vegetal pole</i>		
T_1	-13%	$p < 0.001$
T_2	-22%	$p = 0.025$

Tab. 7.3: Changes in NMR parameters from fresh to post-fixation reimmersed cells

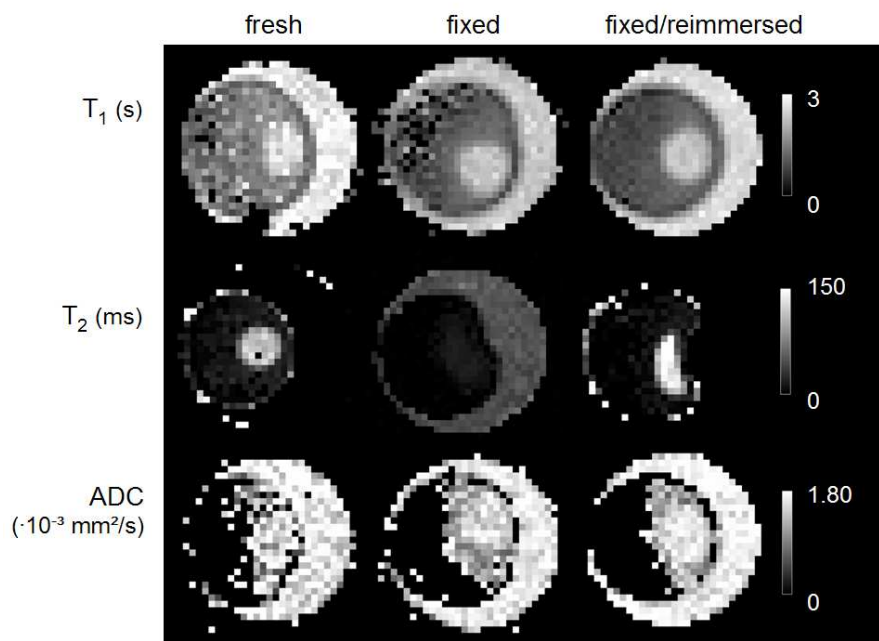


Fig. 7.2: Parameter maps for unfixed, fixed and reimmersed oocytes. Data acquisition parameters are contained in the main text. Note that, for clarity, the T_2 maps do not show values for the medium for either the fresh or reimmersed cells. This figure is reprinted from reference [82].

T_1 values [88]. These facts suggest that the dominant factor in reducing T_1 values is chemical exchange. There is a larger reduction in T_1 , approximately twice as much, in the animal and vegetal poles compared to the nucleus, suggesting that substantial cross-linking occurs within these latter regions. The T_2 value is extremely sensitive to chemical exchange effects, and there is similar behavior in the nucleus and Barth's medium in terms of percentage reduction. The T_2 decreases in the nucleus and animal pole are statistically significant ($p < 0.001$), but the change in the animal pole is difficult to quantify, given the very short values even before fixation. The measured ADC is not sensitive to chemical exchange if a sufficiently short T_E value is used: the fact that the ADC in the medium is very similar for Barth's medium without and with formaldehyde suggests that this is true for the data acquisition parameters used in this study. Since the ADC also depends upon viscosity, the similar values suggest that any viscosity differences between buffer and buffer+fixative are relatively small. Substantial changes in the ADC upon fixation can therefore be linked directly to structural changes, i.e., protein crosslinking. In the nucleus there is a statistically significant ($p = 0.02$) very small decrease in the ADC, suggesting no major structural effects of fixation. In the animal pole there is a decrease in the ADC, ($p < 0.001$): the formation of cross-links would be expected to decrease the water ADC, which is indeed the case here.

7.4.2 Fixed samples reimmersed in buffer

Table 7.3 summarizes the changes in NMR parameters comparing fresh cells with those that have been fixed and reimmersed in buffer. The nucleus shows a small decrease in T_1 , and increase in T_2 and ADC values. The T_2 values strongly suggest that there is no residual formaldehyde in the nucleus, and that the physical environment of the water inside the nucleus has been made slightly freer by the fixation and re-immersion process. In contrast, the T_1 and T_2 values in the animal and vegetal poles show large decreases in the reimmersed cells compared to the fresh cells, with no change in the ADC of the animal pole. These data suggest that there are unreacted aldehyde groups left in these cellular regions, which can still undergo chemical exchange. The presence of unreacted groups has also been found in previous studies by Helander using ^{14}C -labeled formaldehyde-fixed specimens of rabbit liver [89], although no cellular information about the distribution of the formaldehyde was gathered. This latter study determined that the isotope binding reached a plateau after 24 hours, and that after rinsing with water for almost four weeks the level had decreased to between 10-20% of the maximum level. Since the T_2 values are more sensitive to chemical exchange than the T_1 values, the presence of aldehyde groups would be expected to result in the T_1 values after reimmersion being closer to the fresh cells than the T_2 values: this is born out by the data in Tables 7.2 and 7.3.

7.4.3 Gadolinium experiments

Representative T_1 maps from the Gd-experiments are shown in Fig. 7.3. In all six cells studies, the results were the same. In the fresh cells the T_1 values for nucleus, animal pole and vegetal pole, Fig. 7.3(a), are not affected by immersion in the Gd-solution, showing that the membrane is impermeable to small molecules. In the fixed and reimmersed cells, Figs. 7.3(b) and (c) the T_1 values are reduced by over a factor-of-twenty compared to the

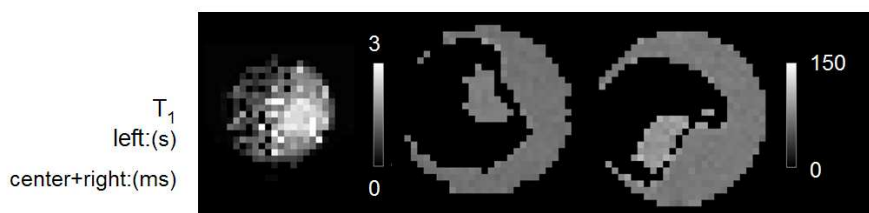


Fig. 7.3: T_1 maps with 5 mM Gadovist added to the medium surrounding the oocyte. (left) fresh oocyte in Barth's medium. (center) Fixed oocyte in Barth's medium plus formaldehyde. (right) Fixed oocyte after reimmersion in Barth's medium. This figure is reprinted from reference [82].

fresh cells: statistical analysis shows that this reduction has a p value much less than 0.01. One can therefore surmise that the outer cellular membrane and also the double membrane between cytoplasm and nucleus have been structurally and functionally altered.

7.4.4 Spectroscopic experiments

Fig. 7.4 shows three spectra, one each from a fresh, fixed and reimmersed cell, displaying very similar lipid levels for all conditions of the cells. A statistical analysis of the data from all nine cells showed that there was no significant change in the lipid concentration over the three conditions which suggests that lipids are most likely trapped during the formaldehyde cross-linking process, but that no chemical reaction with lipid is taking place within the period of fixation employed in our study.

7.5 Conclusion

Using a well-characterized single cell system allows a detailed study of the intracellular effects on NMR relaxation times and diffusion coefficients of chemical fixation and subsequent reimmersion. Although NMR data cannot detect all of the physical processes involved, it does provide information on reversible and non-reversible structural changes. Based on the results presented here, and elsewhere by other authors, it is clear that some care must be taken in interpreting relaxation and diffusion data in fixed tissues, even after reimmersion in buffer.

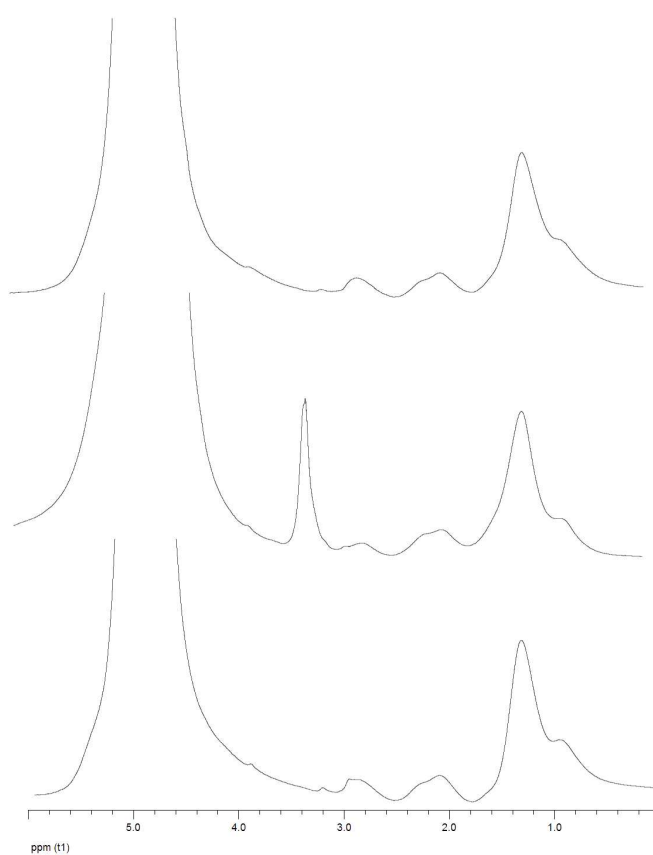


Fig. 7.4: Spectra obtained from (top) fresh, (center) fixed, and (bottom) fixed and then reimmersed. The peak at 3.2 ppm originates from the formaldehyde polymers. This figure is reprinted from reference [82].

8. MORPHOLOGICAL STUDIES OF *X. LAEVIS* EMBRYOS

As mentioned before, *X. laevis* is a widespread animal model in developmental biology due to its robustness, short generation time and easily accessible embryos. Visible light microscopy techniques such as confocal microscopy or histological sectioning are commonly employed when studying this type of organism. Those techniques, however, are hampered by the opacity of the sample mostly due to yolk inclusions. This composition does not affect the effectivity of NMR microscopy on the other hand, making it a tool well suitable for noninvasive three-dimensional analysis of embryos of this species. In a previous study by Papan and coworkers, the gastrulation process has been visualized *in vivo* over a period of 24 hours at a temporal resolution of approx one hour [90].

In this study, NMR microscopy was used for three-dimensional visualization of *X. laevis* embryos at different developmental stages. In addition, the influence of chromosomal protein overexpression as well as depletion on the development process was assessed. High mobility group N (HMGN) and Histone H1A protein knock-down and HMGN overexpressed specimen were examined by NMR microscopy and compared to wild-type samples. Chromosomal proteins such as histones are associated with DNA and perform important gene regulation. DNA is spatially compressed by wrapping around histone protein, the combination is called chromatin. HMGN and Histone H1A are proteins that act as a stabilizer for chromatin. H1A is the most abundant subtype of H1 histone.

The influence of HMGN and H1A protein levels upon the development of *X. laevis* were studied extensively by Dr. Ulrich Körner [91] (HMGN) and Tina Stange [92] (H1A). NMR microscopy of individual embryos at suitable stages was performed in addition to conventional histological sectioning and confocal microscopy techniques.

8.1 Embryo preparation

In vitro fertilization and culture of embryos as well as manipulation of HMGN and H1 protein levels were performed by Dr. Ulrich Körner, Dr. Robert Hock and Tina Stange (Dept. of Cell and Experimental Biology, University of Würzburg) as described previously [93, 94]. For the time lapse study, wild type embryos were grown to the according Nieuwkoop and Faber (NF) stages 2, 6, 6.5, 11, Gastrula, Neurula, 22 and 29. For the HMGN study, manipulated and wild type embryos were grown until the wild type controls reached NF stage 35, upon which they were fixed for 2h at room temperature in MEMFA and stored in 100% methanol at -20°C. For the H1 study, the procedure was carried out similarly to NF stage 35. Since formaldehyde-based fixation is known to lead to very short tissue T₂ values (see Chapter 7), prior to MRI experiments, embryos were rehydrated in a descending methanol series and placed in phosphate-buffered saline (PBS). Hereafter, embryos were immersed in FC-43 to reduce magnetic susceptibility effects, avoid signal from the surrounding medium and thus to maximize the dynamic range of the signal from

the embryo. For the H1 study, 2 mM Gadolinium (Magnevist, Schering) was added to the PBS solution for T_1 reduction and increased SNR efficiency in the spin echo experiments.

8.2 *NMR imaging*

8.2.1 *Time lapse study*

Embryos were placed in 2 mm o.d. glass capillaries. Up to four individual samples were inserted into the four available 2 mm solenoid coils of the multicoil probehead described in Chapter 4. Imaging was thus performed simultaneously on multiple samples. A 3D spin echo sequence was used with an echo time $T_E = 4.76$ ms, a repetition time $T_R = 200$ ms and $N_A = 192$ averages. Data acquisition parameters were empirically optimized to give best contrast. The acquisition matrix consisted of $512 \times 128 \times 128$ complex points, the FOV was $3.84 \times 1.92 \times 1.92$ mm³ resulting in an isotropic spatial resolution of $(15 \mu\text{m})^3$. Total data acquisition time was 11 h.

8.2.2 *HMGN study*

Each embryo was placed in a 2.5 mm o.d. glass capillary and inserted into a 2.5 mm i.d. four-turn Bruker solenoid RF coil. Three-dimensional data sets of each embryo were acquired using a 3D spin echo sequence. Data acquisition parameters were $T_R = 600$ ms, an echo time $T_E = 5.4$ ms, number of averages 16 (wild type), 18 (HMGN overexpressed) and 10 (knock down), spatial resolution $33 \times 14 \times 14 \mu\text{m}^3$ (wild type), $14 \times 14 \times 14 \mu\text{m}^3$ (HMGN overexpressed and knock down). Total data acquisition times were ≈ 14 h for each sample: the FOV for the wild type in the long-direction was twice that in the other two embryos due to its physically larger size. The NMR data sets were zero-filled to $256 \times 128 \times 128$ before inverse Fourier transformation. Images were analyzed using the software package Amira 3.0 by Dr. Robert Hock. 3D digital reconstruction of the embryos was performed using the Voltex tool and the segmentation editor tool was used to simultaneously slice the embryos in all three axial planes in parallel windows.

8.2.3 *H1A study*

An NF stage 35 H1 knock-down embryo was prepared in the same way as the embryos in the time-lapse study. Imaging parameters were chosen similarly. For comparison with a wild type NF stage 35 embryo, the respective wild type data set obtained from the HMGN study was chosen. Segmentation of the 3D data set was performed using the software package Amira 3.0 by Tina Stange.

8.3 *Results and Discussion*

8.3.1 *Time lapse study*

Results from imaging experiments are shown in Figs. 8.1 and 8.2, along with light microscopic images of the according stages. In the obtained image data, the morphology of the respective stages is well depicted. The maximum intensity projections (MIPs) reflect the visual appearance of the complete embryos. Light microscopy, however, is only able

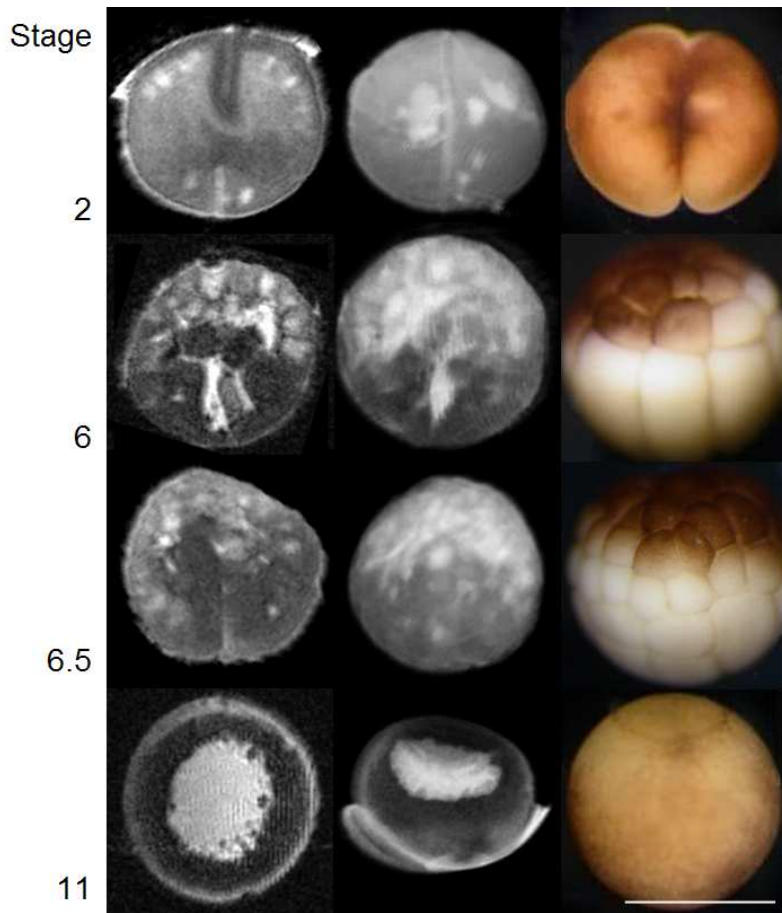


Fig. 8.1: Time lapse study of NF stages 2, 6, 6.5 and 11: (left) individual slice from dataset, (center) 3D-Maximum Intensity Projections (MIP), (right) light microscopic image [95]; artifacts in stage 2 slice and stage 11 MIP is caused by residual liquid on the embryo surface. Note that embryo orientation within images is not always identical; scale bar 1 mm

to represent the surface structure of the early stages when the embryo has a spherical shape. This is caused by the large yolk inclusions which are opaque to light. On the other hand, yolk appears dark in NMR images. Intraembryonal contrast is very pronounced, in analogy to the results obtained from *X. laevis* oocytes, most likely due to the large differences in T_2 times. In the early stages (stages 6 and 6.5) when the fertilized ovum has only divided several times, individual cells can still be distinguished due to the high intracellular contrast. Hereafter, the decrease in cell size due to constant cell divisions together with the limited spatial resolution impedes the observation of single embryonic cells. The good intraembryonal contrast is preserved in the course of embryonal development. Macroscopic changes can be traced, such as the formation of somites, a mesoderm structure that will become skeletal muscle in the developmental process. Somites are pointed out in Fig. 8.2, stages 22 and 29.



Fig. 8.2: Time lapse study of NF stages gastrula, neurula, 22 and 29: (left) individual slice from dataset, (center) 3D-Maximum Intensity Projections (MIP), (right) light microscopic image [95]; arrows indicate somites; artifacts in gastrula and neurula slices and MIPs is caused by residual liquid on the embryo surface. Note that embryo orientation within images is not always identical; scale bar 1 mm

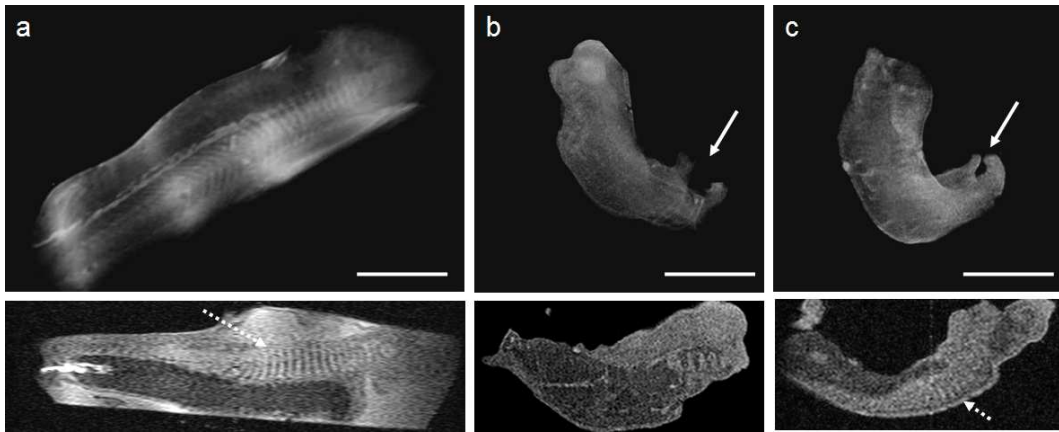


Fig. 8.3: (top) 3D-Maximum Intensity Projections, (bottom) individual slices from datasets, (a) wild type, (b) HMGN knock-down and (c) HMGN overexpressed embryos; the solid arrows indicate imperfect blastopore closure, the dotted arrows indicate somite positions; scale bar 1 mm

8.3.2 HMGN study

Results from this study are shown in Fig. 8.3. For each embryo, a MIP image has been displayed along with one exemplary slice. Comparison between wild type and HMGN modified embryos shows that deviation of HMGN protein levels causes a distorted and shortened body axis. The blastopore, an embryonic structure initially opened during gastrulation, is closed in wild type embryos forming the primitive gut. HMGN modified embryos showed imperfect blastopore closure, as shown in Fig. 8.3 (b) and (c). Furthermore, the data revealed that myotome differentiation was impaired following HMGN injection. Compared to the wild type data set, horizontal and sagittal sections of HMGN-injected embryos showed that the myotome organization was more loose. Moreover, malformed or missing structures in HMGN manipulated embryos were identified, i.e. reduced development of brain, eyes, and spinal cord, the reduced development and organization of the somites and the absence of a notochord and a spinal cord in the posterior region of the HMGN-injected or HMGN knock-down tadpoles. Differences in anterior malformations caused after increasing or reducing HMGN protein levels are also evident.

8.3.3 H1A study

Results from NMR microscopy are presented in Fig. 8.4. Identification of several organs allowed 3D volumetric segmentation. Good agreement was found with conventional histology: all structures present in the wild type embryo have been identified in the knock down embryo, revealing no major deviations in position or size. The knock-down embryo appears morphologically rather equal to the wild-type controls. The body axis is intact, somite formation is normal and the head region is similar in size. The functions of the H1A histone can be compensated almost fully by other histone and non-histone proteins as shown in the work by T. Stange [92]; this is confirmed by NMR microscopy of the knock-down embryo.



Fig. 8.4: Individual slices and 3D maximum intensity projections from NF stage 35 wild type (a,c) and H1 knock-down (b,d) embryos; the dotted arrows indicate somite positions; Identification of following organs allowed segmentation: nerve system (yellow), notochord (orange), eyes (blue), pharynx (green) and heart (red); scale bar 1 mm

8.4 Conclusion

The data presented here show that high field magnetic resonance microscopy, at a spatial resolution of $15 \times 15 \times 15 \mu\text{m}^3$, is very useful in assessing morphological changes in embryonic development of *X. laevis*. In comparison with conventional histological sectioning, layers obtained from three-dimensional NMR imaging are still inferior in terms of resolution. On the other hand, regarding the long preparation times necessary for histological sectioning, the methodology applied in this study allows significantly faster preparation and data acquisition. The combination with time-efficient parallelization of four individual experiments makes this technique ideally suited for screening experiments where highest image resolution is not the main prerequisite.

9. SPECIFIC LABELING USING IRON OXIDE

In the previous sections, applications have been presented that employ NMR microscopy at high spatial resolution in order to display the morphology of biological systems. In certain applications, however, it is desirable to obtain information from structures far below the spatial resolution, typically large molecules such as proteins. For this purpose, a contrast agent is linked to a "seeker" molecule that specifically detects and links to the desired target. This general methodology is independent of the respective imaging technique. The initial motivation is the early detection and potential treatment of diseases such as malignant tumors long time before a morphological manifestation impedes proper treatment. This methodology called molecular imaging is broadly defined as the "*in vivo* characterization and measurement of biologic processes at the cellular and molecular level" [96].

In biology, the specific detection and labeling of target structures has long been a standard method. Immunohistochemical methods make use of antibodies that are coupled to fluorescent dyes. A distribution of multiple target molecules thus can be obtained using different dyes, but quantification is complicated by the nonlinear performance of light intensity vs. number of fluorescent molecules. Even though advances in light microscopy such as confocal microscopes have been established, a true three-dimensional representation of specimens is not achievable due to the opaque nature of most samples. This is also true for optical projection tomography (OPT), which is essentially an optical analogue to computer tomography (CT) [97]. Despite the already mentioned inferior spatial resolution that is achievable with NMR microscopy, its ruggedness against opaque samples is advantageous when studying samples such as *X. laevis* embryos. Those contain a considerable amount of yolk that is responsible for significant light scattering. Compared to light microscopy, however, specific labeling techniques in NMR are still scarce, although efforts have been made to adapt common paramagnetic and superparamagnetic NMR contrast agents to specific linker molecules. Louie and coworkers [98] have presented a so-called smart contrast agent denoted as Egad-Me, which is composed of a Gadolinium-containing molecule with an obstructed coordination site. The obstruction can only be cleaved by the enzyme β -galactosidase. Cleavage leads to an increased relaxivity and thus, abundance of the target molecule can be inferred from image contrast based on T_1 reduction.

Besides paramagnetic contrast agents which are mostly Gadolinium based, superparamagnetic and ferromagnetic contrast agents are highly significant. Those agents are composed of small iron oxide particles on the nm to μm scale. Due to their ferromagnetic nature, those particles will be magnetized in the static magnetic field and produce a field distortion that is much larger than their physical dimension, making them ideal specific markers. Particles that are smaller in size than a single Weiss domain essentially show paramagnetic behaviour and are denoted as superparamagnetic. Corresponding particles down to sizes of 10 nm are known as small Superparamagnetic Iron Oxide (SPIO) while

	Resovist	VSOP C200	MACS IgG
core diameter (nm)	4 ± 1	5	≈ 10
total diameter (nm)	58 ± 1	≈ 11	48 ± 14^1
coating	carbodextran	monomeric citrate	carbodextran
core composition	Fe_2O_3	$\text{Fe}_2\text{O}_3/\text{Fe}_3\text{O}_4$	$\text{Fe}_2\text{O}_3/\text{Fe}_3\text{O}_4$
reference	[100]	[101]	[102]

Tab. 9.1: Parameters of iron oxide contrast agents

sizes below 10nm are known as Ultrasmall Superparamagnetic Iron Oxide (USPIO).

In this study, the NMR properties of USPIO particles with core diameters of a few nm and various biocompatible coatings has been examined. The applicability of USPIO-labelled antibodies was evaluated using wild type *X. laevis* embryos as a specific NMR contrast agent [99] for indirect immunolabeling by studying intraembryonal relaxation times.

9.1 Quantification of iron concentration

The iron oxide labeled antibodies used in this study (MACS, Miltenyi Biotech, Germany) consist of a dextran-coated iron oxide particle with a total diameter of 50 nm coupled to goat anti-mouse IgG antibodies. The manufacturing company does not disclose all relevant parameters regarding this product, such as iron concentration, particles per antibody, exact size and magnetization of the core. It is only known that the iron oxide core is significantly smaller than the overall particle diameter and that it consists of maghemite (Fe_2O_3) and magnetite (Fe_3O_4).

In order to determine the iron concentration which is a classified parameter, relaxation times of different MACS concentrations were measured spectroscopically and the susceptibility of one MACS concentration was measured with the method described in Section 5.3. In contrast to substances used in susceptibility measurements previously carried out and described in Chapter 5, the iron oxide particles are superparamagnetic. The dependence of the magnetization on the magnetic field is analogous to a ferromagnet without the effect of hysteresis, meaning that the remanence is zero. The superparamagnetic behaviour is caused by the size of the particles, which is smaller than one magnetic domain. Unlike a paramagnet where the magnetization is induced and where its magnitude is proportional to the external field, the magnetization of superparamagnetic particles saturates above a certain field strength which is typically on the order of 1 T. In this case, χB_0 has to be replaced by the saturated magnetization $\mu_0 M$.

The iron quantification procedure was also carried out for Resovist SH U555A (Schering AG, Berlin, Germany) and VSOP particles (Ferropharm GmbH, Teltow, Germany). Experiments were motivated by a need for validation as well as a need for experimental data at 17.6 T. The iron concentrations of these iron oxide based contrast agents are known and the core sizes are comparable to the size of the MACS core.

¹ In [102], the particle diameter has been determined with electron microscopy and dynamic light scattering. Reported diameters were 30 ± 20 nm (e.m.) and 65 ± 20 nm (DLS). Calculation of a weighted average value gives the mean value and error reported above.

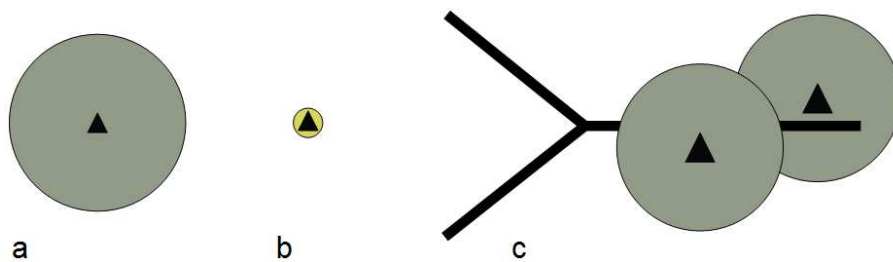


Fig. 9.1: Schematics of a (a) Resovist particle, (b) VSOP and (c) antibody-coupled MACS; the actual amount of MACS particles coupled to an antibody is unknown, a number of two has been chosen arbitrarily

9.1.1 Relaxivity

The relaxivities r_1 and r_2 of Resovist, VSOP and MACS contrast agents have been determined by measuring T_1 and T_2 relaxation times at different concentrations. The relaxation rates $1/T_{1,2}$ change according to:

$$\frac{1}{T'_{1,2}} = \frac{1}{T_{1,2}} + c \cdot r_{1,2} \quad (9.1)$$

Solutions of the various contrast agents were prepared at different concentrations and approximately 500 μl were poured into 5 mm NMR tubes respectively. The relaxation time experiments were carried out spectroscopically using a Bruker 20 mm birdcage coil. Only one NMR sample was examined at a time. The tube was centered inside the 20 mm coil by a spacer disc with 20 mm o.d. and 5 mm i.d. As the experiment was not SNR-limited, a 20 mm coil was favored over a 5 mm birdcage coil because of increased B_1 homogeneity. T_1 was measured using an inversion recovery sequence with 16 different delay times. T_2 was measured with a CPMG sequence for 16 different total echo times. The delay time between the 180° pulses was 1 ms. The number of refocusing pulses was increased from 2 to a total of 32 (samples with short T_2) up to 512 (samples with long T_2). The data was fitted with XWIN-NMR (Bruker Biospin GmbH).

The relaxation time T_2^* was measured by acquiring an FID and obtaining the *FWHM* of the spectral line hereafter which is assumed to be Lorentzian. Due to the mathematical relation

$$T_2^* = \frac{1}{\pi \cdot FWHM}, \quad (9.2)$$

T_2^* can be calculated from the *FWHM* value.

Resovist

The experiments were carried out for five different iron concentrations ($c = (0.25, 0.5, 1.0, 3.0, 5.0)$ mM). A linear regression algorithm was used to obtain the relaxivities according to Eq. (9.1):

$$\begin{aligned} r_1 &= 0.46 \pm 0.01 \text{ mM}^{-1}\text{s}^{-1} \\ r_2 &= 205.4 \pm 6.1 \text{ mM}^{-1}\text{s}^{-1} \\ r_2^* &= 232.6 \pm 7.9 \text{ mM}^{-1}\text{s}^{-1}. \end{aligned}$$

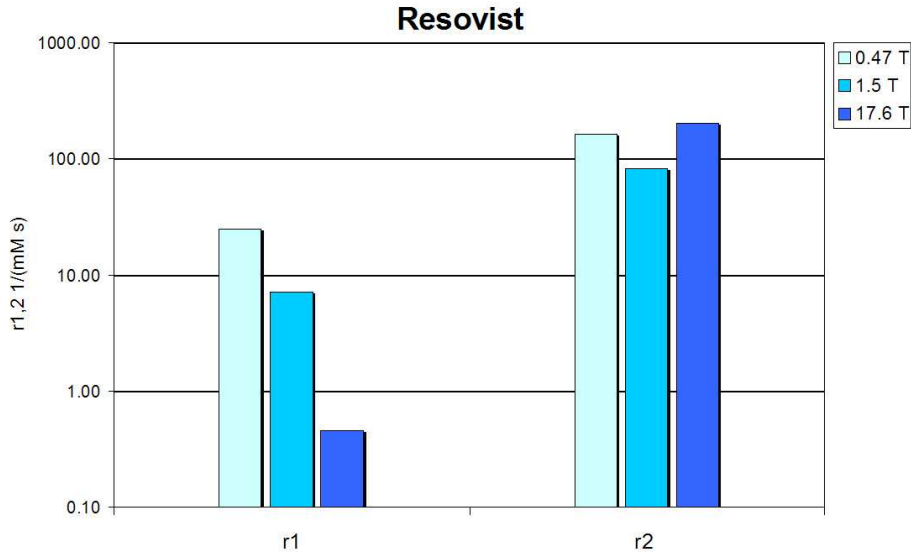


Fig. 9.2: Relaxivities r_1 and r_2 of Resovist at different field strengths

The measured relaxivities at $B_0 = 17.6$ T have been compared to published values at 0.47 T [100]. The data is shown in Fig. 9.2. The relaxivity r_1 is reduced by a factor of almost 54, while r_2 is slightly increased by a factor of 1.25. The ratio r_2/r_1 changes from 6.6 at 0.47 T to 447 at 17.6 T.

VSOP

The relaxivities of five VSOP solutions with different iron concentrations ($c = (0.25, 0.5, 1.0, 3.0, 5.0, 10.0)$ mM) have been measured. The relaxivities were obtained in the same way as described above:

$$\begin{aligned} r_1 &= 0.93 \pm 0.03 \text{ mM}^{-1}\text{s}^{-1} \\ r_2 &= 71.5 \pm 1.05 \text{ mM}^{-1}\text{s}^{-1} \\ r_2^* &= 74.8 \pm 2.5 \text{ mM}^{-1}\text{s}^{-1}. \end{aligned}$$

Those values have been compared to published values at three different field strengths. It is worth noting that the values at 0.47 T and 1.5 T were obtained using VSOP C63 particles. It has not been specified how VSOP C63 are different from VSOP C200 particles. A comparison of the relaxivity values from 0.47 T to 17.6 T shows that r_1 has decreased by a factor of 77 and r_2 has increased by a factor of 1.83. The ratio r_2/r_1 increases from 1.3 at 0.47 T to 77 at 17.6 T.

MACS

The relaxivities of four different MACS solutions with varying iron concentrations have been determined ($c = 0, 0.083, 0.200, 0.500$). The concentration is given without units because the actual iron concentration is not specified. A concentration of $c = 1$ corresponds to the initial concentration that the substance was provided. Due to the limited amount

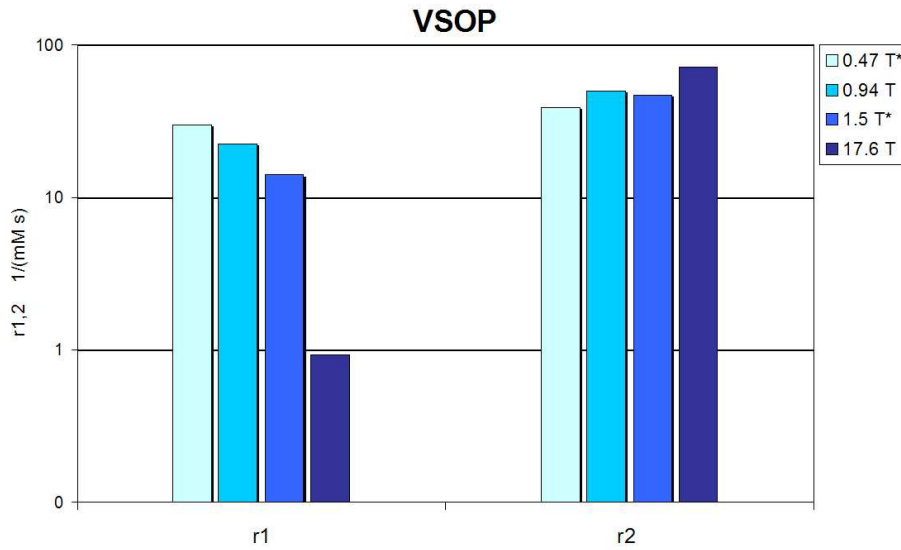


Fig. 9.3: Relaxivities r_1 and r_2 of VSOP at different field strengths: values at 0.94 T obtained from VSOP C200 datasheet [101], *values at 0.47 T and 1.5 T have been obtained for VSOP C63 [103]

of MACS solution, it was not possible to obtain data from additional solutions of different concentrations. The following unitless relaxivities have been obtained:

$$\begin{aligned} r_1 &= 0.86 \pm 0.03 \text{ s}^{-1} \\ r_2 &= 1184 \pm 179 \text{ s}^{-1} \\ r_2^* &= 1242 \pm 87 \text{ s}^{-1}. \end{aligned}$$

Substituting the unitless iron concentration $c = 1$ with the iron concentration determined for MACS by mass spectrometry $c_{Fe,1:1} = 153 \text{ mM}$ (see Section 9.1.3), the molar relaxivities can be calculated:

$$\begin{aligned} r_1 &= (5.62 \pm 0.20) \cdot 10^{-3} \text{ mM}^{-1} \text{ s}^{-1} \\ r_2 &= 7.74 \pm 1.17 \text{ mM}^{-1} \text{ s}^{-1} \\ r_2^* &= 8.12 \pm 0.57 \text{ mM}^{-1} \text{ s}^{-1}. \end{aligned}$$

9.1.2 Iron quantification

Theory

A dilution of iron oxide particles in water is treated as a two-compartment model: the iron oxide particles occupy the fraction η of the total volume, the difference $1 - \eta$ being occupied by water. The magnetization of the particles is $\mu_0 M_p$, and the magnetization of the water is determined by its susceptibility:

$$\mu_0 M_w = \chi_w B_0 \quad (9.3)$$

The resulting sample magnetization M_s of a mixture of particles and water is given by:

$$\mu_0 M_s = \eta \mu_0 M_p + (1 - \eta) \chi_w B_0. \quad (9.4)$$

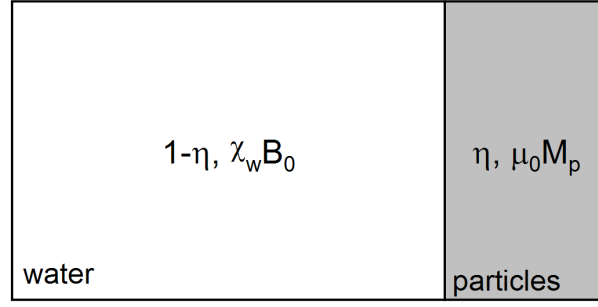


Fig. 9.4: Two-compartment model for the combined susceptibility of particles in solution; η is the particle volume concentration

Rearranging the equation, it can be resolved for the particle magnetization:

$$\mu_0 M_p = \frac{\mu_0 M_s}{\eta} - \frac{\eta - 1}{\eta} \chi_w B_0 \quad (9.5)$$

The above equation contains two unknowns: the volume concentration η and the magnetization of the particle-water mixture $\mu_0 M_s$. The particle concentration can be obtained using the measurement of the transverse relaxation rate $R_2^* = 1/T_2^*$ and following the expression for the transverse relaxation rate R_2^* derivation by Ziener and coauthors [104]; the theory is based on the analysis of the correlation time τ describing the motion of spins around the iron oxide particle and the mean equatorial frequency on the particle surface $\delta\omega$:

$$\tau = \frac{4 R_p^2}{9 D}; \quad \delta\omega = \frac{\gamma}{3} \mu_0 \Delta M \quad (9.6)$$

where R_p is the particle radius, D the self-diffusion coefficient and $\Delta M = M_p - M_w$ is the difference between the magnetization of the particle M_p and the surrounding water M_w .

Two different regimes are usually addressed, depending on spin diffusion and particle size: the case where $\tau\delta\omega \gg 1$ is characterized by slow field fluctuations compared to the field strength and is referred to as the static dephasing regime. The opposite limit is called motional narrowing regime. It is described mathematically by $\tau\delta\omega \ll 1$ and displays the case where field fluctuations are fast in relation to the field strength. For both limiting cases the relaxation process is well understood. Estimations showed that for iron oxide particles on the order of tens of microns, such as MACS, at 17.6 T, $\tau\delta\omega \approx 1$. Neither limit can be applied and a general approach derived is necessary [104]. The general expression for R_2^* is given by

$$R_2^* = \frac{1}{\tau} \text{Re} \left[\frac{1 - \eta}{G(\eta\tau\delta\omega) - \eta G(\tau\delta\omega)} - 1 \right] \quad (9.7)$$

with the function

$$G(x) = \frac{2}{3} (1 - 2ix) \sqrt{\frac{1}{3} \left(1 - \frac{i}{x}\right)} \text{Arccoth} \sqrt{\frac{1}{3} \left(1 - \frac{i}{x}\right)} + \frac{1}{3}. \quad (9.8)$$

Again, there are two unknowns, η and $\delta\omega$. With Equations (9.3) and (9.5),

$$\begin{aligned}
\mu_0 \Delta M &= \mu_0 M_p - \mu_0 M_w = \mu_0 M_p - \chi_w B_0 \\
&= \frac{\mu_0 M_s}{\eta} + \frac{\eta - 1}{\eta} \chi_w B_0 - \chi_w B_0 \\
&= \frac{\mu_0 M_s - \chi_w B_0}{\eta}.
\end{aligned} \tag{9.9}$$

The frequency shift on the particle surface $\delta\omega$ becomes a function of η and the sample magnetization M_s :

$$\delta\omega = \frac{\gamma\mu_0 \Delta M}{3} = \frac{\gamma(\mu_0 M_s - \chi_w B_0)}{3\eta}. \tag{9.10}$$

Introducing the above relation into the general expression for the relaxation rate given in Eq. (9.7), it is possible to obtain a value for the particle volume concentration η by implicitly solving the resulting equation.

Resovist

The magnetization of a diluted solution (1:99) of 0.5 M Resovist resulting in a nominal iron concentration of $c_{Fe} = 5$ mM was measured using the method described in Chapter 5. With $\eta\delta\omega = 2728.6$ Hz, $R_2^* = 1493$ s⁻¹ and a radius of $R_p = 29$ nm which corresponds to the published hydrodynamic radius, a volume particle concentration of $\eta = 5.68 \cdot 10^{-4}$ is obtained. Assuming that the core is composed of maghemite, the resulting iron concentration is $c_{Fe} \approx 35$ mM, seven times higher than the actual concentration.

If the knowledge about the iron concentration is used to compute the respective particle size, the radius is approximately $R_p = 11$ nm, which is significantly smaller than the hydrodynamic radius but still larger than the core radius.

VSOP

A solution of VSOP C200 with a concentration $c_{Fe} = 5$ mM was obtained by diluting the native solution with a ratio of 1:99. In analogy to the measurement carried out for Resovist, the magnetization of the solution was determined, resulting in a value $\eta\delta\omega = 3406.3$ Hz. With $R_2^* = 446$ s⁻¹ and assuming a radius $R_p = 2.5$ nm, the volume concentration is $\eta = 1.14 \cdot 10^{-4}$, leading to an iron concentration $c_{Fe} = 1.8$ mM. The value is about 2.8 times smaller than the actual concentration. On the other hand, using the known concentration to calculate the corresponding radius, a value of $R_p = 4.1$ nm is obtained, which is consistent with the published value range for the hydrodynamic diameter of 8 nm to 11 nm.

MACS

With $R_p = 25$ nm, $D = 2 \cdot 10^{-9}$ m²/s, $\chi_w = -9.04 \cdot 10^{-6}$ and the measured values for 1:3 diluted MACS ($\eta\delta\omega = \gamma\mu_0 M_s/3 = 721.9$ Hz and $R_2^* = 341$ s⁻¹):

$$\eta = 1.39 \cdot 10^{-4}. \tag{9.11}$$

Sample no.	c_{iron} (ppb)	c_{iron} (μM)	SD (%)	nominal c_{iron} (μM)
1 (Resovist)	577.6	10.3	1.7	10.0
2 (VSOP)	4.2	0.08	17.0	10.0
3 (MACS)	854.9	15.3	1.7	unknown
4 (water)	2.2	0.04	27.9	-

Tab. 9.2: Results from iron quantification using MS

The concentration of iron is determined by

$$c_{Fe} = \eta \frac{f\rho}{M} \quad (9.12)$$

where ρ is the density, M the molar mass and f the number of iron atoms per molecule. For maghemite (Fe_2O_3), $f\rho/M = 2 \cdot 4900/160 \text{ mol/l} = 61.25 \text{ mol/l}$ and for magnetite (Fe_3O_4), $f\rho/M = 3 \cdot 5200/232 \text{ mol/l} = 67.2 \text{ mol/l}$. The iron concentration of undissolved MACS antibodies becomes

$$c_{Fe} = 36.0 \text{ mmol/l} \quad (9.13)$$

if a ratio of 1:1 of maghemite vs magnetite is assumed.

9.1.3 Verification using mass spectrometry

Individual samples of Resovist (sample 1), VSOP (sample 2) and MACS (sample 3) solutions were analyzed using mass spectrometry (MS) in order to obtain additional information on iron concentration. The experiment was carried out by Dr. Andrea Heymer (Division of Tissue Engineering, Orthopaedic Institute, University of Würzburg). Resovist and VSOP have known iron concentrations and were used to confirm the method. According to the standard protocol, each sample had a total volume of 5 ml, whereof 77 μl were 65% HNO_3 . Due to the high sensitivity of the MS, the iron concentration needs to be quite low, on the order of μM . In a first step, Resovist, VSOP and MACS were each diluted at a ratio of 1:1000 with Millipore water. In the next step, Resovist and VSOP were diluted another 1:49, resulting in an iron concentration of 10 μM . MACS were diluted at a ratio of 1:9 in the second step. A fourth sample with no iron was added to determine the iron level bias from the water.

Experimental results from MS are given in parts per billion (ppb) of the element of interest, in this case it was ^{56}Fe . Hereby, 1 ppb is equivalent to 1 $\mu\text{g/l}$ iron. The results are given in Table 9.2.

The iron concentration of the Resovist sample as determined by MS is in good agreement with the nominal concentration, whereas the value obtained from the VSOP sample is only a factor of two higher than the iron concentration found in Millipore water. The value obtained for the MACS solution results in an iron concentration of $c_{Fe} = 153 \text{ mM}$ after conversion to the native solution by multiplying with 10,000. This value is 4.25 times higher than the concentration determined theoretically from T_2^* and the magnetization, assuming a particle radius of $R_p = 25 \text{ nm}$.

If the MACS iron concentration determined by MS is used to calculate a corresponding particle diameter, a radius of $R_p = 51 \text{ nm}$ is determined. This value is about twice as high as the published value of hydrodynamic radius [102].

9.1.4 Discussion

An increase in magnetic field strength leads to a significant decrease in T_1 relaxivity and an increase in T_2 and T_2^* relaxivity of iron oxide based contrast agents. Both effects combine to a highly increased r_2/r_1 ratio at 17.6 T compared to field strengths around 1 T. At high field strengths, iron oxide based contrast agents solely produce T_2 and T_2^* contrast.

If the iron concentration of USPIO particles is unknown, the theory of Ziener et al. [104] allows for obtaining accurate values within an order of magnitude depending on the information available on particle size. The only parameters that need to be determined experimentally are the transverse relaxation time T_2^* and the sample magnetization M_s . On the other hand, knowledge of the iron concentration allows calculation of the particle radius and allows validating the theory with respect to the composition of the particle coating. It is still being investigated how the dextran coating can be dealt with mathematically, e.g. by assuming a soft shell with limited penetration depth for the surrounding spins.

Two out of three samples that were studied with MS yielded plausible results (Resovist and Millipore water). Therefore, the value obtained for MACS is assumed to be correct. The reason for the high discrepancy between nominal and experimental values of the VSOP sample is unknown.

Resovist and VSOP solutions are composed of individual particles, while the MACS particles used in this study are connected to IgG antibodies. It is unknown how many MACS are bound to one antibody, but a distribution of a single particle per antibody is very unlikely. If MACS particles were distributed homogeneously over the sample, a similar result as for Resovist particles has to be expected, and a radius would be obtained in the range between the core and the hydrodynamic value. The larger particle radius or alternatively the underestimation of the iron concentration lead to the conclusion that some amount of clustering has occurred. This is substantiated by the lower relaxivity of MACS, which is possibly caused by reduction of the effective surface due to clustering.

9.2 Specific labeling of *X. laevis* embryos

9.2.1 Preliminary experiments

In the second part of the project, the MACS particles coupled to antibodies were used in order to evaluate the feasibility of specific targeting and detection of an iron oxide contrast agent in a model organism. Fluorescence experiments were performed by Dr. Robert Hock at the Department of Cell and Developmental Biology, University of Würzburg to evaluate whether antibodies carrying MACS particles are able to penetrate the tissue of fixed *X. laevis* embryos. Indirect immunolabeling was performed by incubation with the primary antibody that was specific to desmin, a characteristic protein found in mesoderm cells and thus in the somites of the embryo (see chapter 9 for details). A texas-red fluorescent second antibody specific to the primary antibody was used in a second step incubation. After washing and confocal microscopy, an image was obtained that showed the distribution of primary antibodies and thus its specificity. In a second experiment, MACS-coupled antibodies specific to the primary antibody were used for incubation, and

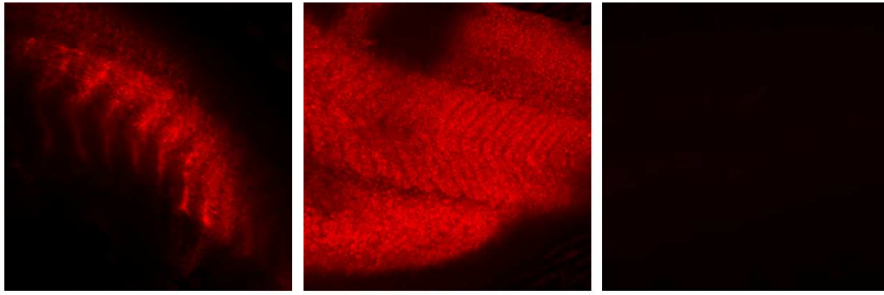


Fig. 9.5: Confocal microscopy images of embryos incubated with primary antibody (ab) and various secondary incubations: (left) texas red-coupled antibody, (center) MACS-coupled antibody and texas red-coupled antibody specific to secondary, (right) same as center without secondary MACS-coupled antibody

a third antibody specific to the second one was used to display the specificity map of the secondary antibody. The third experiment was carried out in a similar fashion, except the second antibody was left out. Any residual fluorescence therefore reveals non-specific binding of the third antibody.

From the images in Fig. 9.5, it can be concluded that the first antibody bound specifically to the desmin found in the somites. Compared to the incubation with the MACS-coupled antibody (center image), it appeared that some specificity was lost and a higher number of secondary antibodies were bounding. The absence of fluorescent signal in the third experiment indicated that the fluorescence observed in the second experiment was indeed caused by the distribution of the secondary antibody and not any unwanted binding of antibody three.

It has thus been shown that MACS-coupled antibodies penetrate fixed embryos. Obviously, some specificity is lost in the process of using MACS-coupled antibodies.

9.2.2 Methods and Materials

In vitro fertilization and culture of *X. laevis* embryos were performed as described previously [93]. Stage 41 embryos were fixed in MEMFA and placed in PBS. Whole mount immunolocalization was carried out using primary antibodies (ab1) directed to desmin. Secondary antibodies (ab2) coupled to MACS particles were used to detect bound desmin antibodies. Embryos incubated with either primary or secondary antibodies only were used as controls.

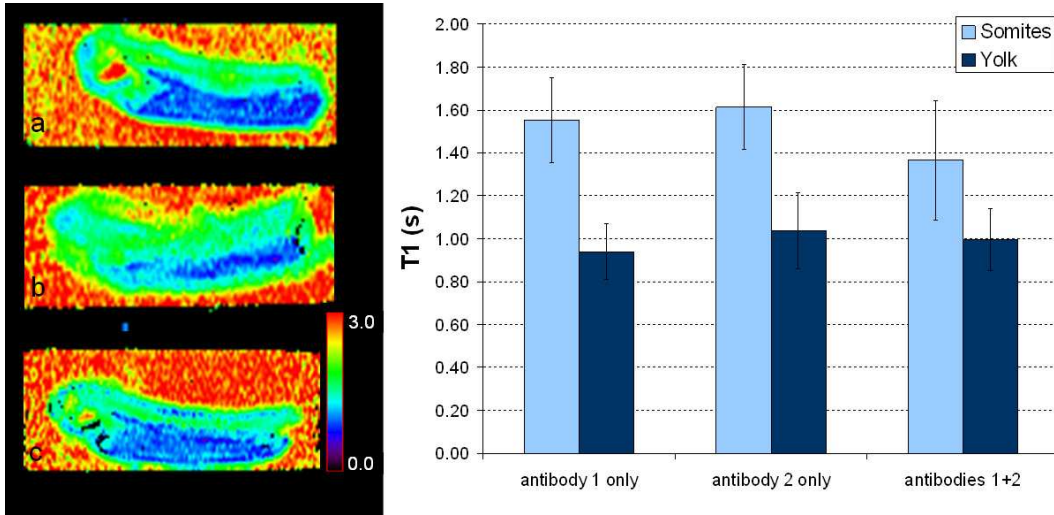
NMR imaging was performed using the homebuilt 2 mm solenoid coil described in section 7.3 that was immersed in susceptibility matching fluid (FC-43). 3D T_1 , T_2 and T_2^* relaxation time maps were acquired using the methods described in Chapter 3.

9.2.3 Results and Discussion

The relaxation time values obtained from ROIs placed in the somites and in the yolk in the respective parameter maps are summed up in Table 9.3. After labelling embryos with iron oxide coupled antibodies, there was almost no change in T_1 , while both T_2 and T_2^* were reduced by 75% in the somite region after incubation with both antibodies.

	T_1 (s) Mean \pm SD (sem)	T_2 (ms) Mean \pm SD (sem)	T_2^* (ms) Mean \pm SD (sem)
<i>Somites</i>			
ab1 only	1.55 \pm 0.20 (0.01)	41.59 \pm 13.75 (0.64)	10.96 \pm 3.62 (0.19)
ab2 only	1.61 \pm 0.20 (0.01)	-	4.64 \pm 2.30 (0.10)
ab1+ab2	1.37 \pm 0.28 (0.02)	11.70 \pm 5.63 (0.62)	2.77 \pm 0.96 (0.07)
<i>Yolk</i>			
ab1 only	0.94 \pm 0.13 (0.01)	8.94 \pm 1.83 (0.10)	1.42 \pm 0.83 (0.04)
ab2 only	1.04 \pm 0.18 (0.01)	-	2.44 \pm 0.78 (0.03)
ab1+ab2	1.00 \pm 0.15 (0.01)	13.01 \pm 9.12 (0.37)	1.72 \pm 0.49 (0.02)

Tab. 9.3: Relaxation times in ROIs of specifically labeled embryos

Fig. 9.6: T_1 relaxation time maps (T_1 in s) of *X. laevis* embryos incubated with primary antibody only (a), secondary antibody only (b) and both antibodies (c); ROI data from somites and yolk shown in chart

After incubation with antibody 2 only, a reduction of 60% in T_2 of the somites was observed. Additionally, it was observed that other regions than the somites also experienced reduction in T_2 and T_2^* .

The volume-averaged concentration of iron oxide can be calculated from the change in relaxation times and the knowledge about the relaxivity of MACS that has been determined previously. This has been performed for both the T_1 and the T_2 data by using the values obtained from the somite ROIs of embryos incubated with antibody 1 only and both antibodies 1 and 2. By applying Eq. 9.1, the iron concentration resulting from T_1 data is $c_{Fe,T_1} \approx (10.6 \pm 1.3)$ mM based on the iron concentration determined by mass spectrometry ($c_{Fe} = 153$ mM), corresponding to a dilution of 1:15 from the primary solution. T_2 data yields an iron concentration of $c_{Fe,T_2} \approx (9.4 \pm 1.7)$ mM and a respective dilution of 1:17. The embryos were incubated in a dilution which is comparable to the values obtained from the T_1 and T_2 data. It can be concluded that on a macroscopic scale, no concentration enhancing effect has occurred, which can be attributed to the volume-

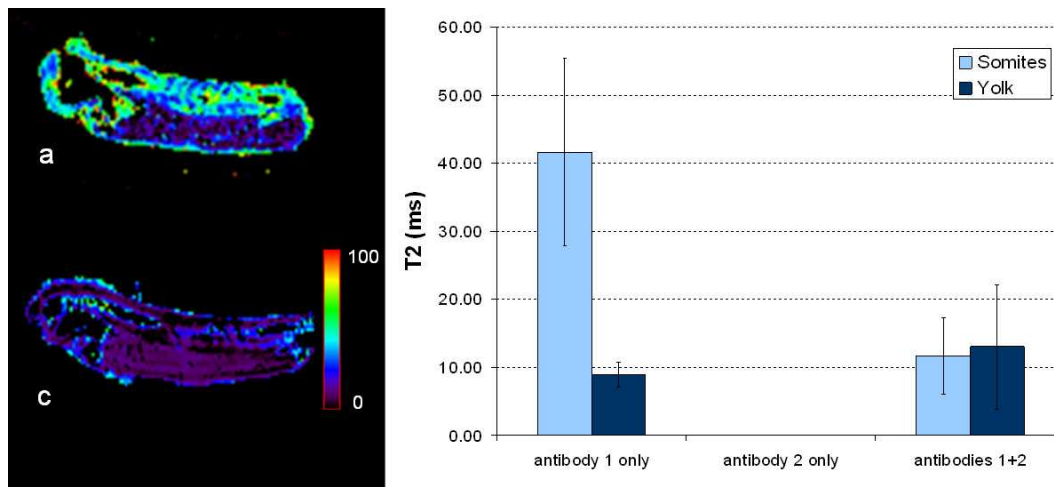


Fig. 9.7: T_2 relaxation time maps (T_2 in ms) of *X. laevis* embryos incubated with primary antibody only (a) and both antibodies (c); ROI data from somites and yolk shown in chart

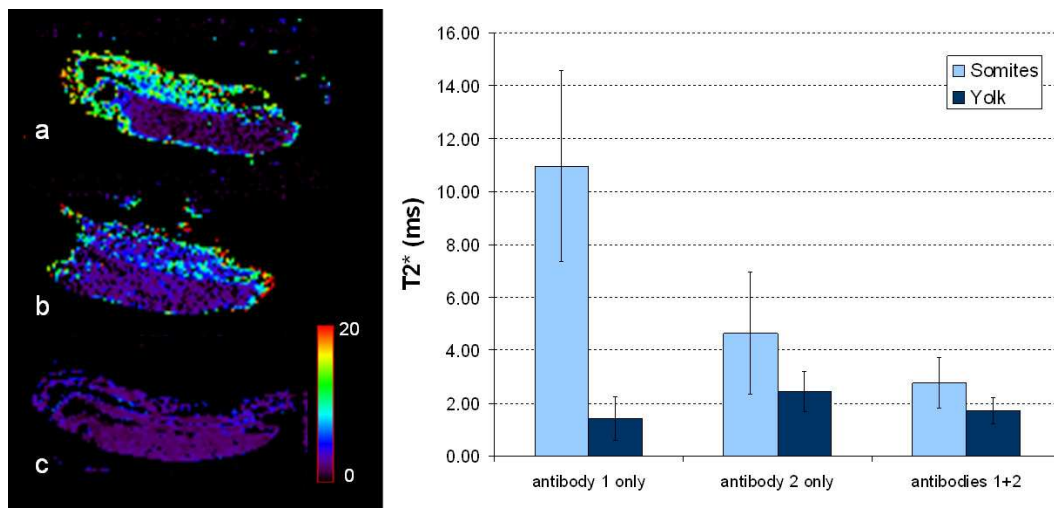


Fig. 9.8: T_2^* relaxation time maps (T_2^* in ms) of *X. laevis* embryos incubated with primary antibody only (a), secondary antibody only (b) and both antibodies (c); ROI data from somites and yolk shown in chart

averaging nature of the method. Despite the small voxel size, one single voxel is still very large on a molecular scale; signal obtained from one voxel is significantly volume-averaged.

While previous studies using MACS describe effects based on changes in relaxation time weighted sequences only [99], this study shows that significant information can be obtained by mapping relaxation times and deducing concentrations from the changes. Statistical analysis shows that all changes are systematic ($p < 0.001$), even changes in the yolk relaxation times. Antibodies are not expected to enter the yolk sack due to tight packing. It can be concluded that variations between individual specimen account for this variation and a higher number of embryos per preparation is necessary to obtain more significant mean values and standard deviations.

A possible cause for unspecific binding is the large diameter of the USPIO particles: entanglement of the particles is likely to occur within fixed tissue. A potential way to test whether MACS particles get entangled in the fixed tissue requires the repetition of the experiment using smaller particles such as VSOP (very small superparamagnetic iron oxide particles) [103]. Unfortunately, VSOPs coupled to antibodies are not available, making it necessary to carry out the time-consuming procedure of linking the VSOPs to the respective antibodies.

10. CONCLUSION AND OUTLOOK

As shown in this work, NMR microscopy has a high and constantly growing potential for many applications. Being an intrinsically insensitive method, the efficiency of microscopic imaging has been improved to enable more data acquisition per unit time. This is a crucial issue if NMR microscopy is used for screening purposes, such as imaging a number of embryos or insects, which is the case in many studies. As the number of available receiver channels on NMR systems is constantly increasing, it is a logical consequence to further increase the number of parallel coils. To further reduce field distortions and improve linewidths and image quality on multiple samples, developing a probehead that contains multiple susceptibility-matched coils is also a reasonable continuation.

The investigation for alternative susceptibility matching substances indicate that not only the susceptibility difference but also other parameters should be verified and adapted for the best matching results. By conducting more detailed experiments, the focus should be put on highly viscous substances.

Results obtained from the single cell fixation and specific labeling experiments on *X. laevis* suggest that NMR microscopy can provide a lot of preliminary work for studies of more complex NMR problems of biological models. While it is highly desirable to develop readily available molecular imaging and potentially molecular therapy methods in the future, the application on humans is generally only the last step in a long process of scientific and engineering work. Initial studies using NMR are usually carried out on rats or mice due to knowledge of the genome and the availability of mutants with certain desired gene defect. Ultimately, translation onto human physiology and pathology is possible from these models, but as a downside, using model organisms of such complexity can obstruct a clear view on fundamental problems. In these cases, NMR microscopy can potentially provide additional information using simpler and smaller model organisms due to higher spatial resolution, less temporal restriction and hence better access to physical parameters.

The experiments described in this and many other works display the high versatility of NMR microscopy. This versatility and multitude of samples, on the other hand, makes it very difficult to compare the performance of different experiments due to the large number of different parameters involved, such as field strength, RF coil size and type and image sequence. The framework under which NMR microscopy experiments are performed is very experimental and only little standardized. Experiments are often compared very focused on certain aspects, e.g. highest in-plane resolutions, highest voxel volume and shortest acquisition times. While these experiments are necessary for continuously extending the limits, there is also a need for classification and standardization of all the work that has been put into the continuous growth of NMR microscopy. That way, a fair comparison between experiments can be obtained, which is mostly an academic aim. It can also lead to better prediction of experimental outcome and better efficiency

by reducing the experiment time consumed by preliminary experiments, a prerequisite for becoming a widespread industrial application. It is highly desirable to extend NMR microscopy into a conventional method away from the highly experimental framework it is enclosed nowadays. Furthermore, the solidification of present standards can stimulate advances on the experimental sector. Future work therefore might include a detailed theoretical description of the NMR microscopy experiment with special focus on the amount of information acquired in a given time and at a given SNR or contrast to noise-ratio (CNR) to provide an unbiased platform for all present and future NMR microscopic experiments.

11. SUMMARY

Nuclear magnetic resonance (NMR) imaging is a well-established imaging technique. If the achieved spatial resolution is below 100 μm , it is usually denoted as magnetic resonance microscopy (MRM). The spatial resolution limit is on the order of a few μm . Due to diffusion and signal limitations, this is a threshold that is unlikely to be overcome within the near future. Nevertheless, MRM applications are numerous and diverse. As a downside, high resolution imaging is usually time-consuming and technological requirements are very sumptuous. Furthermore, miniaturization of the radiofrequency (RF) coil leading to a so-called microcoil is necessary; it also brings along detrimental effects. Therefore, there is a high potential for optimizing present MRM methods.

Hence it is the aim of this work to improve and further develop present methods in MRM with focus on the RF coil and to apply those methods on new biological applications. All experiments were conducted on a Bruker 17.6 T system with a maximum gradient strength of 1 T/m and four RF receiver channels.

By minimizing the RF coil dimensions, the distance between coil windings and sample volume is reduced. As a consequence, differences in magnetic susceptibility of the coil wire and surrounding air lead to pronounced magnetic field distortions ultimately resulting in image artifacts. Susceptibility matching by immersing the coil in FC-43 is the most common approach that fulfills the requirements of most applications. However, hardly any alternatives are known for cases where usage of FC-43 is not feasible due to its specific disadvantages. Alternative substances were investigated and the usability of two potentially useful substances was checked by susceptibility determination and demonstration experiments after shimming under practical conditions. In contrast to FC-43, Bromotrichloromethane (CBrCl_3) has only a single ^{13}C carbon spectral line and significantly reduces background signal otherwise obtained from FC-43 in ^{13}C experiments. Fomblin Y25 is the second substance that was evaluated and offers higher temperature stability than FC-43.

In a typical MRM microcoil experiment, the sample volume is significantly smaller than the maximum volume usable for imaging. This mismatch has been optimized in order to increase the experiment efficiency by increasing the number of probe coils and samples used. A four-channel probehead consisting of four individual solenoid coils suited for cellular imaging of *Xenopus laevis* oocytes was designed, allowing simultaneous acquisition from four samples. All coils were well isolated and allowed image acquisition with the same spatial resolution as in single coil operation. 3D T_1 -mapping of fixed oocytes was carried out to demonstrate practical use.

This method has also been applied in other studies for increased efficiency: using *X. laevis* oocytes as a single cell model, the effect of chemical fixation on intracellular NMR relaxation times T_1 and T_2 and on diffusion was studied for the first time. Significant reduction of relaxation times was found in all cell compartments; after reimmersion in

buffer, values return close to the initial values, but there were small but statistically significant differences due to residual formaldehyde.

Embryos of the same species have been studied morphologically in different developmental stages. Wild type embryos were compared to embryos that had experienced variations in protein levels of chromosomal proteins HMGN and H1A. The experiment efficiency was increased by imaging multiple embryos simultaneously using the four-channel probehead. Significant differences were found between wild type and HMGN-modified embryos, while no difference was observed between wild type and H1-modified embryos. These results were concordant with results obtained from light microscopy and histology.

The technique of molecular imaging was also performed on *X. laevis* embryos. Commercially available antibodies coupled to ultrasmall superparamagnetic iron oxide (USPIO) dextrane coated particles (MACS) served as a specific probe detectable by MRM, the aim being the detection of tissue specific contrast variations. Initially, the relaxivity of MACS was studied and compared to Resovist and VSOP particles. The iron concentration was determined quantitatively by using a general theoretical approach and results were compared to values obtained from mass spectroscopy. After incubation with MACS antibodies, intraembryonal relaxation times were determined in different regions of the embryo. These values allowed determination of local iron oxide particle concentrations, and specific binding could be distinguished from unspecific binding. A possible cause for the observed unspecific background signal is the large diameter of the iron oxide particles: entanglement of the particles is likely to occur within fixed tissue.

Although applications in this work were focused on *X. laevis* oocytes and embryos, three dimensional imaging on a beewolf head was also carried out in order to visualize the postpharyngeal gland. Additionally, an isolated beewolf antenna was imaged with a spatial resolution of $(8 \mu\text{m})^3$ for depiction of the antennal glands by using a microcoil that was specially designed for this sample.

The experiments carried out in this work show that commercially available MRM systems can be significantly optimized by using small sample-adapted RF coils and by parallel operation of multiple coils, by which the sample throughput and thus time-efficiency is increased. With this optimized setup, practical use was demonstrated in a number of new biological applications.

12. ZUSAMMENFASSUNG

Bildgebung mittels magnetischer Kernresonanz (NMR) ist eine etablierte Methode. Liegt die erreichte Ortsauflösung unter $100\ \mu\text{m}$, wird sie allgemein als Magnetresonanz-Mikroskopie (MRM) bezeichnet. Die Untergrenze der Auflösung liegt in der Größenordnung weniger μm . Aufgrund von Diffusion und begrenztem Signal kann diese Grenze derzeit nicht überwunden werden. Die Anwendungen der MRM sind dennoch sehr vielfältig und breit gestreut. Da höchst aufgelöste Bildgebung meist sehr zeitintensiv ist, kostspielige Anforderungen an die zugrunde liegende Technologie setzt und zudem durch die notwendige Verkleinerung der Hochfrequenz (HF)-Spule auf sogenannte microcoils und Erhöhung der Bildauflösung auch nachteilige Effekte zunehmen, besteht viel Optimierungsbedarf bei bestehenden MRM-Methoden.

Das Ziel dieser Arbeit war daher die Verbesserung und Weiterentwicklung bestehender Methoden der MRM mit besonderem Augenmerk auf die HF-Spule und ihre Anwendung auf neue biologische Fragestellungen. Alle Experimente wurden an einem Bruker 17.6 T-System mit einer maximalen Gradientenstärke von $1\ \text{T/m}$ und vier HF-Empfangskanälen durchgeführt.

Durch die Miniaturisierung der HF-Spule reduziert sich die Entfernung zwischen Spulenwindungen und Probenvolumen, Magnetfeld- und somit Bildverzerrungen aufgrund des Unterschieds in magnetischer Suszeptibilität zwischen Luft und Spulendraht sind die Folge. Der übliche Ansatz der Suszeptibilitätsanpassung mit FC-43 ist für die meisten Anwendungen ausreichend, jedoch gibt es kaum bekannte Alternativen für den Fall, dass die Nachteile von FC-43 eine Verwendung verhindern. Es wurde daher nach alternativen Substanzen gesucht und ihre Verwendbarkeit mittels Suszeptibilitätsmessung und experimentellen Shim-Ergebnissen im praktischen Einsatz geprüft: Bromtrichlormethan (CBrCl_3) verfügt im Gegensatz zu FC-43 nur über eine einzelne Linie im ^{13}C -Spektrum. Dadurch kann das Hintergrundsignal bei ^{13}C -Experimenten deutlich reduziert werden. Die zweite Substanz Fomblin Y25 bietet deutlich höhere Temperaturstabilität als FC-43.

Bei üblichen MRM-Experimenten mit 'microcoils' ist das Probenvolumen deutlich kleiner als das maximal für Bildgebung zur Verfügung stehende Volumen. Dieses Ungleichgewicht wurde ausgenutzt, um die Effizienz von Mikroskopie-Experimenten durch parallelen Einsatz mehrerer 'microcoils' zu erhöhen. Ein Probenkopf mit vier entkoppelten Solenoidspulen wurde für zelluläre Bildgebung an *Xenopus laevis* (Krallenfrosch)-Oozyten konstruiert. Ohne Auflösungsverlust konnten damit vier Proben zeitgleich untersucht werden. Mit der Akquisition von 3D T_1 -Karten konnte auch die Verwendbarkeit für quantitative Bildgebung gezeigt werden.

Diese Methode wurde auch in weiteren Studien zur Steigerung der Effizienz eingesetzt: Am Modell einzelner Zellen (*X. laevis*-Oozyten) wurde die Auswirkung chemischer Fixierung auf NMR-Relaxationszeiten (T_1 , T_2) sowie Diffusion erstmals intrazellulär untersucht. Es konnten erhebliche Verkürzungen der Relaxationszeiten in allen Zel-

lkompartimenten festgestellt werden, die nach Spülung mit Pufferlösung bis auf geringe, statistisch signifikante Abweichungen bedingt durch verbleibendes Formaldehyd auf die Ausgangswerte der nichtfixierten Zelle zurückkehrten.

In einem weiteren Projekt wurden Embryonen derselben Spezies in verschiedenen Entwicklungsstadien morphologisch untersucht. Wildtyp-Embryonen wurden mit Embryonen verglichen, deren natürlicher Gehalt an chromosomalen Proteinen HMGN und H1A verändert wurden. In Kombination mit dem Parallelsulen-Probekopf konnte auch hier die Effizienz gesteigert werden, indem mehrere Embryonen gleichzeitig untersucht wurden. Signifikante Unterschiede zwischen Wildtyp und HMGN-veränderten Embryonen konnten festgestellt werden, während sich kein Unterschied zu H1A-veränderten Embryonen zeigte. Lichtmikroskopie und Histologie lieferten damit übereinstimmende Ergebnisse.

Ebenfalls an *X. laevis*-Embryonen wurde die Technik der molekularen Bildgebung eingesetzt. Ziel war es, mit kommerziell erhältlichen Antikörpern, die an superparamagnetische Eisenoxidpartikel mit einer Größe von wenigen nm (USPIO) mit Dextranhülle gekoppelt sind (MACS), gewebespezifische Kontraständerungen zu erhalten. Zunächst wurde die Relaxivität von MACS untersucht und mit Resovist- sowie VSOP-Partikeln verglichen. Anschließend wurde die Eisenkonzentration quantitativ unter Zuhilfenahme eines allgemeinen theoretischen Modells bestimmt und mit Ergebnissen verglichen, die massenspektroskopisch gewonnen wurden. Nach Inkubation mit MACS wurden Relaxationszeiten intraembryonal in verschiedenen Regionen gemessen. Daraus wurden Konzentrationen von Eisenoxid-Partikeln berechnet; zusätzlich konnte zwischen spezifischer und unspezifischer Bindung differenziert werden. Eine mögliche Erklärung für die beobachtete unspezifische Bindung ist die Partikelgröße, die dazu geführt haben könnte, dass die Partikel sich im Gewebe verfangen.

Obwohl der Anwendungsschwerpunkt dieser Arbeit auf der Bildgebung an *X. laevis*-Oozyten und Embryonen lag, wurde auch Bildgebung am Kopf eines Bienenwolfs zur dreidimensionalen Darstellung der Postpharyngealdrüse durchgeführt. Zusätzlich wurde mit einer speziell auf das Untersuchungsobjekt angepassten 'microcoil' eine isolierte Bienenwolfantenne mit einer Auflösung von $(8\mu\text{m})^3$ untersucht; Ziel war die Darstellung der Antennaldrüsen.

Die durchgeführten Projekte zeigen, dass bei kommerziell erhältlichen MRM-Systemen deutliches Optimierungspotential existiert: zum einen durch verkleinerte und probeangepasste HF-Spulen, zum anderen durch die Parallelisierung mehrerer Spulen, wodurch der Probendurchsatz und damit die Zeiteffizienz gesteigert werden kann. Mit diesem optimierten Aufbau konnte anschließend die Nutzbarkeit der MRM bei neuen biologischen Anwendungen gezeigt werden.

APPENDIX

A. MULTICHANNEL OPERATION

In a typical NMR experiment, a single NMR coil is connected to the console. More precisely, it is connected to a box that contains an active or passive switching device that connects the RF coil to either the transmitter (when pulsing) or the receiver (when acquiring).

A.1 *Sequential acquisition*

Running more than a single NMR coil increases the complexity of the setup, as each coil needs to be pulsed and needs a connection to the receiver likewise. There are two general approaches to this problem, depending on the number of available receive channels on the respective NMR system. The first approach makes use of a switching device that multiplexes the n available coils to the single transmit/receive chain. It is the only option on a single channel system. This sequential scheme is most efficient for sequences that employ a small T_e/T_R -ratio, where the long waiting time can be utilized to excite another sample in a different coil. In a sense, this is analogous to a multislice experiment where spatially separated spins are excited consecutively as well.

A.2 *Simultaneous acquisition*

On a system where multiple receiving channels are available, coils can be operated simultaneously if the number of channels is smaller or equal to the number of coils. In general, only a single transmitter is available. However, its output can be expanded into n individual outputs, where all outputs are phase correct, allowing simultaneous excitation of all samples. The only downside is the loss of transmitter power per output. As the whole

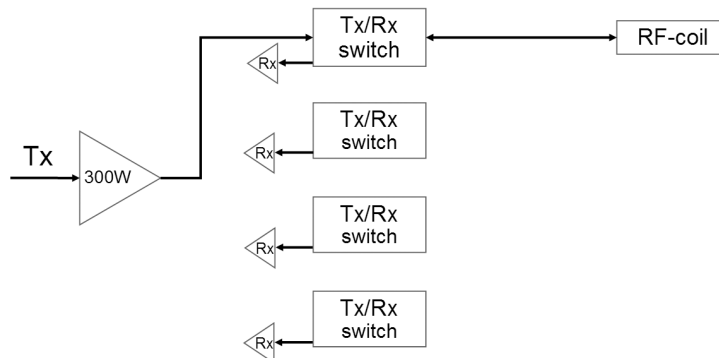


Fig. A.1: Single coil setup

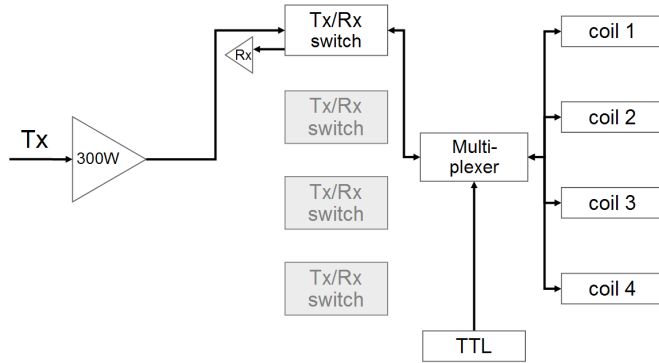


Fig. A.2: Sequential acquisition setup

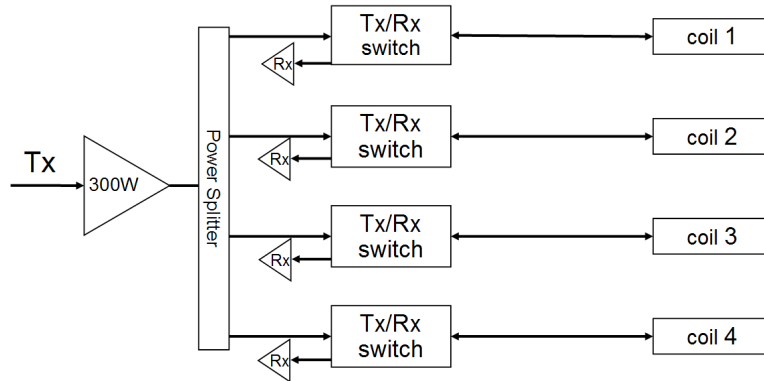


Fig. A.3: Simultaneous acquisition setup

concept behind multiple coils is accompanied by a miniaturization of each coil to make better use of the available homogeneous volume of the NMR magnet, this disadvantage is negligible. Common values for n are 2, 4 and 8. Both methods can be combined in order to perform experiments when the number of coils exceeds the number of channels, as shown in [42].

A.3 Practical details

The NMR system available to multiple coil experiments was a Bruker 750 MHz widebore magnet with an AVANCE console. The system was equipped with one 300 W proton amplifier along with four independent proton receiver channels. Both sequential and simultaneous experiments have been carried out using the methods described in this section.

A.3.1 Sequential acquisition

Prior to the simultaneous experiments described in Section 4, multiplexed experiments have been carried out using a 5-port relay switch (SP5T, MBF Microwave, Henderson, NV) with a maximum switching time of 15 ms, operating frequency range between DC

and 18 GHz, an insertion loss of 0.5 dB and an isolation of 60 dB. It is controlled by TTL outputs from the AVANCE console. The actuating voltage necessary for the switch being +28 V and the actuating current being 160 mA, the TTL signals had to be amplified prior to feeding into the switch. This was accomplished using an integrating circuit containing an array of open-collector Darlington transistors (ULN2003AN). The construction has been described by Zhang et al. [43]. Switching through the console was achieved by adding certain switching commands to the according NMR pulse sequence file. Details can be found in a system manual [105]. It has to be noted that some parameters given in the manual deviate from the actual parameters found on the AVANCE 750 system: the actual NMR word to be set is NMR Control Word 5, the four bits setting the TTL states are 11, 13, 14 and 15. The following command induces a 15 ms delay into the pulse program. During this time, the first TTL line (BNC connector N12) is set to active level (0 V):

```
15m setnmr5^11
```

Resetting is obtained by the command:

```
15m setnmr5|11
```

Setting the state of all four outputs simultaneously is also possible:

```
15m setnmr5|11|13^14|15
```

Hereby, the first, the second and the fourth line are set to a voltage of 0 V while the third line is set to +5 V. Using this syntax, any pulse program can be modified to cycle through all available coils following any desirable pattern. The number of images (NI) has to be adapted accordingly in the base level parameters to obtain the full set of k -space lines.

A.3.2 Simultaneous acquisition

As stated before, simultaneous acquisition requires as many receiver chains as RF coils. The Bruker AVANCE system contains four individual 1H - and X -channels complete with individual preamplifiers, switching boxes and receivers. Transmitting on all coils is achieved by employing a four-point power splitter (ZB4PD1-930W, Mini-Circuits, New York, USA). Receiving on all channels simultaneously cannot be achieved directly by entering additional channel commands into the pulse program under Paravision 3. A workaround is necessary which has been provided by Bruker. It consists of a macro that enables simultaneous acquisition. It is necessary to change a present method into a multichannel-compatible method by supplying a set of scripts needed by the multichannel macro as well as adding a pulse program that contains modified commands.

The new macro can be generated by opening the Multiple Scan Control (MSC) tool from the macros found in Paravision, choosing a certain MSC method and saving it under a new name. The name of the previous method has to be changed to the new method name in the file `init.tcl` to allow the method call. An MSC method requires a modified version of the regular (single channel) pulse program. While the regular pulse program has the ending `.ppg`, the modified pulse program requires the ending `.msc`. Some changes have to be made after copying the `.ppg` into the `.msc` file. In the top section of the `.msc` pulse program, another file has to be included:

```
#include <msc_rcv>
```

Commands setting frequencies on FCU channels have to be modified by adding external code that is controlled by the macro:

```
fq8b:f1    ->  #include <msc_fqb>
fq1:f1     ->  #include <msc_pts>
```

The command REC_ENABLE must be removed:

```
denab REC_ENABLE grad{..}  ->  denab grad{..}
```

Digitizer commands must be substituted by external code:

```
ADC_INIT_B(ph0,ph1)
ADC_START                                ->  #include <msc_adc_init_start_ph0_ph1>

ADC_END                                  ->  #include <msc_adc_end>
```

Hereafter, the new MSC method is functional and can be used from within the MSC macro. Please note that methods starting with `m_` are incompatible with the MSC environment. Extensive details on multiple scan procedures can be found in the respective manual [106].

BIBLIOGRAPHY

- [1] I. I. Rabi. Space quantization in a gyrating magnetic field. *Phys. Rev.*, 51(8):652–654, Apr 1937.
- [2] F. Bloch, W. W. Hansen, and Martin Packard. Nuclear induction. *Phys. Rev.*, 69(3-4):127, Feb 1946.
- [3] F. Bloch. Nuclear induction. *Phys. Rev.*, 70(7-8):460–474, Oct 1946.
- [4] E. M. Purcell, H. C. Torrey, and R. V. Pound. Resonance absorption by nuclear magnetic moments in a solid. *Phys. Rev.*, 69(1-2):37–38, Jan 1946.
- [5] P C Lauterbur. Image Formation by Induced Local Interactions: Examples Employing Nuclear Magnetic Resonance. *Nature*, 242:190–191, 1973.
- [6] P Mansfield and P K Grannell. Nmr 'diffraction' in solids? *Journal of Physics C: Solid State Physics*, 6(22):L422–L426, 1973.
- [7] Paul T Callaghan. *Principles of Nuclear Magnetic Resonance Microscopy*. Oxford University Press, 1991.
- [8] J B Aguayo, S J Blackband, J Schoeniger, M A Mattingly, and M Hinterman. Nuclear magnetic resonance imaging of a single cell. *Nature*, 322:190–191, 1986.
- [9] X Zhou, C S Potter, P C Lauterbur, and B W Both. Nmr imaging with $(6.37\mu\text{m})^3$ isotropic resolution. In *8th Annual Meeting of the Society of Magnetic Resonance in Medicine, Amsterdam, The Netherlands*, page 128, 1989.
- [10] Z H Cho, C B Ahn, S C Juh, H K Lee, R E Jacobs, S Lee, J H Yi, and J M Jo. Nuclear magnetic resonance microscopy with 4-microns resolution: theoretical study and experimental results. *Med Phys*, 15(6):815–824, Nov 1988.
- [11] L Ciobanu, D A Seeber, and C H Pennington. 3D MR microscopy with resolution 3.7 microm by 3.3 microm by 3.3 microm. *J Magn Reson*, 158(1-2):178–182, Sep 2002.
- [12] L Ciobanu and C H Pennington. 3d micron-scale mri of single biological cells. *Solid State Nucl Magn Reson*, 25(1-3):138–141, Jan 2004. Evaluation Studies.
- [13] N Soffe, J Boyd, and M Leonard. The construction of a high-resolution 750 mhz probehead. *Journal of Magnetic Resonance A*, 116:117–121, 1995.
- [14] H C Torrey. Bloch equations with diffusion term. *Phys Rev*, 104:563–565, 1956.

-
- [15] Samuel Gravina and D G Cory. Sensitivity and resolution of constant-time imaging. *Journal of Magnetic Resonance Series B*, 104:53–61, 1994.
- [16] Luisa Ciobanu, Andrew G Webb, and Charles H Pennington. Magnetic resonance imaging of biological cells. *Progress in Magnet Resonance Spectroscopy*, 42:69–93, 2003.
- [17] John L Markley, William J Horsley, and Melvin P Klein. Spin-lattice relaxation measurements in slowly relaxing complex spectra. *Journal of Chemical Physics*, 55(7):3604–3605, 1971.
- [18] E L Hahn. Spin echoes. *Physical Review*, 80:580–594, 1950.
- [19] E W Hsu, J S Schoeniger, R Bowtell, N R Aiken, A Horsman, and S J Blackband. A modified imaging sequence for accurate T2 measurements using NMR microscopy. *J Magn Reson B*, 109(1):66–69, Oct 1995.
- [20] H Y Carr and E M Purcell. Effects of diffusion on free precession in nuclear magnetic resonance experiments. *Physical Review*, 94:630–638, 1954.
- [21] S Meiboom and D Gill. Modified spin-echo method for measuring nuclear relaxation times. *Review of Scientific Instruments*, 29:688–691, 1958.
- [22] E O Stejskal and J E Tanner. Spin diffusion measurements: Spin echoes in the presence of a time-dependent field gradient. *Journal of Chemical Physics*, 42(5):288–292, 1965.
- [23] Andrew G Webb. Radiofrequency microcoils in magnetic resonance. *Progress in Nuclear Magnetic Resonance Spectroscopy*, 31:1–42, 1997.
- [24] E Odeblad. Micro-NMR in high permanent magnetic fields. Theoretical and experimental investigations with an application to the secretions from single glandular units in the human uterine cervix. *Nordisk Forening for Obsterik och Gynekologi, Lund, Sweden*, 45:1–188, 1966.
- [25] J N Shoolery. Small coils for nmr microsamples. *Topics in Carbon-13 NMR Spectroscopy*, 2:28, 1979.
- [26] Ronald C Crouch and Gary E Martin. Micro inverse-detection: A powerful technique for natural product structure elucidation. *Journal of Natural Products*, 55:1343–1347, 1992.
- [27] G E Martin and C E Hadden. Comparison of 1.7 mm submicro and 3 mm micro gradient nmr probes for the acquisition of 1h-13c and 1h-15n heteronuclear shift correlation data. *Magnetic Resonance in Chemistry*, 37(10):721–729, 1999.
- [28] Gotz Schlotterbeck, Alfred Ross, Remo Hochstrasser, Hans Senn, Till Kuhn, Daniel Marek, and Oscar Schett. High-resolution capillary tube NMR. A miniaturized 5-microL high-sensitivity TXI probe for mass-limited samples, off-line LC NMR, and HT NMR. *Anal Chem*, 74(17):4464–4471, Sep 2002.

-
- [29] Dean L Olson, Timothy L Peck, Andrew G Webb, Richard L Magin, and Jonathan V Sweedler. High-resolution microcoil 1h-nmr for mass-limited, nanoliter-volume samples. *Science*, 270:1967–1970, 1995.
- [30] T L Peck, R L Magin, and P C Lauterbur. Design and analysis of microcoils for NMR microscopy. *J Magn Reson B*, 108(2):114–124, Aug 1995.
- [31] A G Webb and S C Grant. Signal-to-noise and magnetic susceptibility trade-offs in solenoidal microcoils for NMR. *J Magn Reson B*, 113(1):83–87, Oct 1996.
- [32] David I Hoult and R E Richards. The signal-to-noise ratio of the nuclear magnetic resonance experiment. *Journal of Magnetic Resonance*, 24:71–85, 1976.
- [33] Dean L Olson, James A Norcross, Mark O’Neil-Johnson, Paul F Molitor, David J Detlefsen, Aaron G Wilson, and Timothy L Peck. Microflow NMR: concepts and capabilities. *Anal Chem*, 76(10):2966–2974, May 2004.
- [34] F D Doty, T J Connick, X Z Ni, and M N Clingan. Noise in high-power, high-frequency double-tuned probes. *Journal of Magnetic Resonance*, 77:536–549, 1988.
- [35] Matthias Brandl. *Quantitative NMR-Mikroskopie an den Grenzen der physikalischen Ortsauflösung*. PhD thesis, Universität Würzburg, 1996.
- [36] P J Hore. Solvent suppression in Fourier transform nuclear magnetic resonance. *Journal of Magnetic Resonance*, 55:283–300, 1983.
- [37] Matthias Brandl and Axel Haase. Molecular diffusion in nmr. *Journal of Magnetic Resonance Series B*, 103:162–176, 1994.
- [38] G Fisher, C Petucci, E MacNamara, and D Raftery. NMR probe for the simultaneous acquisition of multiple samples. *J Magn Reson*, 138(1):160–163, May 1999.
- [39] T Hou, J Smith, E MacNamara, M MacNaughton, and D Raftery. Analysis of multiple samples using multiplex sample NMR: selective excitation and chemical shift imaging approaches. *Anal Chem*, 73(11):2541–2546, Jun 2001.
- [40] Megan A Macnaughtan, Ting Hou, Ernesto MacNamara, Robert E Santini, and Daniel Raftery. NMR difference probe: a dual-coil probe for NMR difference spectroscopy. *J Magn Reson*, 156(1):97–103, May 2002.
- [41] Y Li, A M Wolters, P V Malawey, J V Sweedler, and A G Webb. Multiple solenoidal microcoil probes for high-sensitivity, high-throughput nuclear magnetic resonance spectroscopy. *Anal Chem*, 71(21):4815–4820, Nov 1999.
- [42] H Wang, L Ciobanu, A S Edison, and A G Webb. An eight-coil high-frequency probehead design for high-throughput nuclear magnetic resonance spectroscopy. *J Magn Reson*, 170(2):206–212, Oct 2004.
- [43] X Zhang, J V Sweedler, and A G Webb. A probe design for the acquisition of homonuclear, heteronuclear, and inverse detected NMR spectra from multiple samples. *J Magn Reson*, 153(2):254–258, Dec 2001.

-
- [44] Nicholas A Bock, Norman B Konyer, and R Mark Henkelman. Multiple-mouse MRI. *Magn Reson Med*, 49(1):158–167, Jan 2003.
- [45] Yoshimasa Matsuda, Shin Utsuzawa, Takeaki Kurimoto, Tomoyuki Haishi, Yukako Yamazaki, Katsumi Kose, Izumi Anno, and Mitsuhiro Marutani. Super-parallel MR microscope. *Magn Reson Med*, 50(1):183–189, Jul 2003.
- [46] H Douglas Morris, Alan W Olson, and A Scott Chesnick. A multi-coil multi-sample probe for a 7t (300 mhz) wide-bore nmr imaging spectrometer suitable for developing mouse embryos. In *Proceedings of the 45th ENC, Asilomar*, page 464, 2004.
- [47] Armin Porea, Thomas Neuberger, and Andrew G Webb. Simultaneous nmr microimaging of multiple single-cell samples. *Concepts in Magnetic Resonance Part B (Magnetic Resonance Engineering)*, 22B(1):7–14, 2004.
- [48] J V Sehy, J J Ackerman, and J J Neil. Water and lipid MRI of the *Xenopus* oocyte. *Magn Reson Med*, 46(5):900–906, Nov 2001.
- [49] Jonathan V Sehy, Joseph J H Ackerman, and Jeffrey J Neil. Evidence that both fast and slow water ADC components arise from intracellular space. *Magn Reson Med*, 48(5):765–770, Nov 2002.
- [50] Jonathan V Sehy, Joseph J H Ackerman, and Jeffrey J Neil. Apparent diffusion of water, ions, and small molecules in the *Xenopus* oocyte is consistent with Brownian displacement. *Magn Reson Med*, 48(1):42–51, Jul 2002.
- [51] Jonathan V Sehy, Alison A Banks, Joseph J H Ackerman, and Jeffrey J Neil. Importance of intracellular water apparent diffusion to the measurement of membrane permeability. *Biophys J*, 83(5):2856–2863, Nov 2002.
- [52] M A Griswold, P M Jakob, Nittka M, J W Goldfarb, and A Haase. Partially parallel imaging with localized sensitivities (pils). *Magn Reson Med*, 44:602–609, 2000.
- [53] E. Mark Haacke, Robert W. Brown, Michael R. Thompson, and Venkatesan Ramesh. *Magnetic Resonance Imaging: Physical Principles and Sequence Design*. Wiley, 1999.
- [54] Anthony A Ribeiro and Keiko Umayahara. ^{19}f , ^{13}c nmr analysis of an oxygen carrier, perfluorotributylamine, and perfluoropentanoic acid. *Magnetic Resonance in Chemistry*, 41:107–114, 2003.
- [55] Spectral database for organic compounds. <http://www.aist.go.jp/RIODB/SDBS>. No. 1744.
- [56] K. V. Viswanathan. Multinuclear nonmagnetic resonance studies of perfluoro poly ether lubricants (abstract). *Journal of Applied Physics*, 75(10):6161–6161, 1994.
- [57] H Benveniste, K Kim, L Zhang, and G A Johnson. Magnetic resonance microscopy of the C57BL mouse brain. *Neuroimage*, 11(6 Pt 1):601–611, Jun 2000.

- [58] V V Itskovich, R P Choudhury, J G S Aguinaldo, J T Fallon, S Omerhodzic, E A Fisher, and Z A Fayad. Characterization of aortic root atherosclerosis in ApoE knockout mice: high-resolution in vivo and ex vivo MRM with histological correlation. *Magn Reson Med*, 49(2):381–385, Feb 2003.
- [59] Chris V Bowen, Xiaowei Zhang, George Saab, Paula J Gareau, and Brian K Rutt. Application of the static dephasing regime theory to superparamagnetic iron-oxide loaded cells. *Magn Reson Med*, 48(1):52–61, Jul 2002.
- [60] S C Chu, Y Xu, J A Balschi, and C S Jr Springer. Bulk magnetic susceptibility shifts in NMR studies of compartmentalized samples: use of paramagnetic reagents. *Magn Reson Med*, 13(2):239–262, Feb 1990.
- [61] David R Lide, editor. *CRC handbook of chemistry and physics*, volume 86. Taylor & Francis, 2005.
- [62] D Haddad, F Schaupp, R Brandtm, G Manz, R Menzel, and A Haase. NMR imaging of the honeybee brain. *J Insect Sci*, 4:7, 2004.
- [63] T Hörnschemeyer, J Goebbels, G Weidemann, C Faber, and A Haase. The head-morphology of *ascioplaga mimeta* *neboiss* (coleptera, archostemata) in the context of archostematan phylogeny. *European J Entomol*, 103:409–423, 2006.
- [64] A G Hart, R W Bowtell, W Kockenberger, T Wenseleers, and F L W Ratnieks. Magnetic resonance imaging in entomology: a critical review. *J Insect Sci*, 3:5, 2003.
- [65] G Herzner, W Göttler, J Kroiss, A Porea, A G Webb, P M Jakob, W Rössler, and E Strohm. Males of a solitary wasp possess a postpharyngeal gland. *Arthropod Structure and Development*, 36:123–133, 2007.
- [66] Martin Kaltenpoth, Wolfgang Gottler, Gudrun Herzner, and Erhard Strohm. Symbiotic bacteria protect wasp larvae from fungal infestation. *Curr Biol*, 15(5):475–479, Mar 2005.
- [67] G Allan Johnson, Gary P Cofer, Boma Fubara, Sally L Gewalt, Laurence W Hedlund, and Robert R Maronpot. Magnetic resonance histology for morphologic phenotyping. *J Magn Reson Imaging*, 16(4):423–429, Oct 2002.
- [68] M Dhenain, S W Ruffins, and R E Jacobs. Three-dimensional digital mouse atlas using high-resolution MRI. *Dev Biol*, 232(2):458–470, Apr 2001.
- [69] N Kovacevic, J T Henderson, E Chan, N Lifshitz, J Bishop, A C Evans, R M Henkelman, and X J Chen. A three-dimensional MRI atlas of the mouse brain with estimates of the average and variability. *Cereb Cortex*, 15(5):639–645, May 2005. Evaluation Studies.
- [70] Allan MacKenzie-Graham, Erh-Fang Lee, Ivo D Dinov, Mihail Bota, David W Shattuck, Seth Ruffins, Heng Yuan, Fotios Konstantinidis, Alain Pitiot, Yi Ding, Guogang Hu, Russell E Jacobs, and Arthur W Toga. A multimodal, multidimensional atlas of the C57BL/6J mouse brain. *J Anat*, 204(2):93–102, Feb 2004.

- [71] Robert C Sills, Daniel L Morgan, David W Herr, Peter B Little, Nneka M George, Thai Vu Ton, Nancy E Love, Robert R Maronpot, and G Allan Johnson. Contribution of magnetic resonance microscopy in the 12-week neurotoxicity evaluation of carbonyl sulfide in Fischer 344 rats. *Toxicol Pathol*, 32(5):501–510, Sep 2004.
- [72] Daniel Haddad, Volker Behr, H H Oelschläger, and Axel Haase. 3d-nmr imaging of dolphin embryos and fetuses. In *Proceedings of the 6th ICMRM, Nottingham*, page 11, 2001.
- [73] J A Kiernan. Formaldehyde, formalin, paraformaldehyde and glutaraldehyde: what they are and what they do. *Microscopy Today*, 00(1):8–12, Jul 2000.
- [74] E L Bossart, B A Inglis, X S Silver, and T H Mareci. The effect of fixative solutions on magnetic resonance imaging. In *Proceedings of the 7th ISMRM, Philadelphia*, page 1928, 1999.
- [75] D I Thickman, H L Kundel, and G Wolf. Nuclear magnetic resonance characteristics of fresh and fixed tissue: the effect of elapsed time. *Radiology*, 148(1):183–185, Jul 1983.
- [76] M Tovi and A Ericsson. Measurements of T1 and T2 over time in formalin-fixed human whole-brain specimens. *Acta Radiol*, 33(5):400–404, Sep 1992.
- [77] A M Blamire, J G Rowe, P Styles, and B McDonald. Optimising imaging parameters for post mortem MR imaging of the human brain. *Acta Radiol*, 40(6):593–597, Nov 1999.
- [78] P M Pattany, W R Puckett, K J Klose, R M Quencer, R P Bunge, L Kasuboski, and R G Weaver. High-resolution diffusion-weighted MR of fresh and fixed cat spinal cords: evaluation of diffusion coefficients and anisotropy. *AJNR Am J Neuroradiol*, 18(6):1049–1056, Jun 1997.
- [79] Thelwall PE, Shepherd TM, Stanisz GJ, and Blackband SJ. Effects of temperature and aldehyde fixation on tissue water diffusion properties, studied in an erythrocyte ghost tissue model. *Magn Reson Med*, 56:282–289, 2006.
- [80] V Gulani, A G Webb, I D Duncan, and P C Lauterbur. Apparent diffusion tensor measurements in myelin-deficient rat spinal cords. *Magn Reson Med*, 45(2):191–195, Feb 2001.
- [81] Jonathan V Sehy, Lin Zhao, Junqian Xu, Heidi J Rayala, Joseph J H Ackerman, and Jeffrey J Neil. Effects of physiologic challenge on the ADC of intracellular water in the *Xenopus* oocyte. *Magn Reson Med*, 52(2):239–247, Aug 2004.
- [82] Armin Porea and Andrew G Webb. Reversible and irreversible effects of chemical fixation on the nmr properties of single cells. *Magn Reson Med*, 56:927–931, 2006.
- [83] E W Hsu, N R Aiken, and S J Blackband. A study of diffusion isotropy in single neurons by using NMR microscopy. *Magn Reson Med*, 37(4):624–627, Apr 1997.

-
- [84] Robert Hock. Personal communication, 2006.
- [85] E W Hsu, N R Aiken, and S J Blackband. Nuclear magnetic resonance microscopy of single neurons under hypotonic perturbation. *Am J Physiol*, 271(6 Pt 1):1895–1900, Dec 1996.
- [86] J S Schoeniger, N Aiken, E Hsu, and S J Blackband. Relaxation-time and diffusion NMR microscopy of single neurons. *J Magn Reson B*, 103(3):261–273, Mar 1994.
- [87] R W Bowtell, A Peters, J C Sharp, P Mansfield, E W Hsu, N Aiken, A Horsman, and S J Blackband. NMR microscopy of single neurons using spin echo and line narrowed 2DFT imaging. *Magn Reson Med*, 33(6):790–794, Jun 1995.
- [88] J G M Winkelman and A A C M Beenackers. Correlations for the density and viscosity of aqueous formaldehyde solutions. *Industrial & Engineering Chemistry Research*, 39:557–562, 2000.
- [89] K G Helander. Kinetic studies of formaldehyde binding in tissue. *Biotech Histochem*, 69(3):177–179, May 1994.
- [90] C Papan, S S Velan, S E Fraser, and R E Jacobs. 3d time-lapse analysis of xenopus gastrulation movements using μ mri. *Dev Biol*, 235:289, 2001.
- [91] Ulrich Körner. *Funktionelle Rolle von HMGN Proteinen whrend der Embryonalentwicklung von Xenopus laevis*. PhD thesis, Universität Würzburg, 2004.
- [92] Tina Stange. *Konsequenzen vernderter Histon H1A Proteinmengen für die Embryonalentwicklung von Xenopus laevis*. PhD thesis, Universität Würzburg, 2005.
- [93] R Hock, A Moorman, D Fischer, and U Scheer. Absence of somatic histone H1 in oocytes and preblastula embryos of *Xenopus laevis*. *Dev Biol*, 158(2):510–522, Aug 1993.
- [94] Ulrich Körner, Michael Bustin, Ulrich Scheer, and Robert Hock. Developmental role of hmgN proteins in *xenopus laevis*. *Mech Dev*, 120:1177–1192, 2003.
- [95] Pictoral atlas of *Xenopus laevis* development, <http://www.bio.davidson.edu/people/balom/>.
- [96] R Weissleder and U Mahmood. Molecular imaging. *Radiology*, 219(2):316–333, May 2001.
- [97] J Sharpe, U Ahlgren, P Perry, B Hill, A Ross, J Hecksher-Srensen, R Baldock, and D Davidson. Optical projection tomography as a tool for 3D microscopy and gene expression studies. *Science*, 296:541–545, 2002.
- [98] A Y Louie, M M Huber, E T Ahrens, U Rothbacher, R Moats, R E Jacobs, S E Fraser, and T J Meade. In vivo visualization of gene expression using magnetic resonance imaging. *Nat Biotechnol*, 18(3):321–325, Mar 2000.

- [99] I Pirko, A J Johnson, M Rodriguez, and S I Macura. Immuno-imaging: cell-selective in vivo nmr microscopy in experimental animals. In *Proceedings of the 11th ISMRM, Toronto*, page 832, 2003.
- [100] R Lawaczeck, H Bauer, T Frenzel, M Hasegawa, Y Ito, K Kito, N Miwa, H Tsutsui, H Vogler, and H J Weinmann. Magnetic iron oxide particles coated with carboxy-dextran for parenteral administration and liver contrasting. Pre-clinical profile of SH U555A. *Acta Radiol*, 38(4 Pt 1):584–597, Jul 1997.
- [101] VSOP C200 datasheet, Ferropharm GmbH, Aug 2005.
- [102] S Miltenyi, W Muller, W Weichel, and A Radbruch. High gradient magnetic cell separation with MACS. *Cytometry*, 11(2):231–238, 1990.
- [103] M Taupitz, J Schnorr, C Abramjuk, S Wagner, H Pilgrimm, H Hunigen, and B Hamm. New generation of monomer-stabilized very small superparamagnetic iron oxide particles (VSOP) as contrast medium for MR angiography: preclinical results in rats and rabbits. *J Magn Reson Imaging*, 12(6):905–911, Dec 2000.
- [104] C H Ziener, W R Bauer, and P M Jakob. Transverse relaxation of cells labeled with magnetic nanoparticles. *Magn Reson Med*, 54(3):702–706, Sep 2005.
- [105] Bruker Biospin GmbH. *Paravision Manual*, 2000. Chapter 19: Basic Aquisition.
- [106] Bruker Biospin GmbH. *Paravision Manual*, 2000. Chapter 22: The Multiple Scan Control Tool.

PUBLICATIONS

Journal Papers

A. Porea, T. Neuberger, A.G. Webb

Simultaneous NMR Microimaging of Multiple Single-Cell Samples

Concepts Magn. Reson. Part B: Magn. Reson. Engin. 22B (1): 7-14 (2004)

A. Porea, A.G. Webb

Reversible and Irreversible Effects of Chemical Fixation on the NMR Properties of Single Cells

Magn. Reson. Med. 56: 927-931 (2006)

G. Herzner, W. Göttler, J. Kroiss, **A. Porea**, A. G. Webb, P.M. Jakob, W. Rössler, E. Strohm

Males of a solitary wasp possess a postpharyngeal gland

Arthropod Struct. and Develop. 36(2): 123-133 (2007)

M. D. Grynbaum, D. Kreidler, J. Rehbein, **A. Porea**, P. Schuler, W. Schaal, H. Czesla, A. Webb, V. Schurig, K. Albert

Hyphenation of Gas Chromatography to Microcoil 1H Nuclear Magnetic Resonance Spectroscopy

Anal. Chem. 79(7): 2708-2713 (2007)

Conference Papers

Oral presentations:

A. Porea, T. Neuberger, S. Aussenhofer, U. Körner, A. G. Webb

Parallel NMR Microimaging of Single Cells

44th ENC, Savannah, Georgia, USA, 30 March - 4 April (2003)

A. Porea, C. Faber, R. Hock, T. Neuberger, A. G. Webb, P. M. Jakob

Cellular and molecular magnetic resonance microscopy at 17.6 T

EUROMAR/EENC2005, Veldhoven, The Netherlands, 3 – 8 July (2005)

A. Porea, R. Hock, A. G. Webb, P.M. Jakob
NMR microscopy and relaxation time quantification of *Xenopus laevis* embryos after labeling with antibody-coupled iron oxide particles
8th ICMRM, Utsunomiya, Japan, August 22–26 (2005)

A. Porea
MR Microscopy from Embryos to Single Cells
International Symposium on Biomedical Magnetic Resonance Imaging and Spectroscopy at Very High Fields, Würzburg, Germany, 16 - 18 February (2006)

A. Porea, R. Hock, A. G. Webb, P.M. Jakob
Magnetic resonance microscopy of USPIO-based labeling of *Xenopus laevis* embryos
ESMRMB, Warsaw, Poland, September 21–23 (2006)

Poster presentations:

A. Porea, T. Neuberger, C. Faber, A. Haase, A. G. Webb
NMR-Hochfeldmikroskopie mit optimierten HF-Spulen
DPG-Frühjahrstagung, Dresden, Germany, March 24 - 28 (2003)

D. Haddad, **A. Porea**, M. Schmidt, M. Haas-Rioth, H. H. A. Oelschlger, A. Haase
Embryonal and fetal brain development in bovines, a MR-Histology study
ESMRMB, Rotterdam, The Netherlands, September 18 - 21 (2003)

A. Porea, D. Haddad, T. Neuberger, A. Haase, A. G. Webb
The effects of chemical fixation on intracellular NMR relaxation times
7th ICMRM, Snowbird, Utah, USA, September 21–26 (2003)

A. G. Webb, L. Ciobanu, **A. Porea**, T. Neuberger, C. Pennington
Relative signal-to-noise efficiencies of phase- and frequency-encoding methods in NMR microimaging
7th ICMRM, Snowbird, Utah, USA, September 21–26 (2003)

D. Haddad, **A. Porea**, M. Schmidt, M. Haas-Rioth, H. H. A. Oelschlger, A. Haase
MR-Histology: Embryonal and Fetal Brain Development in Bovines
7th ICMRM, Snowbird, Utah, USA, September 21–26 (2003)

T. Neuberger, H. Schneider, D. Haddad, **A. Porea**, M. Westhoff, A. Haase, U. Zimmermann, C. Faber, A. Webb
NMR microscopy of the lipid distribution in air-dry branches of the resurrection plant *Myrothamnus flabellifolia*
7th ICMRM, Snowbird, Utah, USA, September 21–26 (2003)

A. Porea, V. Gulani, D. Haddad, A. G. Webb
Single Cell NMR Studies of Chemical Fixation
45th ENC, Asilomar, California, USA, April 18 - 23 (2004)

V. Gulani, **A. Porea**, P. Schmitt, M. A. Griswold, A. G. Webb
Detection of small electrical currents using NMR microscopy
12th ISMRM, p. 2314, Kyoto, Japan, May 15 - 21 (2004)

A. Porea, U. Körner, P. M. Jakob, R. Hock, A. G. Webb
Morphological Analyses of wildtype and HMGN-manipulated *Xenopus laevis* Embryos
using High Resolution Magnetic Resonance Imaging at 17.6 Tesla
13th ISMRM, p. 2534, Miami Beach, Florida, USA, May 7 - 13 (2005)

D. Haddad, K. H. Hiller, **A. Porea**, A. Heymer, M. Weber, R. Hock, U. Nöth, P. Jakob
Magnetic Resonance Imaging (MRI) on a cellular level
2nd International Conference Strategies in Tissue Engineering, Würzburg, Germany, May
31 - June 2 (2006)

V. Hörr, **A. Porea**, C. Faber
In vivo intra-oocyte NMR spectroscopy
9th ICMRM, Aachen, Germany, September 3-7 (2007)

Erklärung

gemäß §5, Abs. 2, Ziff. 2 und 5
der Promotionsordnung der Fakultät für Physik und Astronomie der
Julius-Maximilians-Universität Würzburg
vom 22. September 2003

Hiermit erkläre ich an Eides statt, dass ich die Dissertation eigenständig, d.h. insbesondere selbständig und ohne Hilfe eines kommerziellen Promotionsberaters angefertigt und keine anderen als die von mir angegebenen Quellen und Hilfsmittel benutzt habe.

Die Dissertation wurde bisher weder in gleicher noch in anderer Form in einem anderen Prüfungsfach vorgelegt.

Am 15. Dezember 2001 wurde mir von der University of New Mexico (USA) der akademische Grad "Master of Science" verliehen. Weiterhin wurde mir am 30. April 2002 der akademische Grad Diplom-Physiker Univ. von der Universität Würzburg verliehen. Andere akademische Grade habe ich weder erworben noch versucht zu erwerben.

Würzburg, 07.04.2008

Edmund Armin Porea

Lebenslauf

Persönliche Daten

Edmund Armin Porea
Dundeestr. 20
97084 Würzburg

geboren am 23.08.1977 in Lugosch, Rumänien
verheiratet, deutsch

Schulbildung

09.1987–06.1996 Abtei-Gymnasium Duisburg-Hamborn, Abitur

Zivildienst

09.1996–09.1997 St. Johannes-Hospital Duisburg-Hamborn

Studium

10.1997–04.2002 Physik, Universität Würzburg
Abschluss: Diplom-Physiker

08.2000–09.2001 Auslandsaufenthalt an der University of New Mexico, USA; Abschluss:
Master of Science (Physics)
Thema der Master's thesis/Diplomarbeit: *Feasibility of Unilateral Nuclear Magnetic Resonance*

seit 06.2002 Promotionsstudium, Lehrstuhl für Experimentelle Physik V, Universität Würzburg

Berufliche Tätigkeit

07.2002–12.2006 Wissenschaftlicher Mitarbeiter, Lehrstuhl für Experimentelle Physik V, Universität Würzburg

seit 04.2007 Diplom-Physiker, Rapid Biomedical GmbH, Rimpar

Würzburg, 07.04.2008